

Size and Morphology Effects on the Cell Voltage of Li-Batteries: Case Study of RuO₂

Von der Fakultät Chemie der Universität Stuttgart
zur Erlangung der Würde eines
Doktors der Naturwissenschaften (Dr. rer. nat.)
genehmigte Abhandlung

Vorgelegt von
Olga Delmer (geb. Reifschneider)
aus Frunse (Kirgisistan)

Hauptberichter:	Prof. Dr. J. Maier
Mitberichter:	Prof. Dr. H. Bertagnolli
Mitberichter:	Prof. Dr. T. Schleid
Tag der Einreichung:	23.07.2009
Tag der mündlichen Prüfung:	11.11.2009

Max-Planck-Institut für Festkörperforschung
Stuttgart
2009

Contents

Zusammenfassung	5
Abstract	9
List of Abbreviations	12
List of Symbols	13
1 Introduction	15
2 Fundamentals	18
2.1 Li-Batteries _____	18
2.2 Nano-Size-Effects _____	20
Storage Anomaly _____	20
Impact on Energetics _____	21
2.3 RuO ₂ – Model Electrode _____	24
3 Experimental	27
3.1 Materials, Preparation _____	27
3.1.1 RuO ₂ _____	27
3.1.2 Metallic Ru _____	28
3.2 Materials, Characterization _____	29
3.2.1 RuO ₂ _____	29
3.2.1.1 XRD _____	29
3.2.1.2 HRTEM/SEM _____	30
3.2.1.3 Raman _____	33
3.2.1.4 XPS _____	34

3.2.2	Metallic Ru	35
3.2.2.1	XRD	35
3.2.2.2	SEM/HRTEM	36
3.3	Hydrous Nano-Crystalline RuO ₂	38
3.3.1	Synthesis and Characterization	38
3.3.1.1	XRD Analysis	40
3.3.1.2	Raman Analysis	41
3.3.1.3	TG/MS Analysis	42
3.4	Electrochemical Cell	44
3.5	Electrode Preparation	45
3.6	Electrochemical Tests	45
3.6.1	Discharge/Charge, Capacity	45
3.6.2	GITT	47
3.7	Calculation of Diffusion Coefficient and Li ⁺ -Conductivity	48
4	Results and Discussion	52
4.1	Investigations on RuO ₂	52
4.1.1	Performance of the Electrodes	52
4.1.1.1	Discharge Curves	55
4.1.1.2	Capacity and Influence of PVDF	57
4.1.2	Enhanced Potential of Amorphous RuO ₂	59
4.1.2.1	Thermodynamic Analysis (Chemical Potentials of Li)	63
4.1.2.1.1	Approach 1: Application of cell reaction formalism	64
4.1.2.1.2	Approach 2: Application of mixture thermodynamics	66
4.1.3	Li-Diffusion Coefficient and Li ⁺ -Conductivity	74
4.1.3.1	Amorphous Powders	74
4.1.3.2	Crystalline Powders	76
4.1.3.3	Comparison of the Ionic Conductivities	78
4.1.3.4	Comparison of Diffusion Coefficients	79
4.1.4	Hydrous Nano-Crystalline RuO ₂	74
4.1.4.1	Electrochemical Measurements	80
4.1.4.1.1	Discharge and Charge	80
4.1.4.1.2	GITT, OCV and Li-Diffusion	81
4.1.5	Influence of PVDF on OCV Values	83
4.2	Storage of Li in Metallic Ru	88
5	Conclusions and Outlook	91
	Appendixes	94
	List of Figures	95
	References	99
	Acknowledgements	105
	Curriculum Vitae	107

Zusammenfassung

In der vorliegenden Arbeit wurde RuO_2 als positive Modellelektrode für Li-Batterien im Hinblick auf die Abhängigkeit der Zellspannung der Zelle RuO_2/Li^+ -Elektrolyt/Li von der Teilchengröße und der Morphologie untersucht. Das Ziel dieser Untersuchungen ist, zum Verständnis dieses spezifischen Feldes der Größeneffekte beizutragen und einen Schritt in die Richtung der Verbesserung der positiven Elektroden der Li-Sekundärbatterietechnologie zu ermöglichen.

RuO_2 ist als Modellelektrode besonders geeignet. Das Material zeigt alle relevanten Mechanismen der Li-Speicherung, die in den Li-Batterien bekannt sind. Zusätzlich weist es ausgezeichnete elektronische Leitfähigkeit, eine gute Li-Diffusion und eine einzigartige Kombination aus hoher Kapazität und hoher Coulomb-Effizienz in den ersten Entlade-/Ladezyklen auf.

Nicht alle in RuO_2 möglichen Speichermechanismen wurden im Detail untersucht. Die Untersuchungen wurden auf die Speicherung von Li im Ein- und Zweiphasengebiet, d.h. die Bildung von Li-gesättigtem RuO_2 und die Umwandlung in LiRuO_2 durch einen weiteren Li-Zusatz, konzentriert. Als weiterer Punkt wurde die Speicherung von Li in den Grenzflächen des nanoskopischen $\text{Ru}/\text{Li}_2\text{O}$ Gemisches, welches nach der vollständigen Reduktion von RuO_2 zu Ru gebildet wird, untersucht.

Die im Rahmen dieser Arbeit betrachteten Materialien sind kristalline Pulver mit durchschnittlichen Kristallgrößen von 10 μm , 60 nm, 30 nm und 1.5-3 nm, und amorphe Pulver, die aus den kristallinen (60 nm und 30 nm) Proben elektrochemisch hergestellt werden konnten. Für die elektrochemischen

Untersuchungen wurden zum einen reine Pulver direkt als Elektrode eingesetzt. Zum anderen wurden in einer parallelen Studie Elektroden unter Verwendung eines üblichen Binders (hier polyvinylene difluoride (PVDF)) präpariert.

Elektrochemische Experimente d.h. Messungen der Leerlaufspannung (OCV), galvanostatische intermittierende Titration (GITT) sowie Entladungs- und Ladungsexperimente wurden systematisch an den Li/RuO₂-Systemen durchgeführt und lieferten dabei Informationen über die Zellspannung gegen Li, den Li-Diffusionskoeffizienten, die Li⁺-Leitfähigkeit, das Entladungsverhalten und die Kapazität. Li-Speicherungsexperimente an reinem Ru wurden zum besseren Verständnis der Grenzflächenspeicherung an drei Ru-Pulvern mit verschiedenen Teilchengrößeverteilungen durchgeführt.

Die wichtigsten Ergebnisse, die durch die beschriebenen Untersuchungen erzielt wurden, sind folgende:

- eine Erhöhung der Zellspannung um *ca.* 0.5 V im Falle der amorphen Phase im Vergleich zur kristallinen. Diese Potentialerhöhung konnte als freie Schmelzenergie halb-quantitativ verstanden werden. Zusätzlich zeigte eine ausführliche quantitative Analyse der chemischen Potenziale erhebliche Unterschiede im Ein- und Zweiphasenregime auf. Ein auf der Mischphasenthermodynamik basierendes Modell konnte entwickelt werden, welches die experimentell erhaltenen Li-Löslichkeiten und Leerlaufspannungen miteinander in Bezug bringt. Außerdem konnte dieses Modell auch auf nano-RuO₂ (1.5-3 nm) angewendet werden.
- eine Erhöhung der Zellspannung bis zu 440 mV konnte im Falle der Nanopartikel (1.5-3 nm) erreicht werden. Die erhöhte Spannung konnte durch den Oberflächenbeitrag erklärt werden und lieferte dabei eine scheinbare Grenzflächenspannung von *ca.* 1 Jm⁻².
- die Beschichtung der Partikel mit Binder (PVDF) führte ebenfalls zu erhöhten Zellspannungen (bis zu 340 mV), die nicht völlig verstanden sind.

Ausserdem wurden folgende Ergebnisse erzielt:

- eine neue Methode, die eine Abschätzung der Li-Löslichkeit in den amorphen sowie nano-Materialien ermöglicht und auf der Auswertung der Li^+ -Leitfähigkeit basiert, konnte gefunden werden.
- eine Zunahme der anscheinend reversiblen Kapazität auf bis zu 1.5Li pro Ru durch die Zugabe von Binder konnte erzielt werden. Dieser Effekt konnte der möglichen Li-Speicherung in der Partikel-Binder-Grenzfläche zugeschrieben werden.
- die Versuche, Li in reinem Ru mit verschiedenen Teilchengrößen zu speichern, waren erfolgreich und zeigten eine deutliche Korrelation zwischen der Oberflächengröße und der Menge an gespeichertem Li. Der Großteil der Li-Speicherung konnte durch die Speicherung an der Elektrode-Elektrolyt-Grenzfläche (SEI) erklärt werden, wobei keine Hinweise auf die Speicherung im Ru-Volumen gefunden werden konnten.

Abstract

In the present work RuO_2 as a positive model electrode in a cell RuO_2/Li^+ -electrolyte/Li was investigated with the focus on the influence of the particle size and morphology on the cell voltage of the system. The motivation of these investigations is to contribute to the understanding of that barely studied specific field of size effects and to make a step towards the improvement of the positive electrodes in the rechargeable Li-battery technology.

As a model electrode, RuO_2 is a particularly suitable material. It shows all the relevant modes of Li storage which are known in the Li batteries. Additionally, it exhibits excellent electronic conductivity, a good Li diffusion and offers a unique combination of high capacity and high Coulombic efficiency in the first couple of discharge/charge cycles.

Not all possible reactions were investigated here in detail. The examinations were focused on the storage of Li in the single phase regime followed by a two phase reaction, namely transformation of Li saturated RuO_2 into LiRuO_2 by further Li addition. Furthermore, interfacial storage, which occurs after the full reduction of RuO_2 to Ru, was one of the points of interest.

The considered materials are crystalline powders with the average particle sizes of 10 μm , 60 nm, 30 nm and 1.5 - 3 nm and amorphous powders which could be obtained from the crystalline powders (60 nm and 30 nm) electrochemically. For the electrochemical investigations, pure powders were used directly as electrodes and in a parallel study the electrodes were prepared in a common way, namely using a binder (here polyvinylene difluoride (PVDF)).

Electrochemical experiments, *i.e.*, measurements of the open-circuit voltage (OCV), galvanostatic intermittent titration technique (GITT) and discharge and charge measurements, were systematically performed on Li/RuO₂ systems delivering information about electrochemical potential against Li, Li diffusion coefficient, Li⁺ conductivity, discharge behavior and capacity.

Li storage experiments on pure Ru, for better understanding of the interfacial storage, were performed on three Ru powders with different particle size distributions.

The most important results obtained by the described investigations are following:

- an excess in the electrochemical potential of *ca.* 0.5 V in the case of the amorphous phase in comparison to the crystalline could be obtained and qualitatively understood in terms of melting free energy. Additionally, a detailed quantitative analysis of the chemical potentials delivered striking differences in the single and two phase regime. A model, based on the mixture thermodynamics, was developed and correlated with the experimentally obtained Li solubility limits and OCVs. Furthermore, this model could be also applied to the nano-scaled RuO₂ (1.5 - 3 nm).
- an excess in the electrochemical potential up to 440 mV could be obtained for nano-particles (1.5 - 3 nm) of RuO₂. The excess voltage could be explained by the surface contribution term which delivered the capillary term being 1 Jm⁻².
- the coating of the particles with binder led to the raised electrochemical potential up to 340 mV.

Furthermore,

- a sensitive method, based on the evaluation of the Li⁺-conductivity, for estimation of the Li solubility limits in amorphous and nano-scaled materials could be established.

-
- an increase in apparently reversible capacity up to 1.5Li by addition of binder could be achieved. This effect might be attributed to the storage in the particle-binder-interface.

 - the attempts to store Li in pure Ru with different particle sizes were successful and showed a clear correlation between the surface area and the amount of stored Li. The most storage could be attributed to the storage in the solid electrolyte interface (SEI), whereas no evidences for storage in the bulk could be found.

List of Abbreviations

emf	electromotive force
BET	Brunauer-Emmett-Teller
SEI	Solid Electrolyte Interface
XRD	X-Ray Diffraction
HRTEM	High-Resolution Transmission Electron Microscopy
SAED	Selected Area Electron Diffraction
IR	Infra Rot
XPS	X-Ray photoelectron spectroscopy
SEM	Scanning Electron Microscopy
EC	Ethylene Carbonate
DMC	Dimethyl Carbonate
PVDF	Polyvinylene Difluoride
CB	Carbon Black
GP	Graphite
C	Carbon
NMP	N-Methyl-2-Pyrrolidone
GITT	Galvanostatic Intermittent Titration Technique
OCV	Open-circuit Voltage
TG	Thermo Gravimetry
MS	Mass Spectroscopy

List of Symbols

μ	chemical potential
V	molar volume
$\bar{\gamma}$	average surface tension
\bar{r}	average particle radius
f	surface stress
e	elastic strain
$\bar{\alpha}$	average capillary parameter
E	voltage
G	Gibbs free energy
F	Faraday constant
z, n	number of transferred electrons
Q_{th}	theoretical capacity
Q	real capacity
M	molar weight
I	current
t	time
m	weight of the active mass
η	polarization term
D	chemical diffusion coefficient
S	surface area
c	concentration
σ^{ion}	ionic conductivity
σ^{eon}	electronic conductivity
σ	electrical conductivity
x, a, b	mol fractions of Li
ε, η, ξ	mol fractions of Li
$\alpha, Li_{\varepsilon}Y$	Li-poor phase
$\beta, Li_{\eta}Y$	Li-rich phase
L, l	diffusion length

Chapter 1

Introduction

Technological progress, rising world population and increasing wealth during the last centuries and particularly in the last decades immensely increased the energy consumption worldwide. According to the forecast of energy experts, the energy demand is going to increase dramatically in the next years, especially in the developing countries^{1,2}. From the beginning of industrialization fossil fuel was mainly used to cover the energy requirement. It is obvious that the fossil fuel sources are limited and the use of them caused already evident global climate changes which could irreversibly destroy our biosphere. Due to these facts, during the last years development of new technologies for more efficient energy use and for exploitation of renewable and alternative energy sources became a very big issue.

As one of the energy conversion and storage systems — batteries — play a key role in our mobile world. Without batteries, development of all the variety of portable devices which we use in our daily life would be impossible. Additionally, batteries offer a very promising solution for the environment being able to improve one of the very polluting and energy wasting devices — the automobiles. The car industry already supplies more efficient hybrid technology which seems to be a transition step to the electric cars, being fully powered by batteries which are already planned for the near future. In fact,

batteries can be used to store energy from renewable sources such as solar and wind energy.

Thanks to the high energy density (see Fig. 1), low weight, design flexibility and longer lifespan, Li-based batteries conquered the market, entering also the hybrid technology section. As a result of the memory-effect and low energy density, Ni-Cd batteries are already supplanted by more recent Ni-MH and Li-based batteries even from the power tool market. Ni-MH-batteries today are only used in inexpensive electronics and still generally to power the hybrid vehicles³.

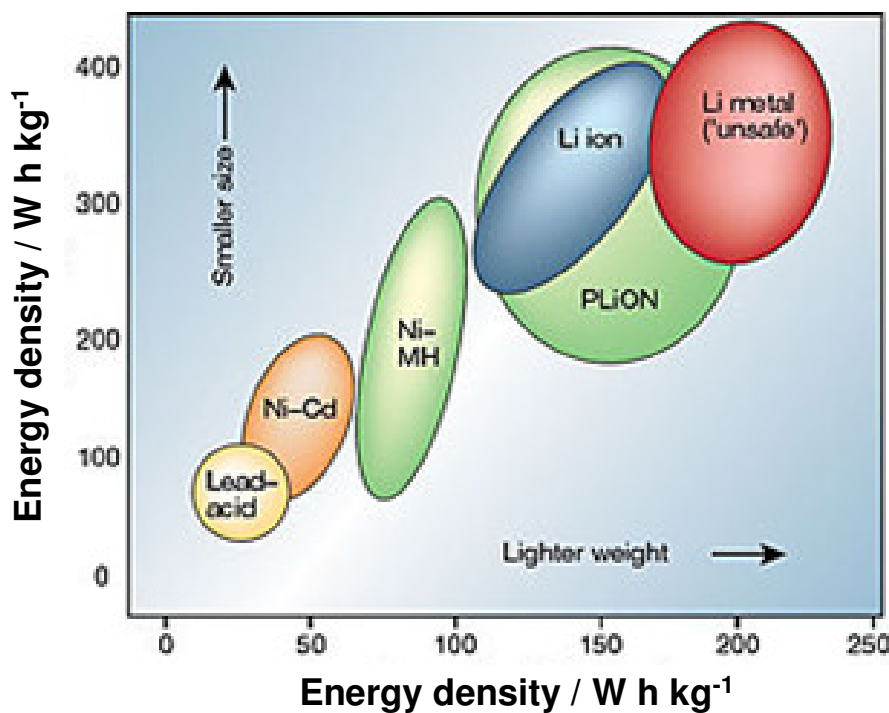


Figure 1: Comparison of gravimetric and volumetric energy densities of different battery technologies. Pb-acid batteries are mainly used in SLI (starting lighting ignition) in automobiles or standby applications⁴.

The pace of progress in the battery technology is much slower than in other areas of electronics. The main reason for this is the lack of suitable electrode materials and electrolytes and the difficulties to deal with the interface between them.

Nanotechnology opened new possibilities to improve Li-based batteries in terms of capacity, power, cost and materials sustainability³. The cycle-life,

though, is risked to suffer under the secondary reactions leading to decomposition of the electrolyte due to the much bigger interfaces according to the increased surface area of the electrodes. Encouragingly, it was already proven that coating of the electrode can protect the electrolyte from undesired red-ox reactions⁵. The benefits of nano-technology in this field are still far from being fully exploited.

In the present work RuO_2 was investigated as a model for positive electrodes in a cell RuO_2/Li^+ -electrolyte/Li in terms of influence of the particle size on the cell voltage. The influence of the particle size on the voltage of a Li-battery is barely studied in comparison to the other nano-size effects on the electrode materials. Only currently, contemporaneously to the present work, a relatively small effect on the voltage could be shown on nano-scaled (~ 40 nm) LiFePO_4 electrode⁶⁻⁸. In this project, open-circuit voltage (OCV), Li-diffusion coefficient, ionic conductivity and discharge/charge – behavior were systematically examined as functions of particle size (10 μm , 60 nm, 30 nm, 1-3 nm) and morphology (crystalline, amorphous). It turns out that also exciting fundamental questions arise that are discussed in dissertation.

Chapter 2

Fundamentals

2.1 Li-Batteries

Lithium is the most electropositive and lightest metal and therewith perfectly qualified for storage systems with high energy densities. Considering that Pb-acid and Ni-Cd battery systems are roughly 100 years old, Li-technology is still pretty young. The development of Li-based batteries begun about 40 years ago with the first primary Li-cells⁹ exhibiting metallic Li as negative electrodes. At about the same time intercalation compounds⁹⁻¹⁴ (mostly sulfides) were discovered which could store lithium in a reversible way. Very fast it could be recognized that using metallic Li as negative electrode led to the dendrite problem, where Li-dendrites grow towards the cathode, in the worst case perforating the separator and causing an internal short-circuit with explosive result. In the best case, the dendrites increase the surface area of Li-electrode which leads to increased reactivity of Li and hence side reactions with the electrolyte at the increased interface result in a decreased cycle-life of the battery. With the introduction of the “rocking-chair” system by Murphy *at al.*¹⁵ and Scrosati *at al.*^{16,17} (see Fig. 2) the dendrite and the safety problems were solved if Li is incorporated in appropriate host materials.

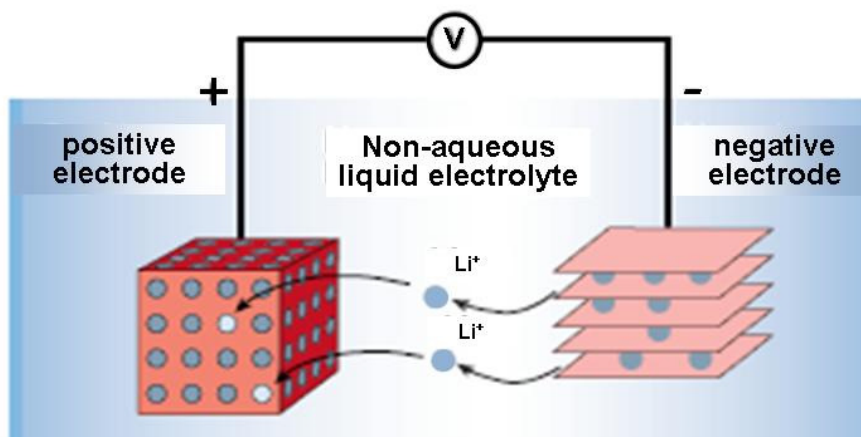


Figure 2: Rechargeable Li-ion battery⁴ (“rocking-chair” - principle)

The “rocking-chair” principle had been previously used in Ni-MH-batteries. It was not easy to fulfill a “simple” concept which requires two inexpensive intercalation compounds with high potential difference and stability to provide sufficiently large cell voltage and a long lasting reversibility of the intercalation reactions. Finally, with the discovery of carbon as a negative intercalation electrode¹⁸, C/LiCoO₂ cell was commercialized by Sony Corporation in 1991. This technology, providing high potential (3.6 V) and high energy density (120-150 W h kg⁻¹), is used nowadays in almost all portable electronic devices. Few improvements of electrolytes followed, *e.g.* introduction of polymeric electrolyte in a liquid Li-ion system¹⁹ (PLiON), making the battery more flexible in design and lighter.

Although the C/LiCoO₂ cell was a great success, the battery systems need to be advanced to fulfill the requirements of the progressing technology such as electric cars. The search for better and cheaper electrode materials and better performing electrode-electrolyte-electrode combinations did not stop. Even though numerous classes of cathode materials were synthesized and anode materials were tried, no real gain in capacity or improvement in performance of Li-system was achieved, until currently very promising nanotechnology entered the field of energy storage. Quite a push to Li-technology is expected by exploring nano-technology, although here a number of fundamental problems can occur.

2.2 Nano-Size-Effects

Down-sizing crystals enhances surface/interface-to-volume ratio and reduces diffusion length for the mass and charge transport. This leads to exciting effects which can be exploited for the design of new materials with excellent properties applicable to energy conversion and storage²⁰⁻²⁷. The beneficial impact of the interfacial contribution and increased defect concentration in nano-crystalline materials on the ionic²⁸⁻³¹ and mixed conduction³²⁻³⁵ are already well studied. Additionally, very slow diffusion coefficients in the solids at room temperature can be compensated by the short diffusion length, *e.g.* reduction of diffusion length from 1 mm to 10 nm at 300 K results for typical diffusion coefficients and activation energies in the same reduction as a temperature enhancement by 300 K³⁵.

For bulk storage, the storage time is proportional to L^2 (L : diffusion length) and together with the high electrode/electrolyte contact area, the charge/discharge rates of nano crystalline electrodes can be much higher (neglecting here the possible improvement of ionic and electronic conductivity *via* size effects). Moreover, the strain of Li insertion/removal can be better accommodated which improves the cycle life. Also new reaction paths come into consideration which are not possible with the bulk²⁰. This opens new possibilities for inexpensive electrode materials with poor ionic and electronic conductivities like *e.g.* LiFePO_4 ³⁶⁻⁴⁰ or TiO_2 (anatase) as a positive electrode. Here, by reduction of particle size or introduction of mesoporosity (reduction of L to few nm) and coating of the particles/pores with an electronic conductor (C, RuO_2) the electronic and ionic conductivity of the composite could be improved significantly, resulting in high storage capacity even at high discharge/charge rates^{41,42}. In spite of the increased surface energies, nano-scaled structures can be very durable which is essential for rechargeable batteries. This is due to the fact that grain growth requires motion also of the sluggish components.

Storage Anomaly

After decomposition reaction of transition metal oxides *e.g.* MO (M: Co, Cu, Ni, Fe, Mo, *etc.*, which do not alloy with Li) with Li upon full reduction to metal, a nano-composite of M and Li_2O is usually formed which is able to take up some extra Li amount, exhibiting a pseudo-capacitive behavior at low

potential⁴³. One reasonable explanation is the interfacial “job-sharing” storage mechanism⁴⁴⁻⁴⁷, in which neither M nor Li₂O can store a significant quantity of Li, but electronegative M can take up electrons and Li₂O is able to accommodate Li⁺ (see Fig. 3).

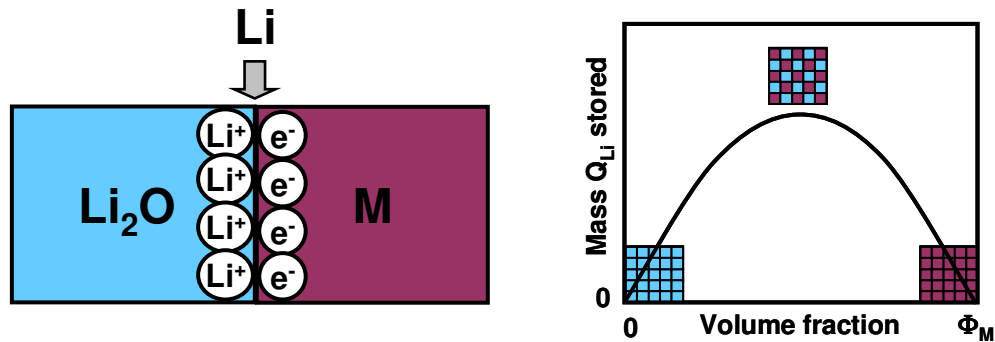


Figure 3: Phenomenological model for the explanation of extra mass storage *via* the interfacial “job-sharing” storage mechanism⁴⁵.

This synergistic effect, where one monolayer of Li per boundary could be possible to store, together with an enormous fraction of interfaces in a nano-composite, can explain the observed capacitor-like behavior (high charge/discharge rate and high reversible capacity) in the investigated M/Li₂O^{45,48} and M/LiF⁴⁹ nano-composites at low potential.

Impact on Energetics

A very popular example of the influence of the particle size on the thermodynamic stability is the suppression of the melting point of Au-nano-particles by several hundreds of degrees⁵⁰. Using a simplified model derived from the fluid systems, which assumes equilibrium shape for the crystals and neglects the surface stress, the variation of the chemical potential μ of a component i can be written as follows:

$$\mu_{i(nano)}^0 = \mu_{i(bulk)}^0 + 2 \frac{\bar{\gamma}}{\bar{r}} V_i, \quad (1)$$

where V_i represents the partial molar volume, $\bar{\gamma}$ and \bar{r} correspond to the average surface tension and average particle radius^{29,30,44}. Since the realistic solid systems are much more complicated and the anisotropic surface stress f

has to be considered which is related to the surface tension γ and is given in his scalar form as

$$f = \gamma + \frac{d\gamma}{de}, \quad (2)$$

with e defined as elastic strain⁵¹, the surface contribution term could be replaced by $2V_i \bar{\alpha}/\bar{r}$, with $\bar{\alpha}$ symbolizing an average capillary parameter being dominated by γ or f , depending on the nature of the solid⁵². Good methods to measure the surface contribution are for example calorimetry experiments⁵³⁻⁵⁵ or emf (electromotive force) measurements⁵⁶⁻⁶³. In the case of emf measurements the surface contribution is directly accessible from *e.g.* the quasi symmetric cell $M_{\text{nano}}/M^+\text{-electrolyte}/M_{\text{bulk}}$ (M: Cu, Ag). The resulting non-zero voltage E of this cell is related through the Nernst equation to the difference of the Gibbs free energies of formation δG_M^0 ($\mu_M^0 \equiv G_M^0/n_M$; with n_M = mole number) between nano- and macro-particle by

$$2 \frac{\bar{\alpha}}{\bar{r}} V = -zFE, \quad (3)$$

with F the Faraday constant and z the number of transferred electrons. (Taking \bar{r} for $\bar{\alpha}$ and some typical values for \bar{r} and V we expect *ca.* 100 mV of difference in voltage from the bulk for particles with 1 nm average radius⁴⁴.) In other words, the cell voltage measurements deliver the difference of chemical potentials of the exchangeable ions. In the case of Cu and Ag, the exchangeable ions are Cu^+ and Ag^+ and in more complicated cases, *i.e.* in the case of anatase (nano- $\text{Na}_2\text{Ti}_6\text{O}_{13}/\text{Na-}\beta''$ alumina/bulk- $\text{Na}_2\text{Ti}_6\text{O}_{13}$)⁶² or RuO_2 ($\text{Li}_x\text{RuO}_2(\text{crystalline})/\text{LiPF}_6+\text{EC}+\text{DMC}/\text{Li}_x\text{RuO}_2(\text{amorphous})$ with $0 < x < 0.04$)^{63,64}, the chemical potentials of Na or Li in the corresponding compounds can be measured through a Na^+ or Li^+ conducting electrolyte. (Ti/O and Ru/O ratios are assumed not to change due to the poor kinetics.)

The surface contribution has an obvious impact on the cell voltage of a Li-battery which might even be exploited in the future. Here, however, we have to make a clear distinction as to whether we want to operate the battery in the single phase regime (solid solution of Li in a compound) or in the two/multi phase regime (*e.g.* reaction $x\text{Li} + \text{Y} \rightleftharpoons \text{Li}_x\text{Y}$, Y: CoO_2 , RuO_2 , FePO_4 , *etc.*)

Let us assume, for the sake of simplicity, a Gibbs energy difference between the metastable state and stable state that is independent of stoichiometry. Then, in the single phase regime, an introduction of metastability (nano-sizing/amorphisation) into the Li-intercalation compound leads, for a given composition, to an increased chemical potential of Li in the metastable compound which means the cell voltage against Li, being the negative electrode and exhibiting the highest Gibbs energy, is decreased. This is explained later in detail (see chapter 4.1.2.1.2). Since the voltage of a cell is given by the difference of the chemical potentials of Li in the cathode and the anode (neglecting the polarization effects), an introduction of metastability would be beneficial for the negative electrode to suppress the intercalation voltage.

The influence of the metastability on the voltage in the two phase regime is much more complicated. It depends a lot on the difference of the surface energies between the metastable educts and the metastable products. Moreover, same nominal compositions correspond to different coexistence compositions. As a consequence, the cell voltage can even be increased which is beneficial for the positive electrode. This surprising feature is part of this thesis and is discussed in chapter 4.1.2. Both effects may even be used in practical systems.

Another consequence of nano-scaled electrodes is the sloped voltage profile of the discharge curve in a two phase regime, in contrast to the plateau at a constant voltage obtained by using bulk electrodes. One reason is that there is a whole spectrum of different transformation voltages due to the size distribution of nano-particles, provided, the Gibbs energies of the pure and the lithiated phases are sufficiently different^{8,44,65}. Further reasons can be size variations of a single particle or even configurational effects due to the tiny size²².

2.3 RuO₂ – Model Electrode

RuO₂ was taken into consideration as an Li intercalation electrode for the first time by Murphy *et al.*¹⁵ about 30 years ago. Few more investigations on this costly material followed, which were restricted to a narrow voltage range, showing moderate reversible capacities^{66,67}. Only recently, after Balaya *et al.*⁶⁸ had demonstrated an exceptional reversibility in the first cycle over a wide voltage range, exhibiting a unique combination of high capacity and high coulombic efficiency, the interest on this intercalation electrode raised. Several studies, mostly focused on the Li storage capacitance of the nano-scaled RuO₂⁶⁹⁻⁷¹, were done. However, the impact of the size and morphology effects on the voltage of the cell RuO₂/Li⁺-electrolyte/Li, which is the main focus of this work, has never been proven before.

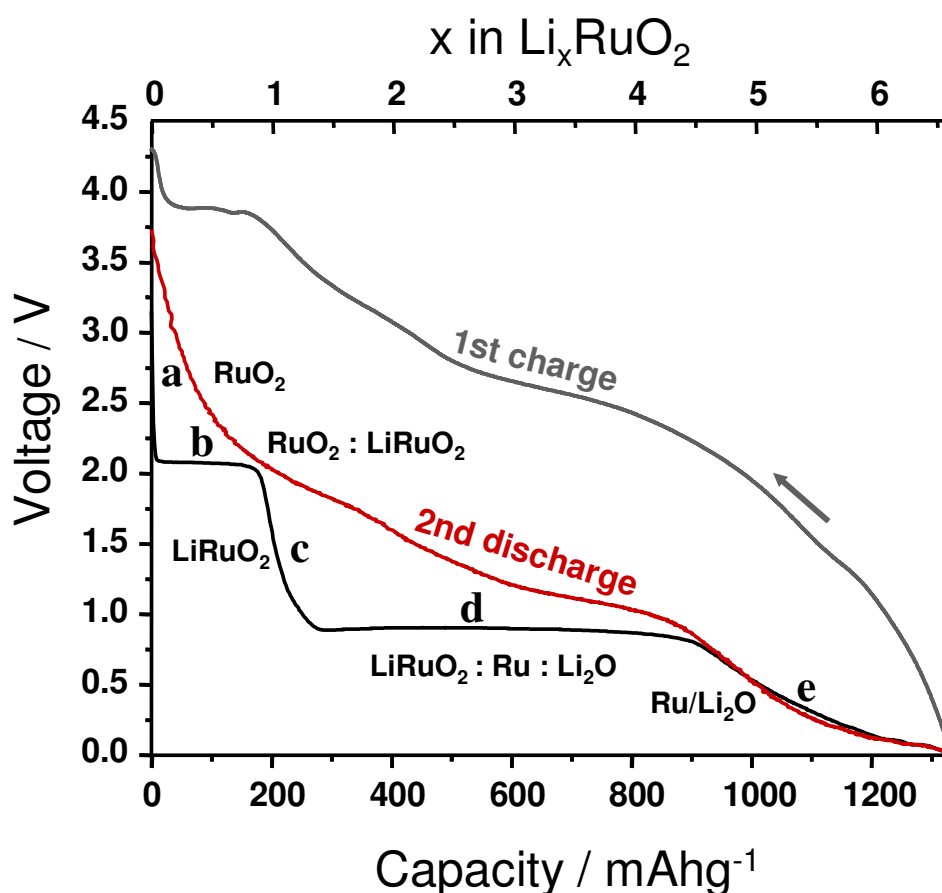


Figure 4: Discharge and charge behavior of RuO₂ electrode against Li at the rate of C/20 (1C denotes a rate at which 4Li per Ru are accommodated in 1 h.); (a)-(e) indicate the different Li storage mechanisms, with the corresponding phases represented near by.

RuO₂ is a unique material in several aspects: it exhibits a favorable combination of high capacity and high coulombic efficiency in the first cycle⁶⁸, very high electronic conductivity (metallic)⁷², high oxygen diffusivity⁷³, comparatively good Li⁺-diffusion⁶⁶. Furthermore, it demonstrates all the known possibilities of Li-storage. Despite the high cost and the fact that the RuO₂ electrode fails after several cycles (possible reasons are ~100% volume expansion during the conversion reaction²⁶ and irreversible structural changes), it is an excellent model material in order to understand the system better and so to be able to improve Li-battery technology.

Figure 4 shows the discharge and charge behavior of the RuO₂/Li half cell at slow rate of C/20. The electrochemical reactions which are nicely evident from the first discharge curve are following: (a) intercalation of *ca.* 0.04Li into the RuO₂ (solid solution); (b) reaction of Li saturated RuO₂ to orthorhombic Li_{0.86}RuO₂, the coexistence of these two phases is revealed by the first plateau at 2.1 V; (c) Li intercalation into the Li_{0.86}RuO₂ until saturation, forming Li_{1.2}RuO₂, followed by the second plateau (d) - conversion reaction by full reduction of Li_{1.2}RuO₂ down to Li₂O/Ru nano-composite (coexistence of Li_{1.2}RuO₂, Ru and Li₂O) and (e) interfacial storage. Furthermore, the discharge and charge reactions are accompanied by reactive Li storage in the solid electrolyte interface (SEI)⁴⁷.

After fully reversible Li removal by the first charge, the obtained RuO₂ turns out to be amorphous⁶³ and hence the second discharge curve (and also the subsequent discharge curves) exhibits a completely different discharge profile due to the different morphology of the electrode. An interesting observation of this work is that the curve of the amorphous sample shows considerably higher overall voltage than the crystalline one – this important feature will be discussed later in detail (see Chapter 4.1.1 and following).

Another remarkable aspect is the following: it is not surprising that during the discharge of crystalline RuO₂ (reaction (b)) we find crystalline Li_{0.86}RuO₂, but it is notable that while lithiation of amorphous RuO₂, obtained electrochemically after the first cycle, reaction with *x*Li ($0.04 \leq x \leq 0.86$) yields (at least partly) the same crystalline Li_{0.86}RuO₂. The two-phase coexistence is demonstrated in Fig. 5a and the hereby reformed crystalline Li_{0.86}RuO₂ is

confirmed by high-resolution transmission electron microscopy (HRTEM) and selected area electron diffraction (SAED) (see Fig. 5b)⁶³.

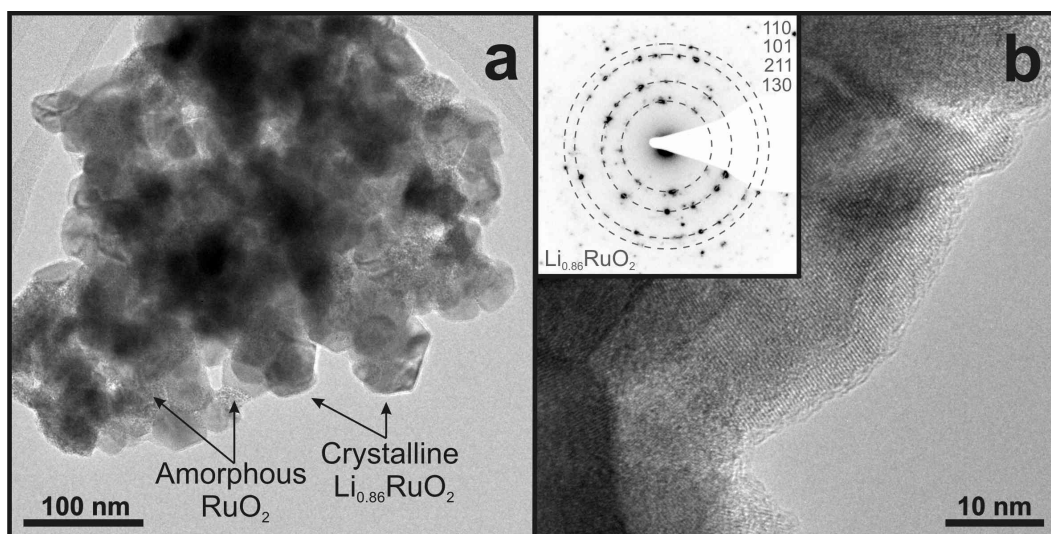


Figure 5: (a) HRTEM observations showing the coexistence of crystalline $\text{Li}_{0.86}\text{RuO}_2$ and amorphous RuO_2 ; (b) HRTEM micrograph and SAED pattern of the crystalline compound $\text{Li}_{0.86}\text{RuO}_2$ formed by Li insertion into amorphous RuO_2 .

In the present work the research is restricted to the reactions (a), (b) and (e), shown in Fig. 4, which are clearly pronounced in the case of the crystalline RuO_2 and less obvious in the case of the amorphous samples ((a) and (b)).

Chapter 3

Experimental

3.1 Materials, Preparation

The following paragraphs give a concise description of the materials used.

3.1.1 RuO₂

RuO₂ (I) (60 nm)

Ruthenium (IV) oxide, RuO_2 (133.07 gmol⁻¹), rutile structure, grain size distribution: 30-100 nm, Johnson Matthey Alfa Products.

RuO₂ (II) (30 nm)

Ruthenium (IV) oxide anhydrous, RuO_2 (133.07 gmol⁻¹), 99.9% purity, rutile structure, grain size distribution: 10-50 nm, Alfa Aesar.

RuO₂ (III) (10 μm)

Ruthenium (IV) oxide, RuO_2 (133.07 gmol⁻¹), rutile structure, grain size distribution: 5-15 μm, obtained by the heat treatment of RuO₂ (I) for 50 h at 800°C.

RuO₂ (IV) (amorphous)

Ruthenium (IV) oxide, RuO_2 (133.07 gmol⁻¹), amorphous. Amorphous particle size distribution depends on the grain size of the initial RuO₂. Amorphous RuO₂ is obtained by deep discharge and charge of the crystalline RuO₂ described above. The exact volume expansion caused by amorphisation is not known. In the case of micro crystalline RuO₂ the grains break into smaller pieces during the LiRuO₂ – formation (see Fig. 21).

RuO₂ (V) (3 nm / 70 h)

Ruthenium (IV) oxide, RuO_2 (133.07 gmol⁻¹), nano-crystalline, grain size: *ca.* 2-3 nm according to HRTEM and 1.8 nm according to X-ray diffraction (XRD). Nano-crystalline RuO₂ was obtained from RuCl₃ (Ruthenium(III) chloride hydrate, 99.9% (36% Ru), ABCR) in the following way: 250 mg of RuCl₃ were dissolved in 90 ml of bi-distilled water and the solution was heated at 180° C in an autoclave, made of stainless steel, for 70 h. The resulting black precipitate was separated from the liquid and was washed with bi-distilled water until the pH of the washing water was neutral (indication that during the reaction formed HCl is removed). The wet black solid was first dried at 70 °C in the air atmosphere and then at 80 °C over 70 h in vacuum.

3.1.2 Metallic Ru**Ru (I)**

Ruthenium (0), Ru (101.07 gmol⁻¹), hexagonal. Ru (I) was obtained from RuO₂ (II) by heat treatment in the hydrogen atmosphere. The completeness of reduction process was proven by thermo-gravimetry (TG). Detected particle size distribution is *ca.* 10-40 nm (HRTEM) and, according to the line broadening of XRD-signals, average crystallite size is *ca.* 30 nm. Surface area was proved by BET analysis and has a value of 29.6 m²g⁻¹.

Ru (II)

Ruthenium (0), Ru (101.07 gmol^{-1}), hexagonal. Ru (II) was obtained from RuO_2 (III) by heat treatment in the hydrogen atmosphere. The completeness of the reduction was proven by TG. Particles are very porous and 5-15 μm sized, average crystallite size is *ca.* 20 nm. Surface area obtained from the BET analysis is $8.83 \text{ m}^2\text{g}^{-1}$.

Ru (III)

Ruthenium (0), Ru (101.07 gmol^{-1}), hexagonal. Ru (III), ABCR, 99.8 % purity, particle size according to ABCR: 60 μm , detected particle size *via* scanning electron microscopy (SEM): 200-600 nm.

3.2 Materials, Characterization

3.2.1 RuO_2

XRD

All XRD measurements at room temperature were performed using PHILIPS device PW 3710 applying CuK α irradiation (40kV/30mA) and at higher temperatures PHILIPS device XPert PW3710 spectrometer with a high temperature camera HTK 2 from Anton Paar was used. The patterns were identified by the program "X`Pert HighScore" containing databases JCPDS-ICDD (Joint Committee on Powder Diffraction Standards - International Center for Diffraction Data).

Figure 6 shows a comparison of RuO_2 with different particle sizes/morphologies which were recorded at room temperature. The patterns in the figure are arranged with increasing particle size from amorphous (IV) to 10 μm sized RuO_2 (III).

Amorphous RuO_2 exhibits a small fraction of crystalline RuO_2 due to the electrochemical preparation method (see pattern (IV) in Fig. 6). To avoid any additional signals, pure RuO_2 powder was applied as an electrode, without

adding any additives which are usually used to improve the particle network and the contact to the current collector. So, some isolated particles could not be involved into the electrochemical reaction. The appearance of broad signals with the first maximum at $2\Theta = 33^\circ$ is similar to a glassy phase.

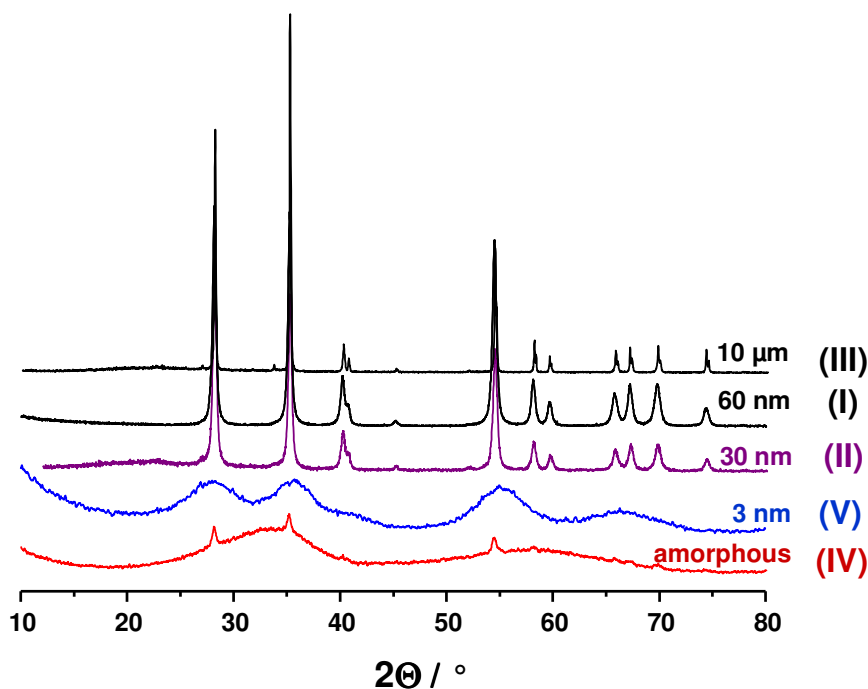


Figure 6: X-ray diffraction patterns of RuO₂-samples (I)-(V).

Nano-crystalline RuO₂ shows very broad signals too, but in contrast to amorphous RuO₂, the maxima reflect the characteristic RuO₂ signals. Calculation of the average crystallite size from the signal broadening, applying Scherrer's equation⁷⁴, yielded 1.8 nm.

With the increasing particle size from 20 nm (RuO₂(II)) up to 10 μm (RuO₂(III)), as expected, the signals become sharper and the resolution of overlapping peaks improves.

HRTEM/SEM

HRTEM micrographs were taken using Philips CM30 ST (300kV) device and SEM photographs were taken using a Tescan VEGA TS 5130MM.

In Figure 7 an overview of RuO₂ micrographs with different particle sizes/morphologies is presented. Micrographs (a), (b) and (c) are displayed in the same magnification. Here one can see a clear difference between

amorphous (a), nano-crystalline (b) and crystalline (c) RuO₂. Amorphous RuO₂ does not exhibit any crystalline order. In the case of nano-crystalline RuO₂ one can see particles with the size of only 2-3 nm. The micrograph (c) shows a RuO₂ crystal of *ca.* 30 nm.

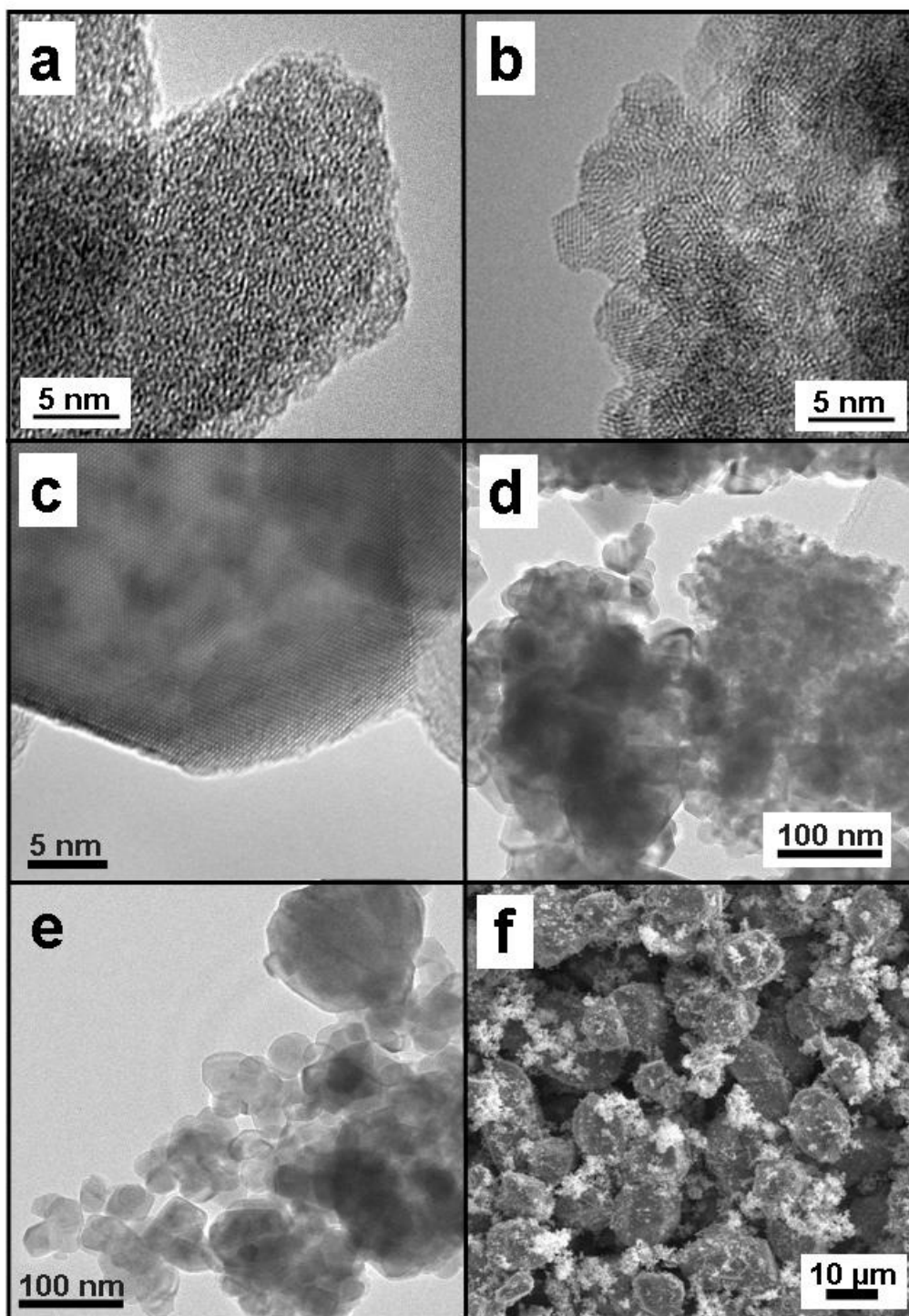


Figure 7: HRTEM/SEM micrographs of RuO₂ samples (I)-(V): (a)-(IV), amorphous; (b)-(V), 3 nm; (c, d)-(II), 30 nm; (e)-(I), 60 nm; (f)-(III), 10 μm.

The micrographs (d) and (e) illustrate the difference in the particle size distribution between RuO₂ (II) (10-50 nm) (d) and RuO₂ (I) (30-100 nm) (e). (f) is the SEM photograph of RuO₂ (III). Apart from the big RuO₂ particles, the powder exhibits a small fraction of the initial RuO₂ (I) which is visible as a bright powder on the surface of the big particles.

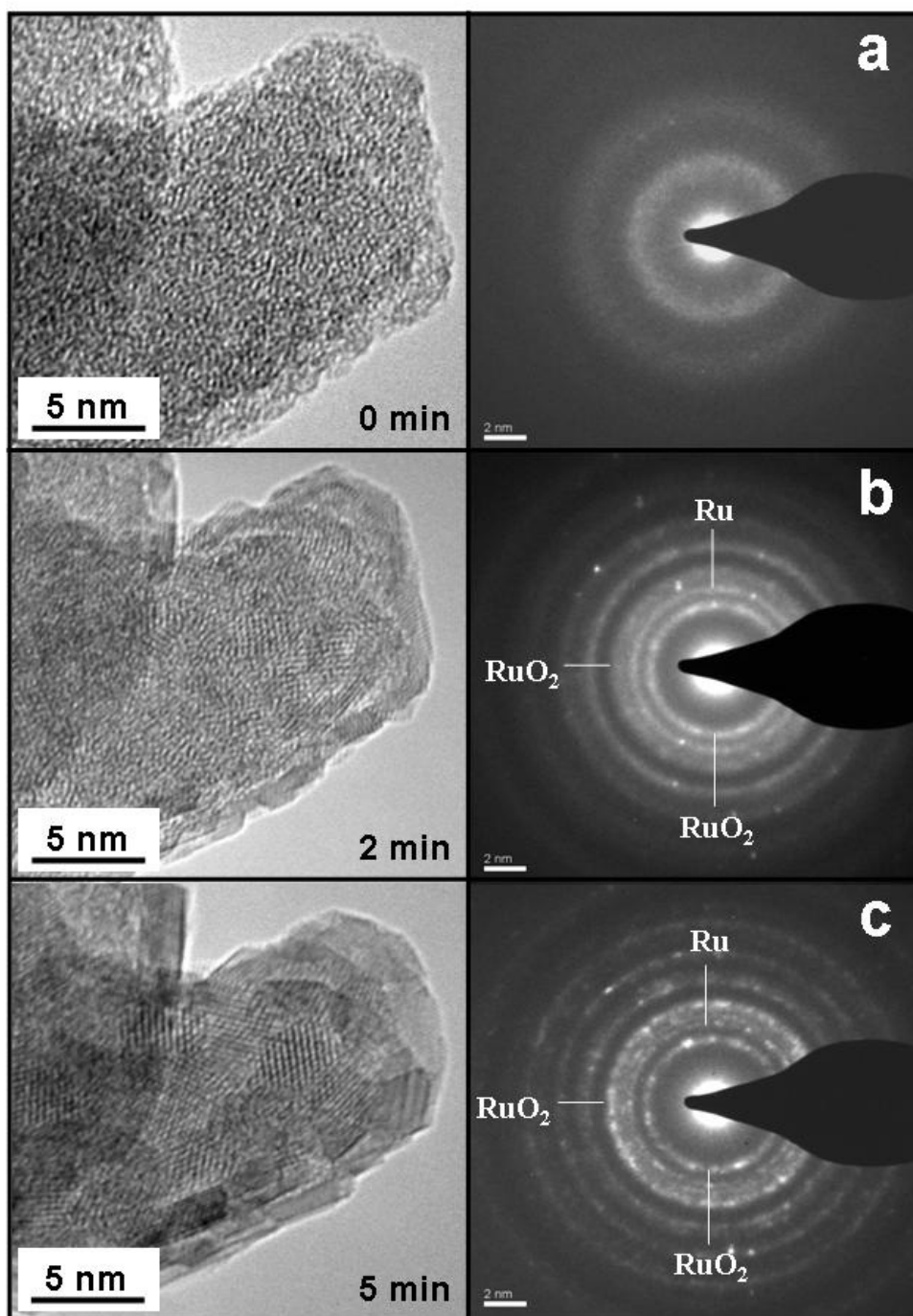


Figure 8: Influence of the electron irradiation on the amorphous sample during a TEM analysis.

During the HRTEM measurements we realized that amorphous samples are very sensitive to the high power electron irradiation illumination and long irradiation times. This feature led already to misleading conclusions in some previous investigations⁶⁸. The samples started to crystallize after several tenths of seconds under additional reduction to metallic Ru. The micrographs and the corresponding SAED patterns of the test series on amorphous RuO₂ are shown in Figure 8. The data were taken with the time lag of few minutes.

Raman

Raman measurements were performed on Jobin Yvon Typ V 010 single grating spectrometer, equipped with a Notch filter and a peltier cooled CCD camera. The spectra are taken in quasi-backscattering geometry using the linearly polarized 632.817 nm line of a He/Ne gas laser with power less than 2 mW, focused to a 15 μm spot through a 20x microscope objective onto the sample surface.

The figure below shows Raman spectra of RuO₂ samples (I)-(V) taken at room temperature. The spectra are ordered with increasing particle size from amorphous (IV) to 10 μm sized RuO₂ (III).

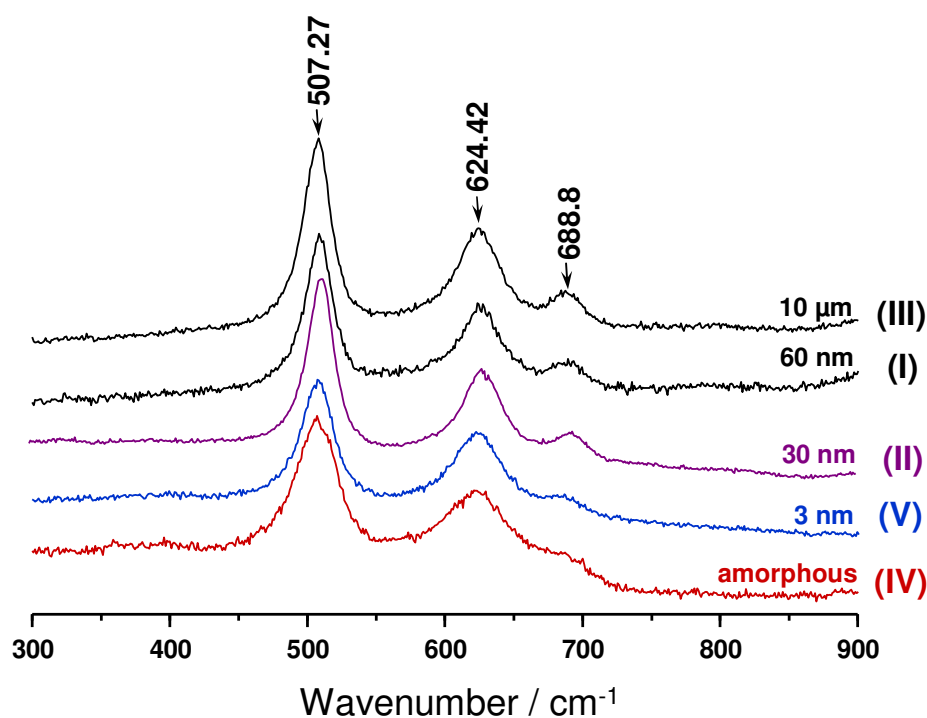


Figure 9: Laser Raman spectra acquired from different RuO₂-samples (I)-(V) using a 632.817 nm He/Ne laser.

All RuO₂ powders exhibit typical bands at *ca.* 507.3, 624.4 and 688.8 cm⁻¹ corresponding to E_g, A_{1g} and B_{2g} modes. The bands are shifted compared to the single crystal rutile-type RuO₂ which is characterized by four bands⁷⁵ at 97(B_{1g}), 528, 646 and 716 cm⁻¹ (D_{4h}). Similar shifts and broadening of Raman bands are reported in the literature for small crystallite sizes of RuO₂⁷⁶, RuO₂ aerogels⁷⁷ and thin films⁷⁸.

Comparing the spectra in Figure 9, one can recognize that the bands of amorphous (IV) and nano-crystalline (V) RuO₂ are slightly broader in contrary to the crystalline ones due to the lower symmetry in more disordered structure.

XPS

XPS (X-Ray photoelectron spectroscopy) analyses were carried out on a Kratos AXIS ULTRA Multi-Technique Electron Spectrometer.

3.2.2 Metallic Ru

XRD

In addition to TG, XRD analysis (shown in Figure 10) ensures that in the case of Ru(I) and Ru (II) there is no RuO_2 left after the reduction by H_2 . The signals of Ru(I) and Ru (II) are much broader compared to the commercial Ru (III), which is again an evidence for very small crystallite sizes. According to Scherrer's equation, reduction of RuO_2 in H_2 atmosphere yielded in average 20 nm sized Ru crystallites from 10 μm big RuO_2 crystals and 30 nm sized crystallites from 10-50 nm sized RuO_2 .

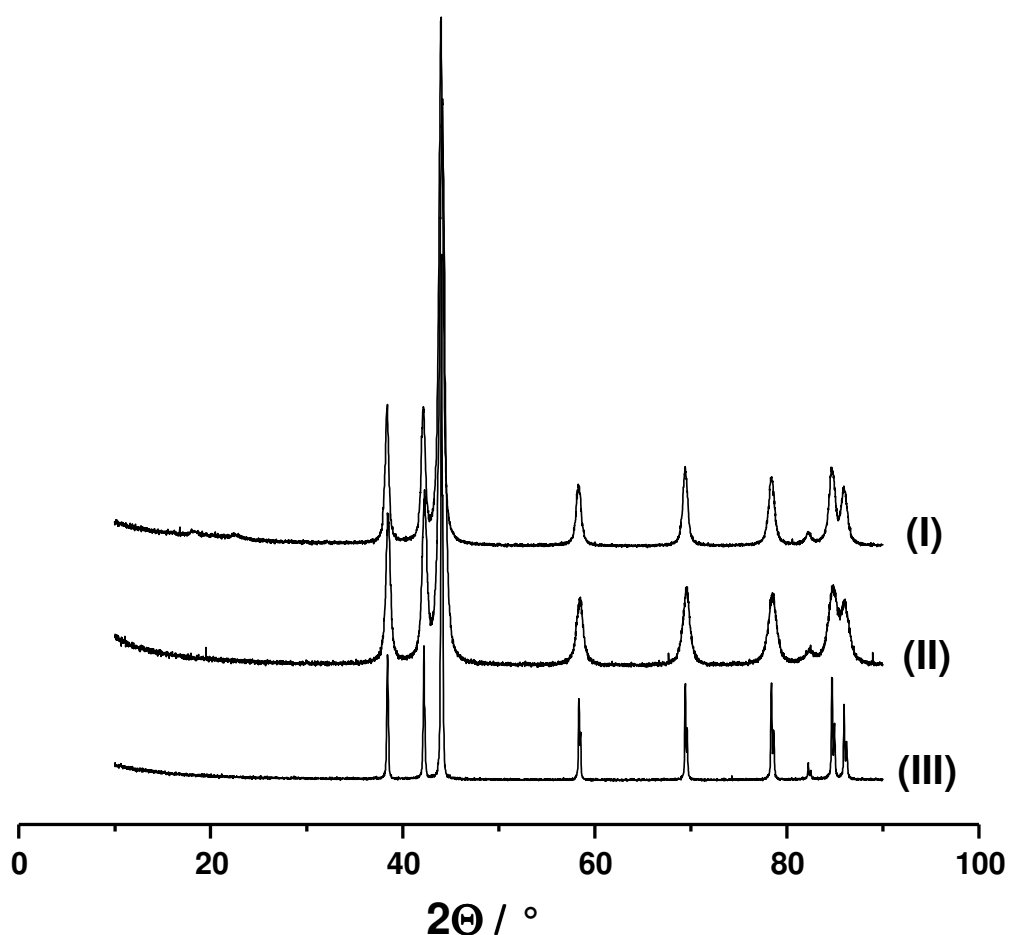


Figure 10: XRD patterns of metallic Ru (I)–(III).

SEM/HRTEM

Figure 11 gives an overview over Ru (I)-(III). The “microstructure” of the samples is quite different. Ru (I), shown in micrograph (a), is a powder of porous agglomerates (*ca.* 100 nm) composed of 10-50 nm sized Ru-crystallites (HRTEM).

Ru (II), shown in micrograph (b), consists of big (5-15 μm) and porous framework. There are two different pore distributions, 1-2 μm sized micro pores according to HRTEM and 4-12 nm nano-pores due to the BET analysis which were formed by elimination of oxygen from RuO_2 (III) *via* reduction by hydrogen. The crystallites, which form the framework, are according to XRD 20 nm sized. Please note that in the case of Ru (I) which was obtained in the same way, *via* reduction by hydrogen, the particles are not porous. The initial RuO_2 particles in this case are very small (10-50 nm), so that the rearrangement of the atoms is much easier and non-porous particles of this dimensions seem to be clearly preferred in order to minimize the high surface energy.

The commercial Ru-powder (c) is composed of big very porous agglomerates (5-30 μm) consisting of 200-600 nm sized Ru-crystallites.

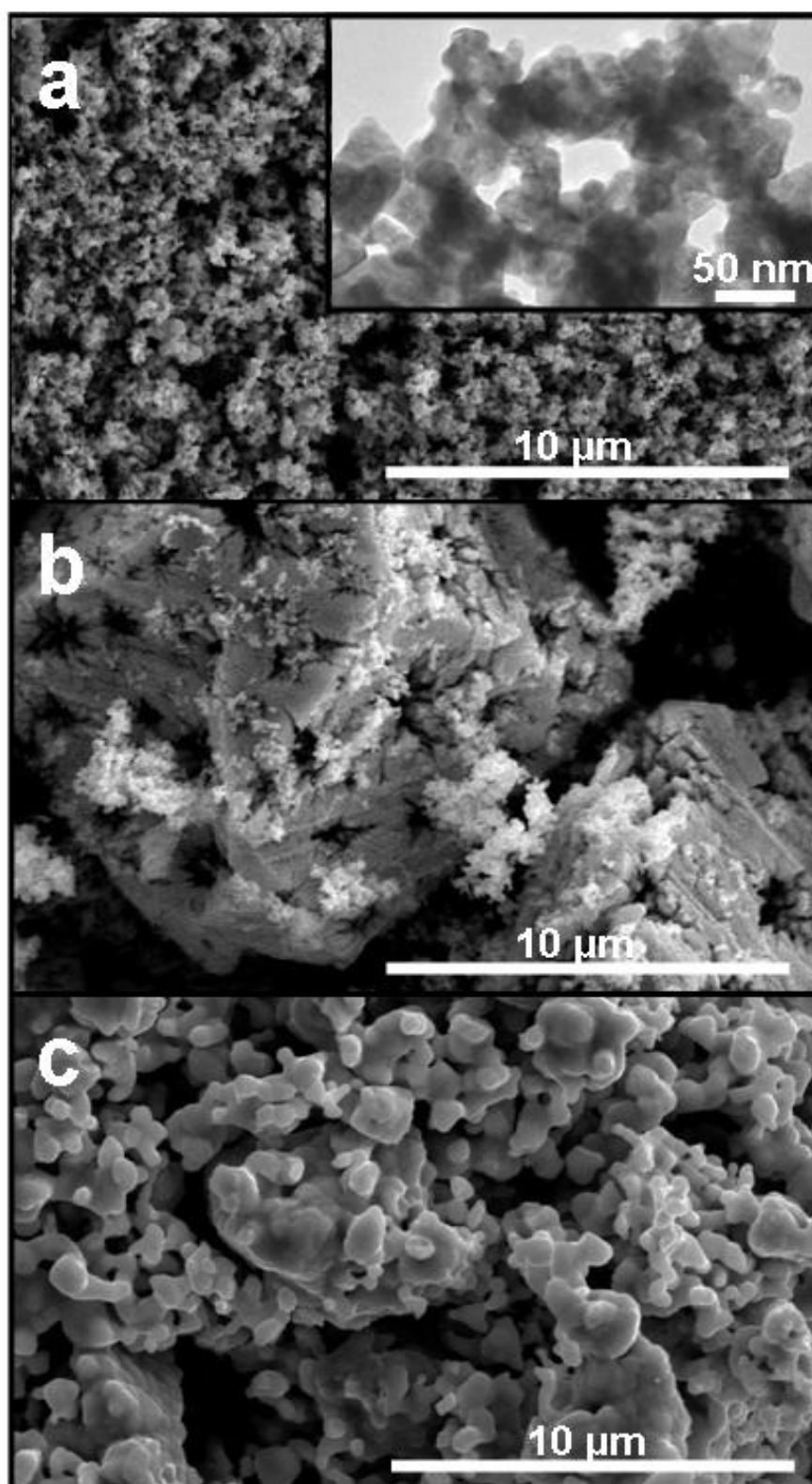


Figure 11: HRTEM/SEM micrographs of Ru samples (I)-(III): (a)-(I), (b)-(II) and (c)-(III).

3.3 Hydrous Nano-Crystalline RuO₂

RuO₂ nano-particles of the here achieved dimensions deserve a more detailed description. Several methods were tried to prepare nano-crystalline RuO₂ with the particle size of < 5 nm, to be able to see an obvious impact of downsizing of the particles on the energetics in the Li - RuO₂ system. In the following synthesis process and characterization along with the estimation of the water content of the nano-particles are presented.

3.3.1 Synthesis and Characterization

The most promising preparation method was based on the previous investigations of Music *et al.*^{76,79} The method, described in literature, was simplified and modified as followed: An aqueous solution of hydrated RuCl₃ (Ruthenium(III) chloride hydrate, 99.9% (36% Ru), ABCR), was prepared by dissolving of 250 mg of RuCl₃ in 90 ml of bi-distilled water. The solution was autoclaved for 2 h at 180 °C. The resulting black precipitate was separated from the liquid and was washed with bi-distilled water until the pH of the washing water was neutral. The wet black solid was first dried at 70 °C in the air atmosphere and then at 80 °C over 70 h in vacuum. As a result ~ 1-2 nm sized RuO₂ crystallites with amorphous hydrous grain boundaries were obtained, as shown in the HRTEM micrograph in Fig. 12.

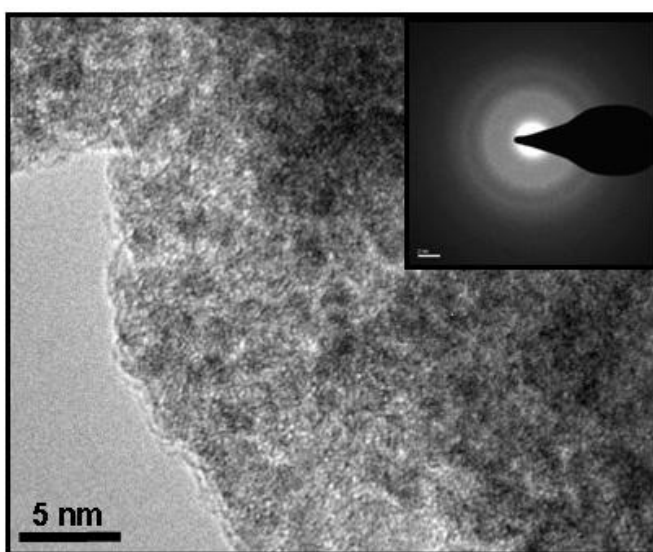


Figure 12: HRTEM micrograph and SAED pattern of RuO₂ prepared by autoclaving of the RuCl₃ solution at 180 °C for 2 h.

To find the best conditions to get rid of the amorphous phase, the powder was heated in air atmosphere with the rate of 5 °C per minute and after every 50 °C the temperature was kept for 2 h. One XRD pattern was recorded at every 50 °C stage and the grain size was obtained using the Scherrer's method (see Fig 13). However, after heat treating the powder in the described way up to 200 °C and 300 °C and subsequent using this samples for GITT and OCV measurements, the obtained results were not reproducible what indicates a non-homogeneous particle growth. So, the preparation method was modified further by autoclaving of the RuCl_3 solution for 70 h instead of 2 h. This was proved to be successful, hence the obtained powder, according to HRTEM shown Fig 14, did not exhibit any amorphous hydrous grain boundaries any more and consisted of well crystallized particles with homogeneous size distribution in the range of 2-3 nm. Three types of powders prepared by this hydrothermal method with different autoclaving times, *i.e.* 2 h, 20 h and 70 h (where labeling "70 h" also corresponds to the labeling "3 nm"), were investigated and compared. The "3 nm" powder, due to low water content and homogeneous particle size distribution in a very small range, is additionally included into the experimental series along with amorphous, 10 μm , 60 nm and 30 nm sized powders.

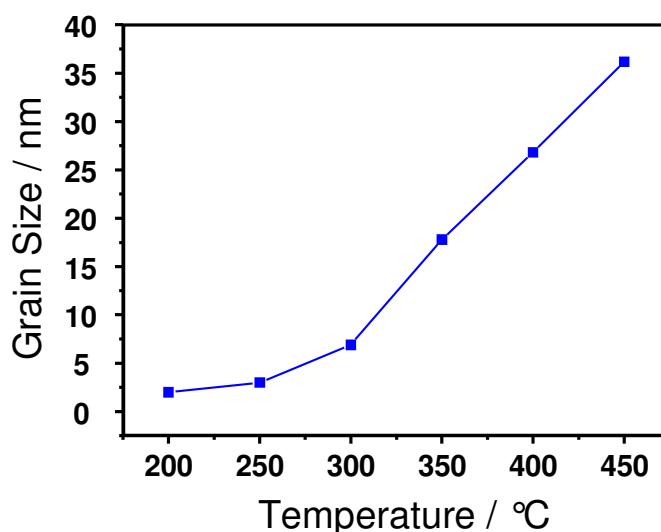


Figure 13: Response of the particle growing to a 2 h heat treatment at every 50 °C step.

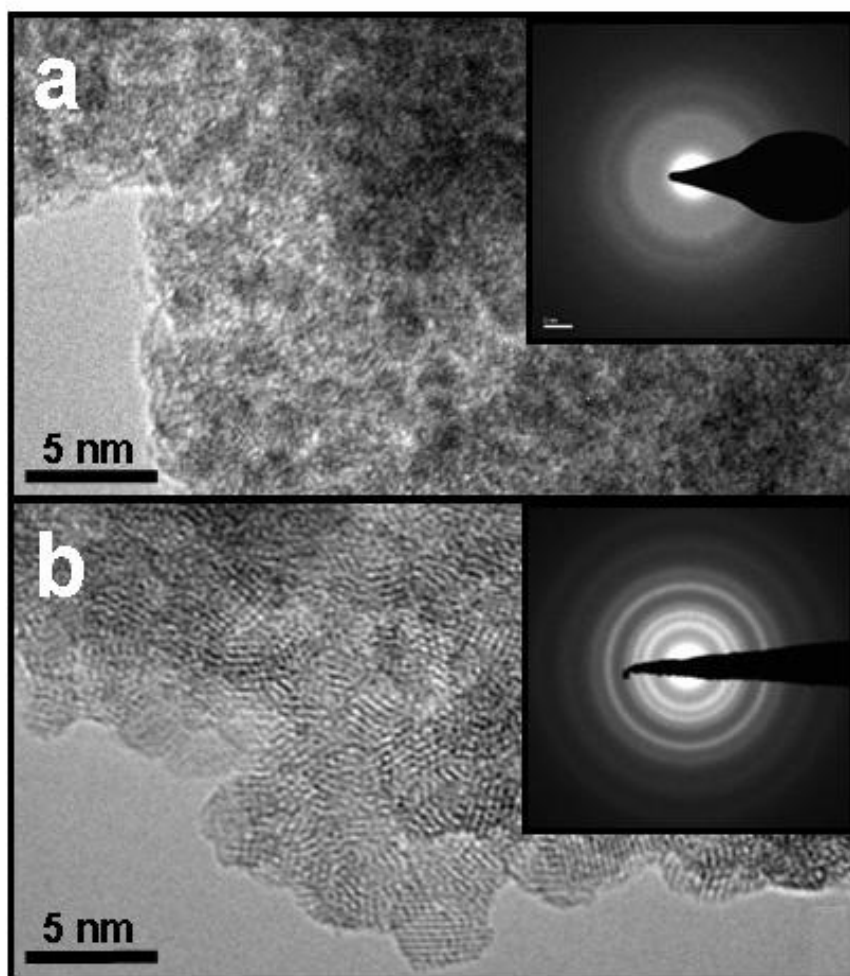


Figure 14: Comparison of the HRTEM micrographs and SAED patterns of powders obtained after autoclaving of RuCl_3 solution at $180\text{ }^\circ\text{C}$ for 2 h (a) and 70 h (b).

XRD Analysis

In Fig. 15 the XRD analysis of hydrothermally prepared powders is presented. For comparison, results of amorphous and crystalline powders and an “anhydrous” commercially available RuO_2 nano-powder (ruthenium oxide anhydrous, 99.9%, Alfa Aesar & GmbH Co. KG) which will be used as a reference for the water content are displayed in the Figure too. The hydrothermal powders show — in contrast to the amorphous sample — very broad signals corresponding to the crystalline pattern. With longer autoclaving time and so decreasing ratio of amorphous hydrous grain boundaries and increasing particle size, the signals became more pronounced. The reference nano-powder, labeled “anhydrous”, seems to have a very broad particle size

distribution, as the basis of the signals is very broad and the tips are fairly sharp. Since, owing to this diversity, the Scherrer's method does not deliver any reasonable results, by comparison with the other patterns, the maxima of the particle distribution may lie at 2-3 and 10-15 nm.

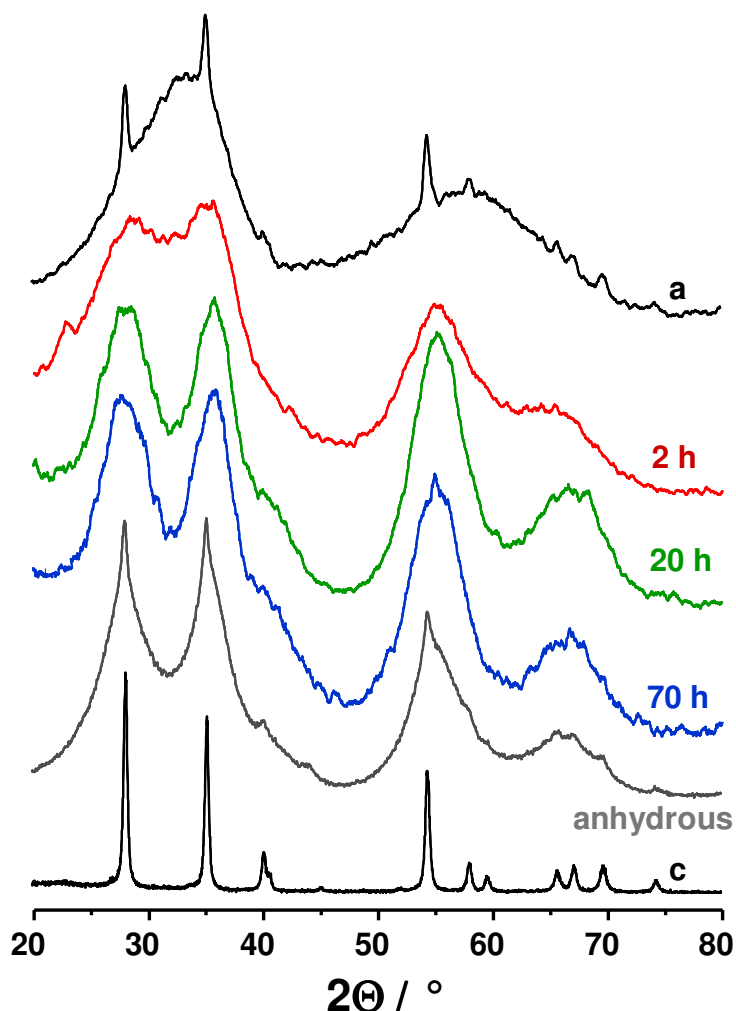


Figure 15: XRD patterns of (a) amorphous, (2 h, 20 h and 70 h) hydrothermally prepared, anhydrous (Alfa Aesar) and (c) crystalline (30 nm) reference RuO_2 powders.

Raman Analysis

Raman analysis of the hydrothermal powders showed, in the case of the for 2 h autoclaved sample, apart from the expected characteristic peaks of RuO_2 modes an additional signal at 393 cm^{-1} . This signal can be attributed to the hydrous amorphous grain boundaries⁷⁸ (see Fig. 16).

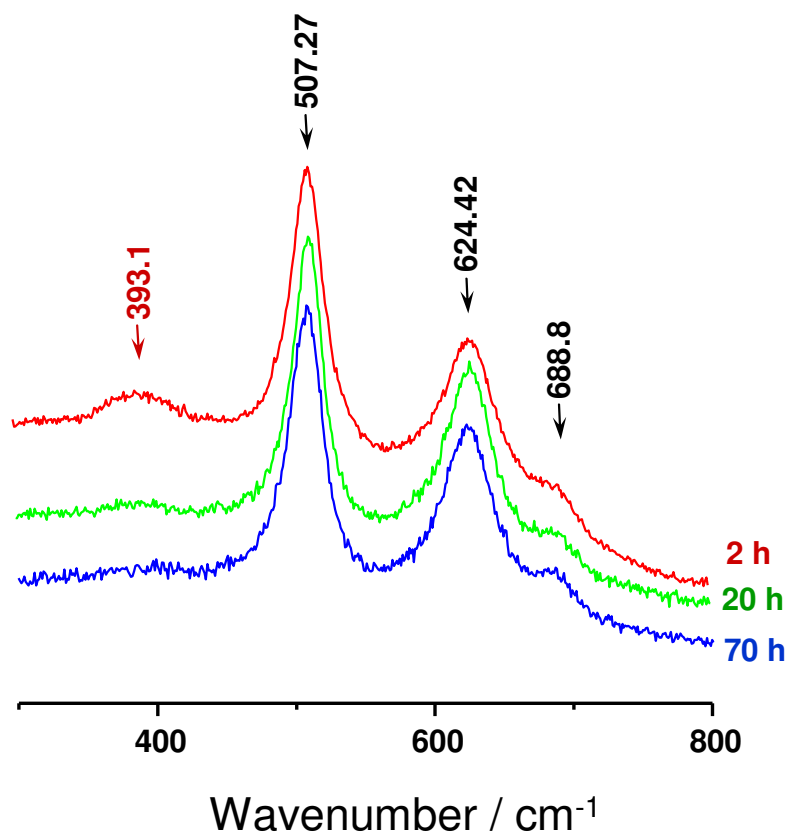


Figure 16: Raman spectra of the hydrothermally prepared RuO₂ powders.

TG/MS Analysis

A better clue as to the water content in the samples gives the TG performed in air atmosphere along with the corresponding MS (mass spectroscopy) analysis, shown in Fig. 17.

According to the weight loss, presented in Fig. 17 (a), the powder autoclaved for 2 h consists of RuO₂ × 1.13H₂O, and the “anhydrous” sample exhibits the composition RuO₂ × 0.3H₂O. It is not possible to correlate the composition of “20 h” and “70 h” powders directly with the weight loss, since the corresponding MS analysis shows a contamination with the carbon which causes additional weight loss. Contamination with hydrocarbons can be excluded, because in the presence of hydrocarbons CO₂ and H₂O signals appear at exactly the same temperature. So, the water content of the “20 h” and “70 h” samples can be roughly estimated from the difference in the areas of the

relative H₂O signals shown in Fig. 17 (b) by using established values of “anhydrous” and “2 h” samples. The “70 h” sample seems to have a similar composition to the “anhydrous” powder and the “20 h” powder must approximately consist of RuO₂ × 0.6H₂O.

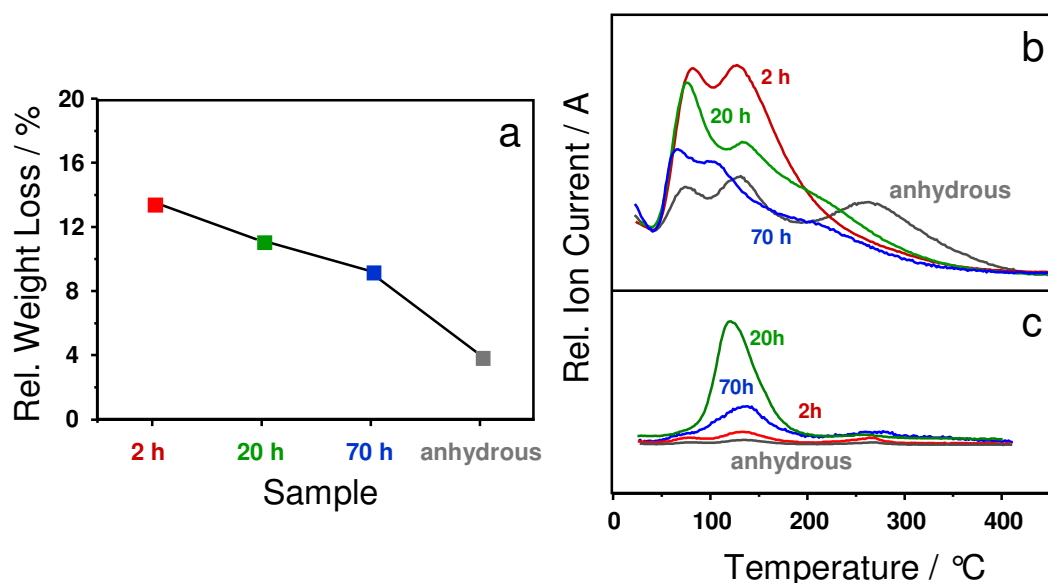


Figure 17: TG (a) and MS (b, c) data of the hydrothermally prepared samples and the anhydrous reference sample. In (b) and (c) the relative signal intensity of the mass 18 and 44 against the temperature is represented.

Interestingly, the MS analysis shows three different water signals. The first one is most probably due to the evaporation of the physisorbed water on the surface of the powder, second and third could be attributed to the condensation of the terminating OH-groups on the surface of the nano-particles under particle growth. The difference in the signal patterns between the hydrothermally produced powders and the commercial “anhydrous” sample could be due to the difference in the secondary structure of powder, *e.g.* particle size distribution or agglomeration. As already noticed in the HRTEM micrograph and XRD analysis, the particle size distribution of the hydrothermally prepared powders is very homogeneous, so only one main signal for condensation of the terminating OH-groups (second peak) is expected and also seen, whereas further condensations are observed as a very broad shoulder (Fig. 17 (b), “20 h” and “70 h” at 150-250 °C). Two clearly pronounced OH-condensation signals (see Fig. 17 (b), “anhydrous” at ~ 150 and 260 °C) could be caused by a powder exhibiting two different maxima in size distribution. First maxima must be in

the same size range like the hydrothermally prepared powders which condensate first reaching the size of the bigger ones and then condensate further together with the bigger particles. In the Fig. 15 presented XRD analysis supports this possibility; small (~ 2-3 nm) and big (~ 10-15 nm) particles are present at the same time.

A very important fact is that in this nano-size range it is hardly possible to avoid presence of a measurable amount of terminating OH-groups on the surface of the particles.

3.4 Electrochemical Cell

For all electrochemical tests a commercially available two-electrode Swagelok™ type cell was used. The cell was assembled in a glove box under Ar atmosphere. To ensure the inert atmosphere during the measurements the cell was placed in an airproof glass bottle filled with Ar. The construction of the cell is shown in Figure 18.

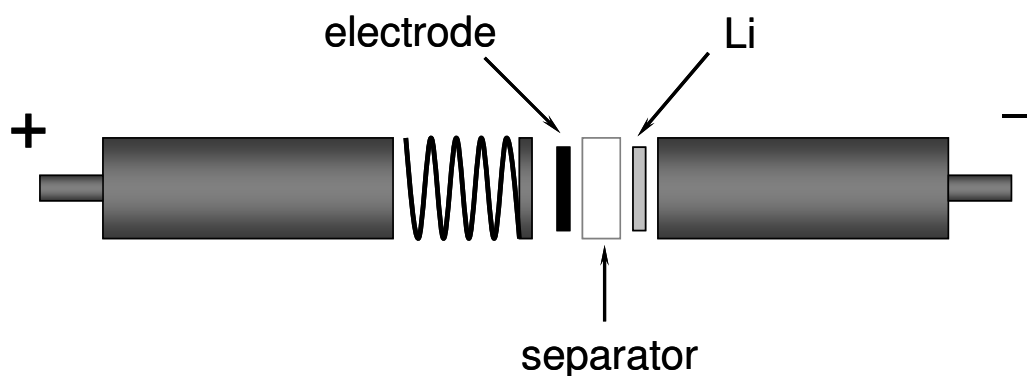


Figure 18: Electrochemical cell.

The negative counter-electrode (Li-foil, Aldrich, 99,99 %,) and the positive working electrode (RuO_2 , Ru) are separated by a glass micro fibre filter (Whatman) which is soaked by the 1 M LiPF_6 electrolyte solution with the solvent being a 1:1 mixture of EC/DMC (ethylene carbonate/dimethyl carbonate, Merck).

3.5 Electrode Preparation

Three types of electrodes were used as working electrodes: (i) pure Ru (I-III) or RuO₂ (I-V) powder, (ii) RuO₂ (I-V) powder mixed with polyvinylene difluoride (PVDF, Aldrich), depending on the particle size the weight fraction of the active mass was 92-96.7 % and (iii) RuO₂ (I-V) mixed with carbon black (CB), graphite (GP) and PVDF with mass ratio of 10:1:1:1.36 (active mass: 74.85 weight%).

The pure powders were uniformly distributed on the whole area (circle with diameter of 1 cm) of the current collector of the Swagelock™ half-cell and covered by the separator before continuing the cell assembling in the glove box. The electrodes (ii) and (iii) were prepared in the following way: first the solid components were carefully ground to a homogeneous mixture and then some PVDF solution (17 mg/ml) in N-methyl-2-pyrrolidone (NMP) was added, so that the consistency of the resulting paste allowed for a homogeneous distribution on the Ti-foil. After drying under IR-lamp, the electrode was additionally dried in the vacuum oven at 80 °C for *ca.* 24 h. To achieve a smoother surface and to improve the particle contact, the electrode was subsequently pressed at 25 kN with the help of an uniaxial press. At the end the electrode was cut into circles with 1 cm diameter.

3.6 Electrochemical Tests

3.6.1 Discharge/Charge, Capacity

The discharge and charge cycling experiments were performed at room temperature using an Arbin MSTAT system.

The rate applied for charge and discharge experiments was C/20. The magnitude of the normalized rate is termed νC if the total theoretical capacity (Q_{th}) is charged (discharged) within $1/\nu$ hour. The theoretical capacity Q_{th} of RuO₂ is calculated as followed:

$$Q_{th} = \frac{n \times F}{M} = 805.663 \text{ mAhg}^{-1}, \quad (4)$$

where n is the number of transferred electrons, F is the Faraday constant and M the molar weight of RuO_2 . We consider here the full discharge and charge which means the full reduction of RuO_2 to Ru . It theoretically requires transfer of 4 electrons leading to $\text{Ru} + 2\text{Li}_2\text{O}$.

The real capacity Q was estimated using the following relation:

$$Q = \frac{I \times t}{m}, \quad (5)$$

with I the applied current, t the time and m the weight of the active mass. In Figure 19 an example of the first discharge (a) and charge (b) of crystalline RuO_2 is demonstrated.

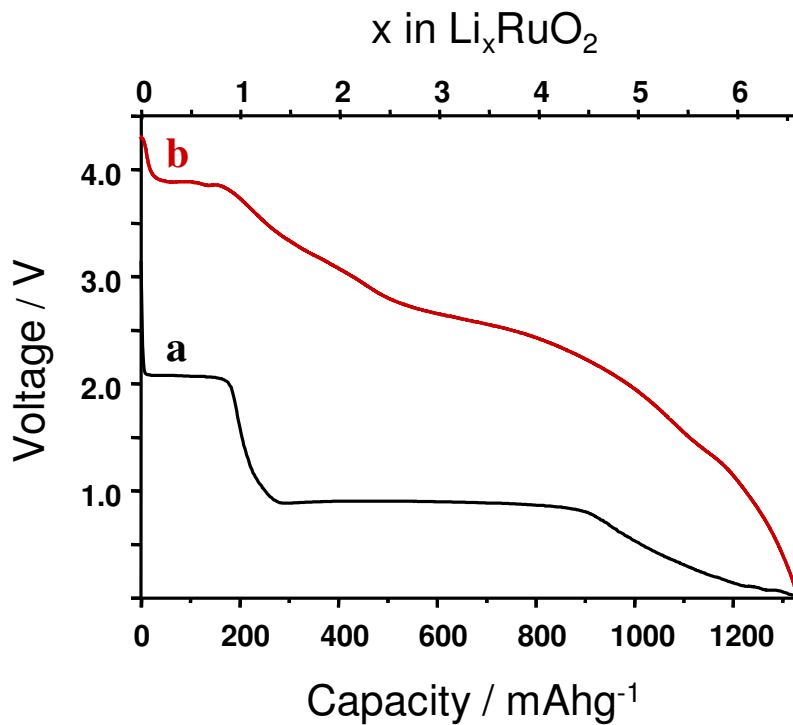


Figure 19: First discharge (a) and charge (b) of crystalline RuO_2 sample at a rate of $C/20$.

3.6.2 GITT

GITT (galvanostatic intermittent titration technique) experiments, in the literature also called time resolved galvanostatic coulometric titration experiments, were performed at room temperature using an Arbin MSTAT system as well.

In the Figure 20 two different experiments on the same sample are shown: (b) refers to the usual discharge curve recorded at the rate of C/20 and (a) is a GITT experiment. In contrast to usual discharge, GITT is performed incorporating very small amounts of Li step by step, using a very low, constant current ($10\mu\text{A} \approx C/140$) which is applied for only 1 h per step with open-circuit equilibration time of at least 20 h between the steps. This results in the voltage close to the equilibrium state. The difference in voltage between the experiment (a) and (b) is the polarization term η , which disappears for vanishingly small current.

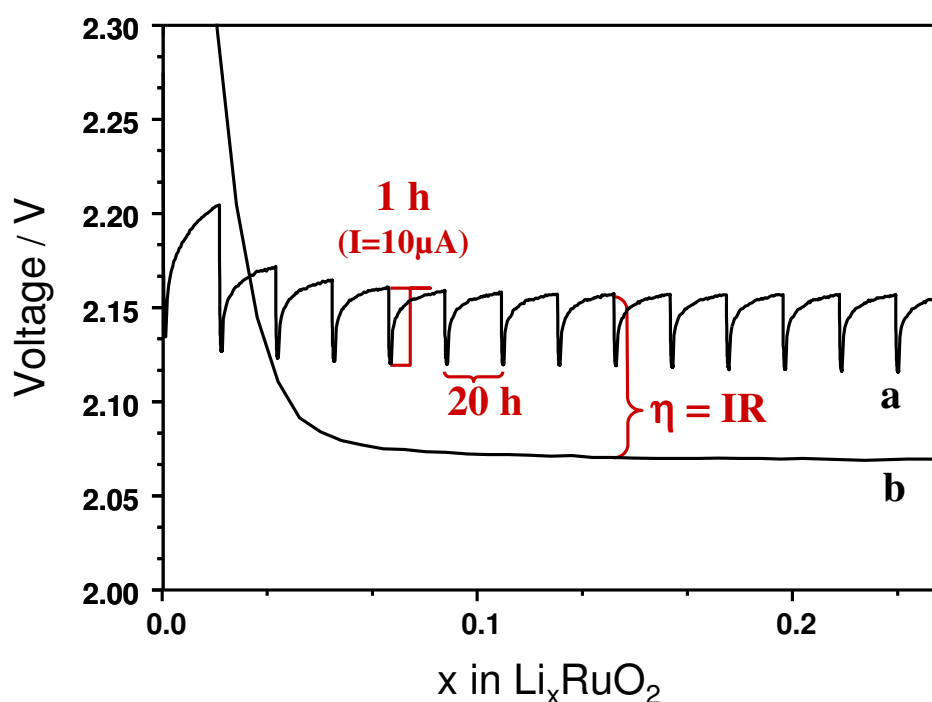


Figure 20: An example of GITT experiment on crystalline RuO₂; curve (a) denotes the GITT experiment and curve (b) is a discharge at a rate of C/20.

3.7 Calculation of Diffusion Coefficient and Li^+ -Conductivity

From the potential response to the small constant current pulses during the GITT experiment (see the red marked ranges in the Figure (21)) it is possible to estimate the chemical diffusion coefficient of Li in the single phase regime.

This method has been made popular by Weppner and Huggins⁸⁰ in the context of investigating solids and since then it has been used as a standard method to obtain chemical diffusion coefficients of Li^+ in Li-battery electrode materials⁸¹⁻⁹³. If also transfer resistances are of significance, the evaluation can be quite complex⁹⁴⁻⁹⁶. Owing to the electrochemical properties of RuO_2 we assume diffusion control that is confirmed by the functional form of voltage vs. time. This assumption is corroborated by the fact that the values for chemical diffusion coefficient which were obtained in the present work using GITT method are similar to the values which were reported by Armand⁶⁶. Armand applied potential sweep voltammetry on RuO_2 thin films which is a completely independent technique.

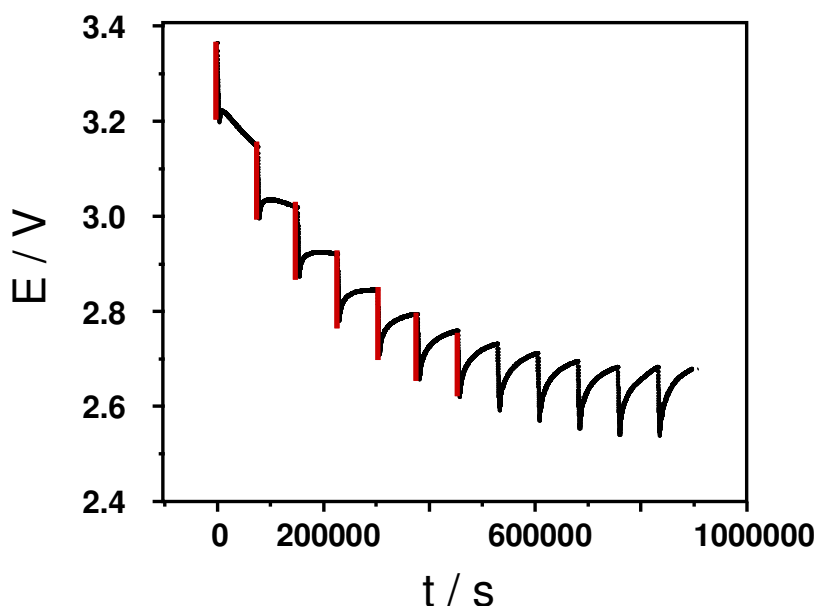


Figure 21: GITT raw data for calculation of chemical diffusion coefficient and conductivity of Li^+ .

For the calculation of chemical diffusion coefficient \tilde{D} , the following equation⁸⁰ was used:

$$\tilde{D} = \frac{4}{\pi} \left(I \frac{V_m}{zFS} \right)^2 \left(\frac{dE}{dx} / \frac{dE}{d\sqrt{t}} \right)^2, \quad (6)$$

with I , V_m , S , z and F denoting polarization current (10 μA), molar volume of RuO_2 (19.09 $\text{cm}^3 \text{mol}^{-1}$), surface area of the sample (πr^2 , with $r = 0.5 \text{ cm}$), charge number ($z = 1$) and the Faraday's constant, respectively. All these values are already known or can be determined from the GITT curve. The short time approximation $dE/d\sqrt{t}$ is only valid for times $t \ll L^2/\tilde{D}$, where L is the thickness of the sample. dE/dx is the slope of the coulometric titration curve which is found by plotting the steady-state voltages, against the composition calculated from:

$$\Delta x = \frac{I \times t \times MW}{m \times z \times F}, \quad (7)$$

where I , t , MW , m , z and F are the constant current, the time interval, the molecular weight of RuO_2 , the active mass, the number of transferred electrons and Faraday's constant.

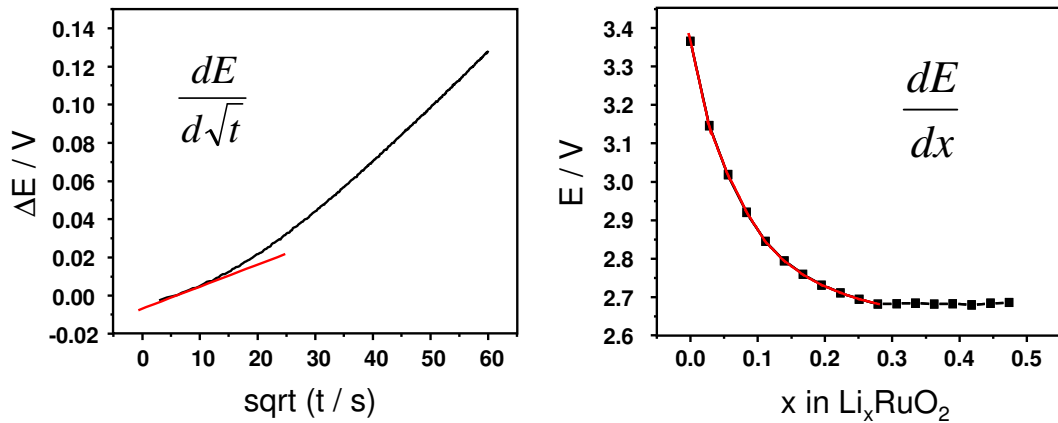


Figure 22: Examples for determination of $dE/d\sqrt{t}$ and dE/dx .

In Figure 22 typical examples of determination of $dE/d\sqrt{t}$ and dE/dx are shown. Black curves correspond to the experimental data and the fitting lines are highlighted by red color.

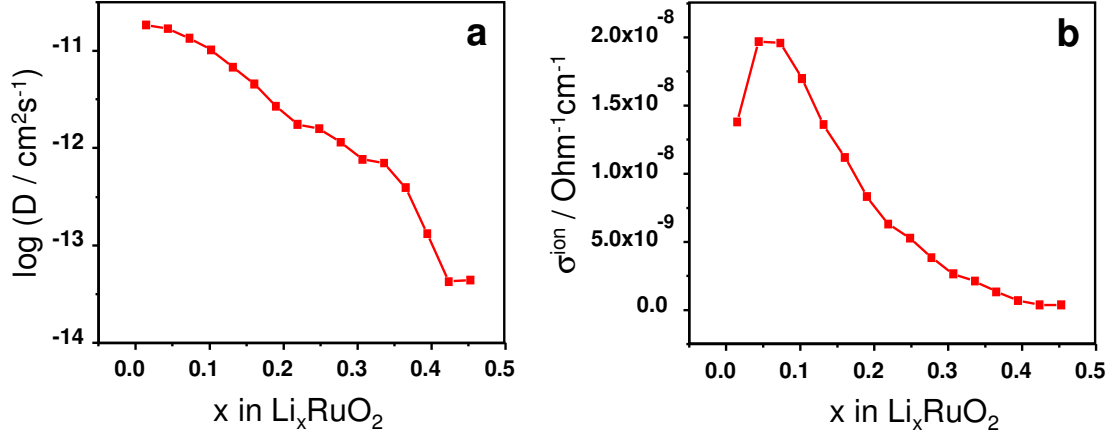


Figure 23: Typical plots of chemical diffusion coefficient of Li (a) and Li⁺ conductivity (b) calculated from \tilde{D} , against Li ratio in RuO₂.

Figure 23 shows the chemical diffusion coefficient dependence on the Li mol fraction x in nano-crystalline RuO₂ and the Li⁺ conductivity σ^{ion} calculated from \tilde{D} using following relations:

$$F \frac{\partial E}{\partial c_{\text{Li}}} = \frac{\partial(\mu_{\text{Li}} - \mu_{\text{Li}}^0)}{\partial c_{\text{Li}}} = \frac{\partial \mu_{\text{Li}}}{\partial c_{\text{Li}}}, \quad (8)$$

where c_{Li} is the concentration of Li in RuO₂, μ_{Li}^0 is the chemical potential of Li in pure Li that is independent of c_{Li} unlike μ_{Li} , the chemical potential of Li in RuO₂. Writing for \tilde{D} ⁹⁷

$$\tilde{D} = \frac{1}{z^2 F^2} \frac{\sigma^{\text{eon}} \sigma^{\text{ion}}}{\sigma} \frac{\partial \mu_{\text{Li}}}{\partial c_{\text{Li}}}, \quad (9)$$

with $z = 1$, σ^{eon} , σ^{ion} and σ as electronic, ionic and total conductivity, knowing, that σ^{eon} of RuO₂ is very high and comparable with σ and using Equation (8) we obtain

$$\sigma_{\text{ion}} = F \tilde{D} \left/ \frac{dE}{dc_{\text{Li}}} \right. . \quad (10)$$

dE/dc_{Li} is the slope of the coulometric titration curve plotted against Li concentration in RuO₂, found *via*

$$c_{Li} = \frac{x_{Li}}{V_{m_{Li_xRuO_2}}} \cdot \quad (11)$$

Instead of $V_{m_{Li_xRuO_2}}$, the molar volume of Li_xRuO_2 , we used molar volume of pure RuO_2 , since the concentrations of Li are very small and hence the volume expansion is negligible.

Chapter 4

Results and Discussion

4.1 Investigations on RuO₂

4.1.1 Performance of the Electrodes

Even though not the main topic of the thesis, in this subchapter we will concentrate on the influence of the morphology on the discharge behavior and capacity of RuO₂ samples in the RuO₂/LiPF₆+EC+DMC/Li cell. Moreover, the influence of the additives (C, PVDF) in association with different particle sizes and morphologies on the performance of the cell will be treated. Here we are not going into detail with the cycling or rate performance, since the cell operation is only sufficiently reversible for the first few cycles (see Fig. 24). Moreover, the XRD analysis of the electrode after 10 cycles showed that the majority of Ru is not converted into RuO₂. The reasons could be *e.g.* the low stability of the amorphous phase formed after the first cycle, irreversible side reactions with the electrolyte or mechanical detachment from the current collector. Fig. 24 illustrates the cell performance of pure crystalline RuO₂

powder (30 nm), as an example, during 10 cycles at the rate of C/20. The first cycle is highlighted by red color and is almost 100% reversible. The focus of the present work will lie on the first discharge. Note that RuO_2 is the only example so far, in which RuO_2 can be reformed *via* charging from the $\text{Ru}/\text{Li}_2\text{O}$ composite⁶⁸.

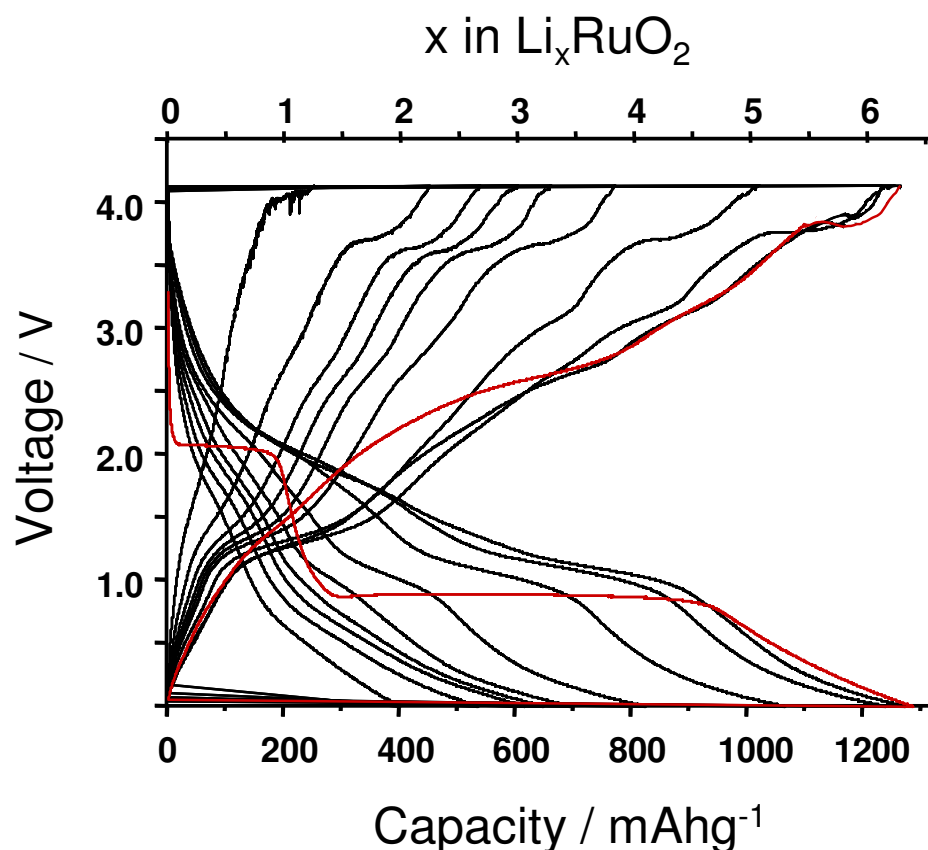


Figure 24: Cycling performance of pure crystalline RuO_2 at a rate of C/20.

In Fig. 25 the discharge behavior of RuO_2 samples with different particle sizes/modifications at a slow rate of C/20 is presented, namely: (a) 10 μm , (b) 60 nm, (c) 30 nm, (d) amorphous and (e) 3 nm. The capacity dependence on the particle size/modification is summarized in graph (f). Red colored curves correspond to the results of the electrodes with additives and the black curves are the data of pure powders. In order to minimize the error contribution, every curve represented in this figure is the average of the data of at least 3 measurements. The error bars in graph (f) are based on the variation of the experimental data, whereas the crucial source of this variation is the weight

error due to the dealing with very small amounts of samples (weight range of the samples ~ 20 mg).

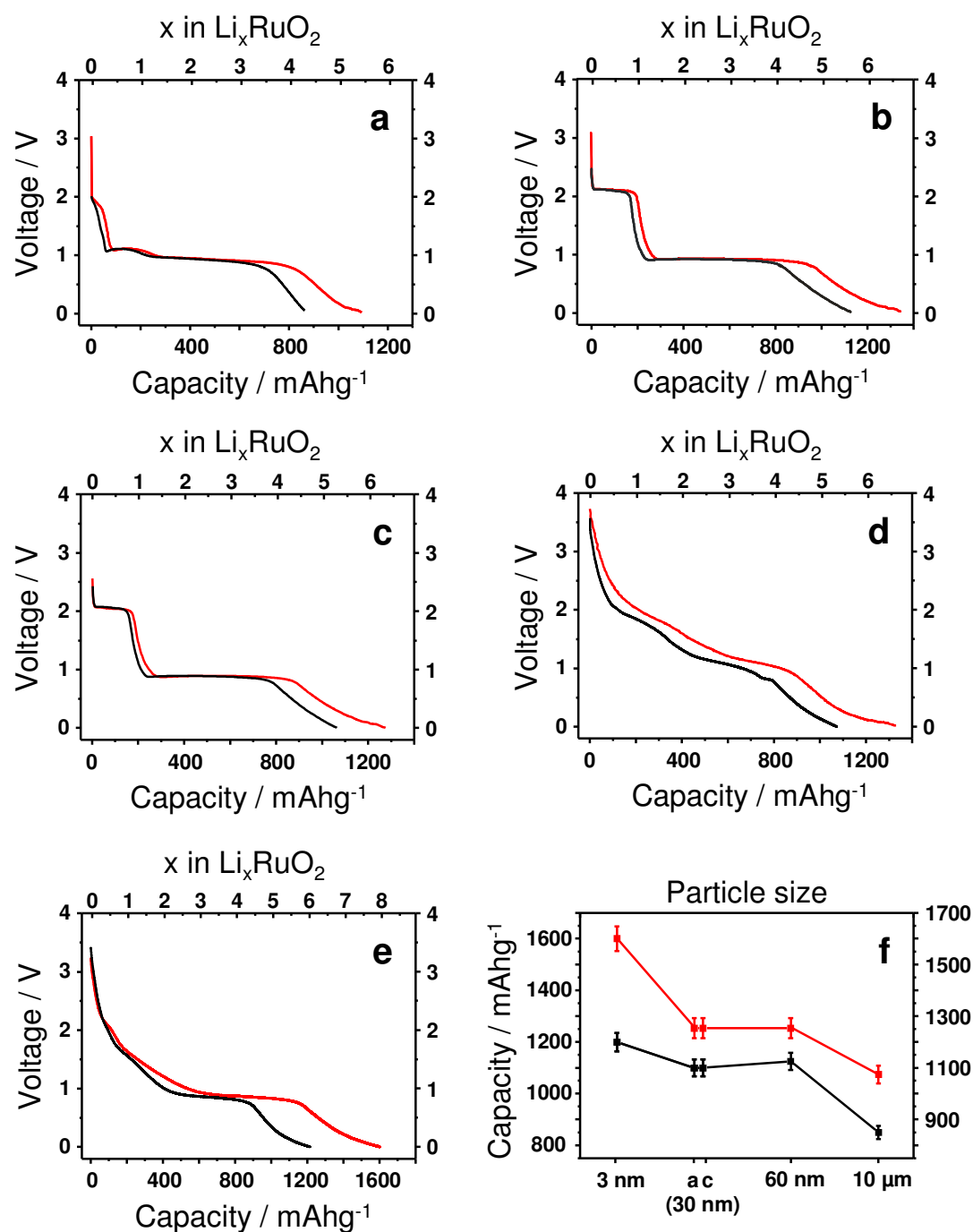


Figure 25: First discharge of RuO_2 in dependence of particle size/morphology at a rate of C/20: (a) sample (III), 10 μm ; (b) - (I), 60 nm; (c) - (II), 30 nm; (d) - (IV), amorphous; (e) - (V), 3 nm; (f) overview of capacity against the particle size. Black curves present the data of pure powders and red curves denote the data of powders with additives (PVDF, C).

Discharge Curves

Let us first consider the shape of the discharge curves. A remarkable difference in the voltage profile could be observed between micro-crystalline (a), nano-crystalline (60 nm, 30 nm) (b, c) amorphous (d) and nano-crystalline (3 nm) (e) powders. This might have different reasons.

If we compare micro-crystalline (10 μm) and nano-crystalline sample (30 nm and 60 nm exhibit the same voltage profile), shown in Fig. 26, we can see a clear voltage difference in the first plateau.

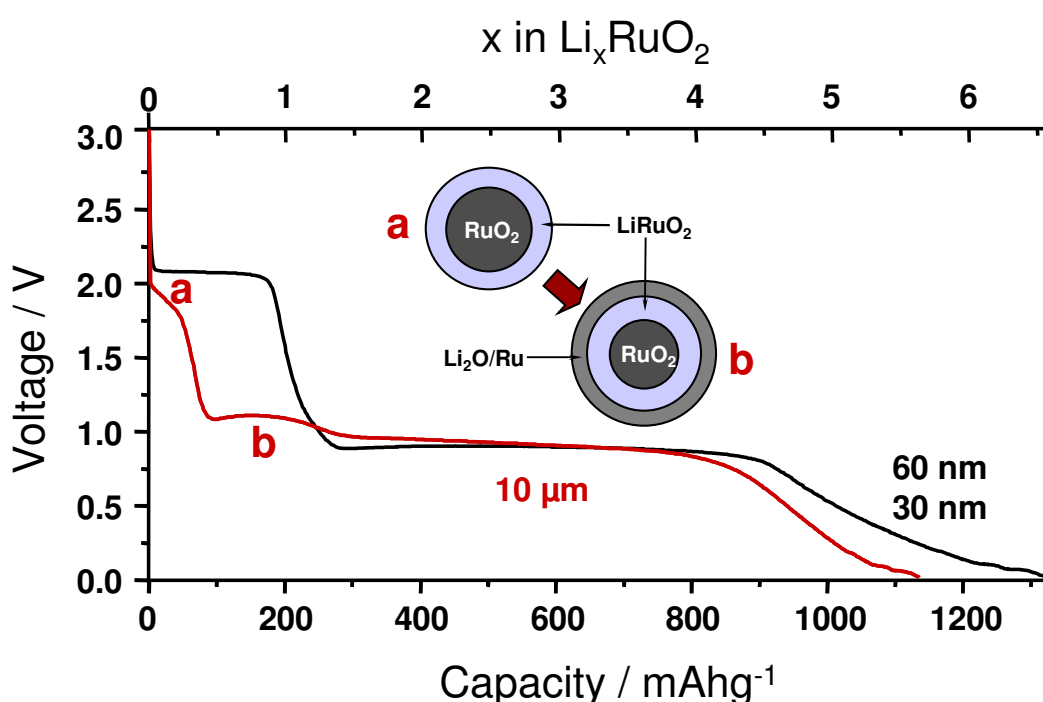


Figure 26: Comparison of the voltage profiles of the micro-crystalline (10 μm , red) and nano-crystalline sample (30 nm or 60 nm, black) at a rate of C/20; (a) and (b) denote the Li storage stages of the 10 μm sample with the corresponding schematic composition of the particles.

Due to the slow kinetics in the case of the micro-crystalline particles, upon lithiation, the decomposition reaction to $\text{Li}_2\text{O}/\text{Ru}$ already begins on the surface before LiRuO_2 formation is finished. The probable reaction mechanism is indicated in Fig. 26. Coating of the LiRuO_2 particle, which still exhibits a RuO_2 core (scheme (a), Fig. 26), with $\text{Li}_2\text{O}/\text{Ru}$ composite leads to the dropping of the non-equilibrium voltage almost to the level of the voltage value of the

decomposition reaction of LiRuO_2 to $\text{Li}_2\text{O}/\text{Ru}$ composite (scheme (b), Fig. 26). Additionally, due to the obviously enormous volume expansion during the LiRuO_2 formation, the initial particles (Fig. 27 (a)) disintegrate into pieces ((b) with the corresponding nominal composition being $\text{Li}_{0.8}\text{RuO}_2$).

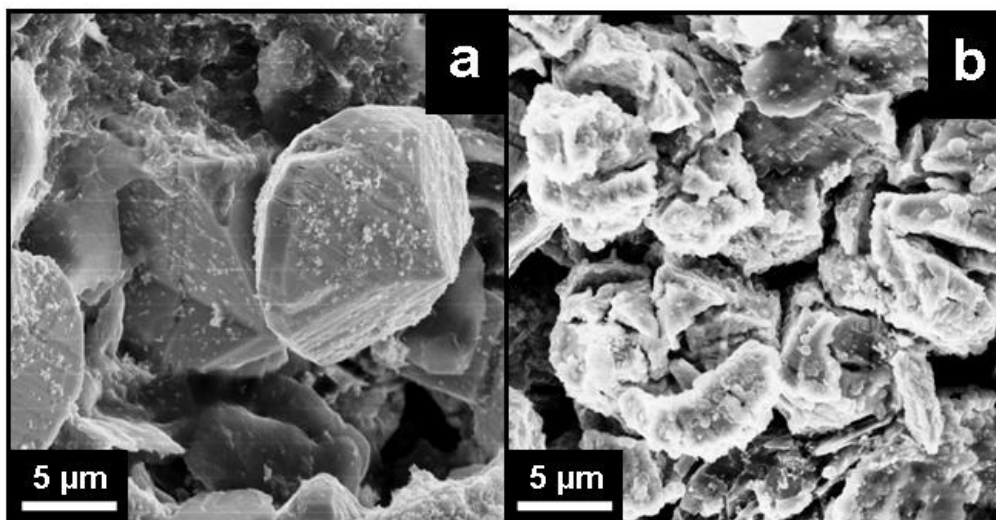


Figure 27: SEM photographs of micro sized RuO_2 particles before (a) and after reaction with 0.8Li per mol RuO_2 (b).

Here we could detect two typical nano-size effects. By reduction of the particles from $10\ \mu\text{m}$ to $60\ \text{nm}$ or $30\ \text{nm}$, the diffusion length for Li is decreased enormously, so that the transformation of the particles from Li saturated RuO_2 to LiRuO_2 and finally to $\text{Li}_2\text{O}/\text{Ru}$ composite occurs very fast and therefore, according to the discharge curve, in sequence. The accommodation of the strain caused by volume expansion during the transformation from Li saturated RuO_2 to LiRuO_2 is, in contrast to the micro sized particles, not a problem for nano-particles and because of the large free volume no cracking could be observed.

While the above discussed situation could be explained by the different kinetics, the difference in the discharge curves between nano-crystalline ($30\ \text{nm}$, $60\ \text{nm}$ (b, c)), amorphous (d) and $3\ \text{nm}$ sized (e) powders deserve a deeper insight.

The origin of the higher overall voltage could be due to the polarization effect⁹⁸ or to higher Gibbs free energy of the nano-particles and amorphous phase. To exclude the polarization term, GITT and OCV measurements were performed

(see following chapters). The sloped discharge profile of the nano-crystalline and amorphous phases can be caused by the particle size distribution and the resulting large range of free energy variation^{8,44,65}, which is possible in case of the large difference in the free energies of the pure and lithiated phases. This effect is negligible for the bigger crystallites (here 60 nm, 30 nm), owing to the low difference in the Gibbs energies of the lithiated and the pure phases.

Capacity and Influence of PVDF

Now let us look at the capacitance of the powders during the first discharge and return to Fig. 25. Capacity of the pure powders (b)-(d) seems to be in the same range. The end of the second plateau which corresponds to the full reduction of RuO₂ to Ru, *i.e.* storage of 4Li, appears exactly at the expected theoretical capacity of 806 mAhg⁻¹, followed by the interfacial extra storage⁴⁵. The lower capacity of the microcrystalline sample (a) could be explained by slow kinetics which lead to uncompleted reaction or/and isolated particles being not involved into the reaction due to the bad electronic wiring. The slightly higher capacity by ~ 0.3-0.4Li in the case of the sample (e) can be attributed to water traces including the terminating OH-groups on the surface of the nano-particles (rough composition of the powder is RuO₂ × 0.3H₂O, see chapter 3.3). These results suggest that the capacity of pure RuO₂ powders is barely influenced by the morphology or particle size when the particles are sufficiently small and the kinetics fast enough.

However, the situation is different if we consider powders mixed with additives. The red discharge curves (a)-(d) show an extension of both plateaus and so a gain in capacity of around 0.5Li in addition to the theoretical capacity ((b)-(d)) (if we again take the end of the second plateau as the reference point). By addition of carbon (graphite) to the RuO₂ powder as the only additive, this effect is not observed, which is not too surprising, since graphite is only used to improve the electronic conductivity of the electrode and electronic conductivity of RuO₂ is already very high. PVDF is beneficial for the wiring within the electrode, so that the number of the particles which are not involved into reactions should be minimized, but it still does not explain the excess storage. The excess storage of the powder with the particle size of 2-3 nm (e) is, surprisingly, above 1.5Li. The things become clearer by examination of HRTEM micrographs supported by BET analysis which shows a correlation between the surface area and the gain in the excess Li storage. The amorphous

sample exhibits the same excess capacity as the crystalline ones, because the particle size is probably increased due to the amorphisation but the surface area is supposed not to substantially exceed the value of the crystalline sample of about $130 \text{ m}^2\text{g}^{-1}$ (see Fig. 26 (a) and (b)).

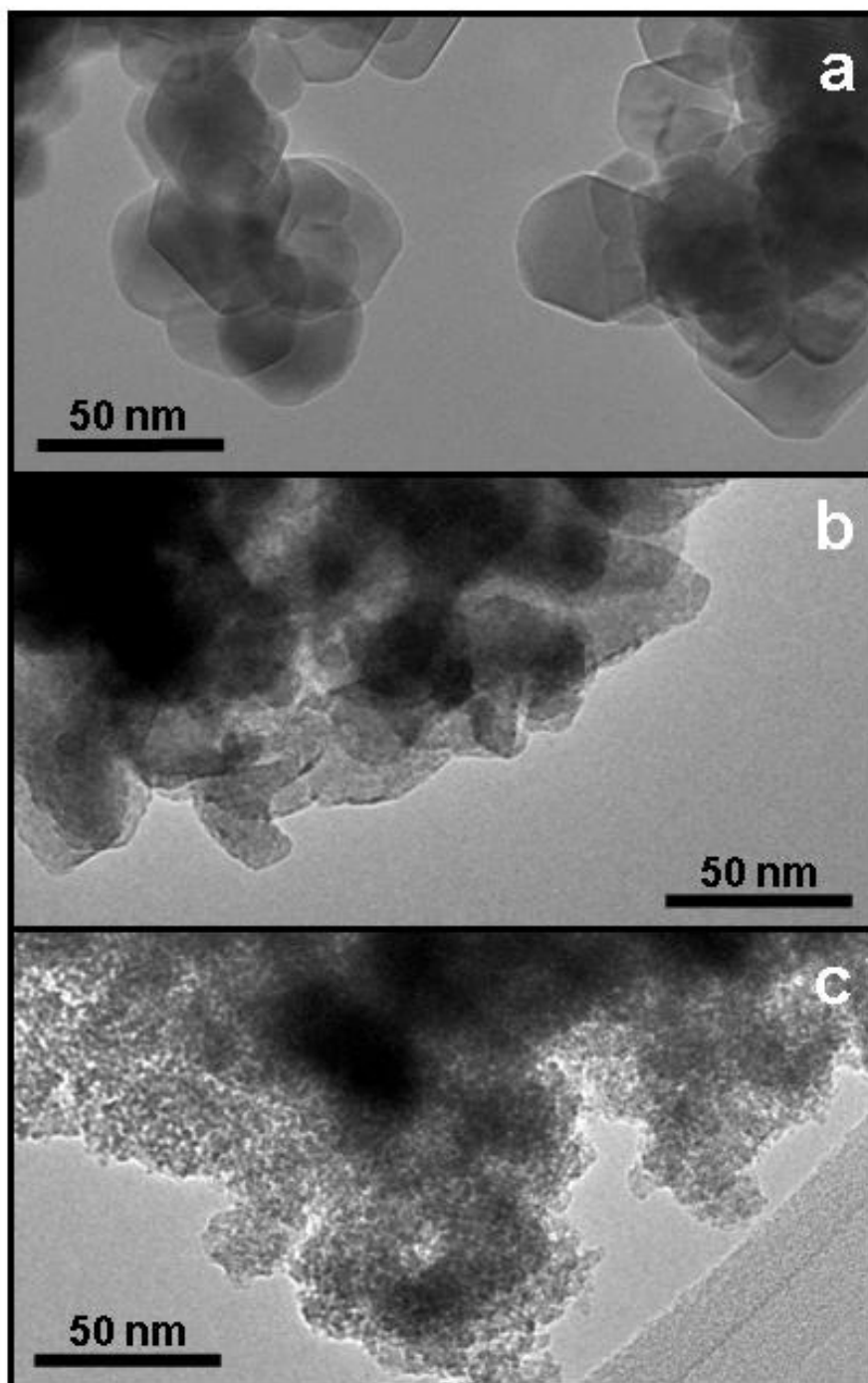


Figure 28: HRTEM micrographs of RuO_2 powders: (a) - (II), 30 nm; (b) - (IV), amorphous, which was obtained after the first cycle of 30 nm powder, and (c) - (V), 3 nm.

The Nano-crystalline sample, on the other hand, exhibits a surface area of above $350 \text{ m}^2\text{g}^{-1}$ (see Fig. 28 (c)). Since PVDF is not capable to store Li alone, but it is able to make a good contact to the surface of the particles due to its flexible long chains, this almost linear dependence of the excess storage on the surface area of the powders suggests an additional reversible (see chapter 4.1.4) storage in the particle-polymer (here PVDF)-interface.

4.1.2 Enhanced Potential of Amorphous RuO_2

In this chapter we will focus on the open-circuit voltage of the amorphous RuO_2 . We concentrate on the first two processes, namely, formation of solid solution of $x\text{Li}$ in RuO_2 (single phase regime: $x \leq 0.04$) and formation of $\text{Li}_{0.86}\text{RuO}_2$ by addition of $x\text{Li}$ (two phase regime: $0.04 \leq x \leq 0.86$). For the crystalline RuO_2 (60 nm, 30 nm) two phase coexistence is expressed as the first plateau at 2.1 V during the first discharge. In the case of amorphous RuO_2 , instead of a plateau we obtain a sloped curve (see Fig. 4) with higher overall voltage.

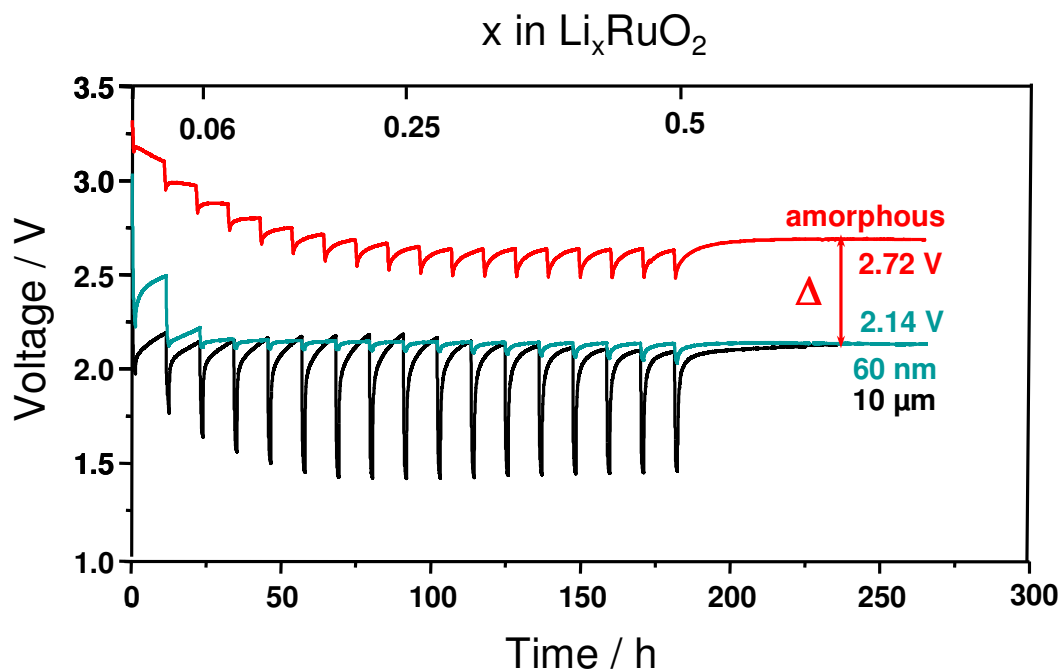


Figure 29: GITT and OCV measurements on RuO_2/Li cells with different particle sizes.

To be able to compare the OCV values of crystalline (60 nm, 10 μm) and amorphous RuO_2 , a reference amount of 0.5Li was titrated into the electrodes *via* GITT and afterwards the system could equilibrate for more than one week (see Fig. 29; note that here powders with additives were used).

As a result we surprisingly obtained a plateau in the case of the amorphous sample with a remarkable different OCV value compared to the crystalline materials, whereas OCV potentials of crystalline samples are, as expected due to the low surface contribution that scales with $1/r$, the same⁶³. Table 1 summarizes the OCV potentials and the corresponding Gibbs energy values ($\Delta_r G = -zF(\text{OCV})$, $z = 1$: number of transferred electrons needed to form LiRuO_2 , F : Faraday's constant) for the four samples under consideration.

Size	OCV / V	$\Delta_r G$ / kJmol^{-1}
amorphous	2.72	-262.4
60 nm, 10 μm	2.14	-206.5
Δ	0.58	-55.9

Table 1: Comparison of the open-circuit voltage (OCV) and the corresponding Gibbs energy for the Li incorporation reaction ($\Delta_r G$) in 60 nm, 10 μm and amorphous RuO_2 .

The 60 nm and 10 μm electrodes have similar OCVs and Gibbs free energies of Li incorporation. If we would use $\bar{\gamma} \approx 0.1 \text{ Jm}^{-2}$ and $V_m(\text{RuO}_2) = 19.09 \text{ cm}^3 \text{ mol}^{-1}$, the surface contribution $2V_m \bar{\gamma} / \bar{r}$ for 60 nm particle size is expected to yield less than 1 mV ($\sim -0.1 \text{ kJmol}^{-1}$). On the other hand, the excess contribution of 580 mV in the case of the amorphous sample would demand a grain size of $\sim 1.4 \text{ \AA}$, if explained by particle size effect.

However, it makes sense in a quantitative way if we consider the amorphous state as a limit case of the nano-crystalline state (see Fig. 30). In nano-crystalline materials the grains are connected through grain boundaries. In these grain boundaries atoms reside that have no long range order. If the grain size would be reduced to the atomic distances, the resulting material would, as it were, consist of grain boundary regions and therewith all the long range order would be lost⁶⁴.

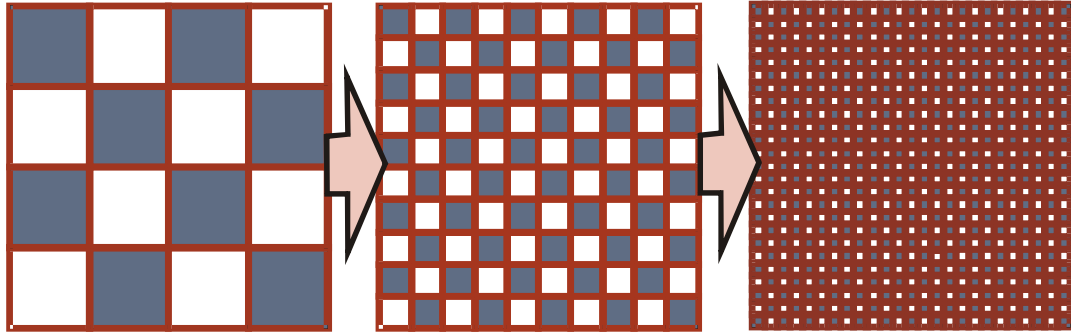


Figure 30: Thought experiment that connects the limit of a nano-crystalline material (with size approaching zero) to the amorphous state. The latter is characterized by a total loss of orientation (white and grey squares denote the differently orientated grains).

More reliably, the lost long range order can be attributed to a “molten” state. The excess voltage of 580 mV can be seen as the free enthalpy of the transition from the crystalline to amorphous (“molten”) state at the operating temperature and should be of the order of magnitude of the free melting enthalpy ($\Delta G_{RuO_2}^m$). Let us consider this in detail. The free enthalpy of the reaction $0.82Li + Li_{0.04}RuO_2 \rightleftharpoons Li_{0.86}RuO_2$ for crystalline phases can be expressed in terms of free Gibbs formation energies, as follows:

$$\Delta_r G^c = \Delta_f G_{Li_{0.86}RuO_2}^c - \Delta_f G_{RuO_2(ss)}^c \quad (12)$$

For the case, when the initial RuO_2 is amorphous, while the lithiation product $Li_{0.86}RuO_2$ is (at least predominantly) crystalline, (see Fig. 5) the measured value $\Delta_r G$ has to be corrected. Neglecting capillary pressure effects here (*i.e.* we can now formally refer to $\bar{r} \approx \infty$) and writing δG for the excess free enthalpy of formation from the elements $\Delta_f G^a - \Delta_f G^c$ we may write

$$\Delta_r G = \Delta_r G^c + \delta G_{RuO_2} \quad (13)$$

Since in the amorphous state the long range order is absent, we can identify the magnitude of δG_{RuO_2} directly with the melting free enthalpy at the operation temperature. If we ignore the temperature dependence of the melting free enthalpy at this point, *i.e.* neglect the entropy effects, this would mean that

$$\delta G_{RuO_2} \approx \delta G^{(1)} \equiv \left| \Delta H_{RuO_2}^m \right|. \quad (14)$$

The lower T compared to T_m , the better is this approximation. A more precise approach ($\delta G^{(2)}$) includes $\Delta S_{RuO_2}^m$ but assumes the temperature independency of $\Delta S_{RuO_2}^m$ and $\Delta H_{RuO_2}^m$. Using $\Delta G^m(T_m) = 0$ we can write instead of eqn (14)

$$\delta G_{RuO_2} \approx \delta G^{(2)} \equiv \left(1 - \frac{T}{T_m} \right) \Delta H^m(T_m). \quad (15)$$

The melting point of RuO_2 is not known, since it sublimates at 1200 °C. If we take the isostructural TiO_2 as an example, the melting point here is 1850 °C and hence the absolute value of the second order correction ($(\delta G^{(2)} - \delta G^{(1)}) / \delta G^{(1)}$) would be less than 15%. As the melting enthalpy of RuO_2 is not available, we use ΔH^m of the isostructural TiO_2 and VO_2 being 65 kJmol⁻¹ and 57 kJmol⁻¹, respectively, as a reference⁹⁹. Obviously, a value of *ca.* 60 kJmol⁻¹ is in a very good agreement with the excess free enthalpy of 55.9 kJmol⁻¹ found in this investigation for the amorphous RuO_2 . The match is even better if we consider the second approximation (see Table 2), yet we consider this as coincidental.

Rutile	$\Delta H^m / \text{kJmol}^{-1}$	$\delta G^{(2)} / \text{kJmol}^{-1}$
TiO_2	65 ⁹⁹	56
VO_2	57 ⁹⁹	49

Table 2: Melting enthalpy ΔH^m and calculated free melting enthalpy $\Delta G^{(2)}$ of TiO_2 and VO_2 for room temperature.

The above discussion is semi-qualitative and is not exact, as it is not based on an analysis of the chemical potentials of lithium, nor does it consider varied concentrations of coexistence. The next part of this chapter provides a detailed thermodynamic analysis of the single and compositionally non-variant two phase regime, which are present before and during $LiRuO_2$ formation by lithiation, respectively. The chemical potentials of Li are examined in crystalline (stable) and amorphous (metastable) RuO_2 , in single and two phase regimes.

Thermodynamic Analysis (Chemical Potentials of Li)⁶⁴

Let us first investigate the chemical potential in the two-phase regime of $\text{Li}_\varepsilon\text{Y}$ (metastable or stable): Li_ηY (stable). In our case it is the two-phase regime of RuO_2 (Li saturated) and LiRuO_2 (RuO_2 saturated), with $Y = \text{RuO}_2$, $\varepsilon \approx 0$ and $\eta \approx 1$. Since the RuO_2 part stays constant (*i.e.* invariant Ru/O ratio), the situation can be regarded as pseudo binary which is adequate for our analysis.

The emf is given by the reaction



that can be rewritten as



The latter form points out that the voltage we measure in the electrochemical cell is governed by the difference in the Li potential in the reference phase and in the two phase system



Our experiments above (Fig. 29) showed that an increase of the Gibbs energy of RuO_2 by amorphisation obviously now decreases the chemical potential of lithium, leading to an increased difference of the chemical potentials between Li in Li-metal and Li in the two phase system and hence to an increased cell voltage. This interesting impact of the Gibbs energy of the phase (here RuO_2) on the chemical potential of the respective component (here Li) will be the main subject of the discussion below. For convenience reasons we will use the following notion throughout the subsequent thermodynamic analysis: We denote the Li-poor phase “ α ” and the Li-rich phase “ β ”. The corresponding coexistence compositions are $\text{Li}_\varepsilon\text{Y}$ for α and Li_ηY for β . The general formula will be Li_ξY (*i.e.* the nominal composition). The corresponding mole fractions of Li, indicated by a , b and x , are interrelated with ε , η and ξ via:

$$x = \xi/(1+\xi) \quad (19)$$

$$a = \varepsilon/(1+\varepsilon) \quad (20)$$

$$b = \eta/(1+\eta) \quad (21)$$

In the following two approaches are presented. The first approach is only valid for the non-variant situation (Appendix 1), while the second approach is applicable to the both, single- and two-phase regime. Both approaches are based on the same concept: they rely on phase equilibrium conditions and Gibbs-Duhem equation. We are going to analyze the cell $Li_\varepsilon Y, Li_\eta Y / Li^+ - \text{electrolyte} / Li$, where Y stands for RuO_2 (metastable or stable), so that we consider the cell RuO_2 (metastable or stable), $LiRuO_2$ (stable) / Li^+ -electrolyte / Li . The coexistence compositions at room temperature in the case of the stable phases are $\varepsilon \approx 0.04$ and $\eta \approx 0.84$.

Approach 1: Application of cell reaction formalism

Since Li^+ -electrolyte does not exhibit gradients in the electrochemical potential of Li^+ ($\tilde{\mu}_{Li^+}$) and it is not electronically conductive (*i.e.* $\nabla \mu_{Li}$ is governed by the gradient in the electrochemical potentials of the electrons), we can determine the equilibrium cell voltage E which is proportional to the difference in the electrochemical potential of the electrons through Nernst's equation

$$E = -(\mu_{Li} - \mu_{Li}^0)/F. \quad (22)$$

(μ_{Li}^0 is the chemical potential of Li in bulk Li , F is Faraday's constant).

The Li potential in $Li_\varepsilon Y$ can be found as following:

$$\mu_{Li} = \frac{1}{\varepsilon} \mu_{Li_\varepsilon Y} - \frac{1}{\varepsilon} \mu_Y. \quad (23)$$

The unknown μ_Y is determined by

$$\mu_Y = \mu_{Li_\eta Y} - \eta \mu_{Li} \quad (24)$$

leading to

$$\mu_{Li} = \frac{1}{\varepsilon - \eta} \left[\mu_{Li_\varepsilon Y} - \mu_{Li_\eta Y} \right] \quad (25)$$

and therefore

$$\begin{aligned} -EF &= \frac{1}{\eta - \varepsilon} \left[-\mu_{Li_\varepsilon Y} + \mu_{Li_\eta Y} - (\eta - \varepsilon)\mu_{Li}^0 \right] \\ &= \frac{1}{\eta - \varepsilon} \Delta_R G \{ (\eta - \varepsilon)Li + Li_\varepsilon Y \rightarrow Li_\eta Y \}. \end{aligned} \quad (26)$$

The last expression is the cell voltage which is given in the usual way involving the Gibbs energy of the cell reaction. It is significant that we assumed for the above treatment

$$\mu_Y(Li_\varepsilon Y) = \mu_Y(Li_\eta Y) \quad (27)$$

together with

$$\mu_{Li}(Li_\varepsilon Y) = \mu_{Li}(Li_\eta Y), \quad (28)$$

even in the case of the metastable framework Y . This is the consequence of the Gibbs-Duhem equation

$$n_{Li} d\mu_{Li} + n_Y d\mu_Y = 0 \quad (29)$$

which supposes that G of each phase is a homogeneous function of the first degree in the mole numbers n_{Li} and n_Y . If this equation is true for both $Li_\varepsilon Y$ and $Li_\eta Y$ and if exchange equilibrium for Li between the two phases is ensured, it holds that $d\mu_{Li} = 0$ and automatically implies $d\mu_Y = 0$. This means that mobility of only one component (here Li) is sufficient for achieving the full phase equilibrium which is true for a binary or a pseudo-binary compound.

Writing the analogous expression for the metastable phase (denoted by dash) as eqn (23) and forming the difference ($E^{ex} = E' - E$), we obtain the excess quantities $\delta E \equiv E^{ex}$ and $\delta\mu_{Li} \equiv \mu_{Li}^{ex}(Li_\varepsilon Y)$ which are correlated through

$$-\delta EF = \frac{1}{\eta - \varepsilon} \delta \mu_{Li}. \quad (30)$$

Please note that δE can be here directly identified with the cell voltage of the quasi-symmetrical cell, with stable RuO_2 being one electrode and metastable RuO_2 the other.

Approach 2: Application of mixture thermodynamics

Since approach 1 is suitable only for the non-variant case, we are going to analyze the emf E by a more general approach which allows us the consideration of the emf of the univariant cell $\text{Li}_{\xi}\text{Y}/\text{Li}^+$ -electrolyte/Li for $\xi < a$ (a is the solubility limit; for $\xi > a$ we have the two phase situation). As a first step we have to correlate μ_{Li}^{α} in the phase α with the molar Gibbs energy of the phase α . The Gibbs energy of the phase α is given by

$$G_{\alpha} \equiv G_{\alpha}^{\text{total}} / (n_{Li}^{\alpha} + n_Y^{\alpha}), \quad (31)$$

where

$$G_{\alpha}^{\text{total}} \equiv n_{Li}^{\alpha} \mu_{Li}^{\alpha} + n_Y^{\alpha} \mu_Y^{\alpha}. \quad (32)$$

According to the definition, the chemical potential of the phase μ_{α} is

$$\mu_{\alpha} = G_{\alpha}^{\text{total}} / n^{\alpha} = (1 + \varepsilon) G_{\alpha}. \quad (33)$$

The difference between μ_{α} and G_{α} (see eqn (31)) is the ratio $(n_{Li} + n_Y)/n_{\alpha}$, which for $\alpha \equiv \text{Li}_{\xi}\text{Y}$ is $\varepsilon + 1$ since $n_{Li} = \varepsilon n_{\text{Li}_{\xi}\text{Y}}$ and $n_Y = n_{\text{Li}_{\xi}\text{Y}}$.

According to mixture thermodynamics^{100,101}, the chemical potential of Li in the phase α at the lithium mole fraction x is related to the Gibbs energy of the phase α $G_{\alpha} = G_{\text{Li}_{\xi}\text{Y}}$ through

$$\mu_{Li} = G_{\text{Li}_{\xi}\text{Y}} + (1 - x) \frac{dG_{\text{Li}_{\xi}\text{Y}}}{dx}. \quad (34)$$

Additionally to the contribution of $G_\alpha(x)$, the second term in this relation describes the slope of the tangent to $G_\alpha(x)$ at the mole fraction x which is particularly important for small x values (see Fig. 31). The Li potential in the case of two-phase equilibrium is determined by the coexistence of $\alpha \equiv Li_\epsilon Y$ with $\beta \equiv Li_\eta Y$. Graphically, a and b can be easily estimated by the common tangent method applied to the $G(x) - x$ plane (see Fig. 31). Hence the slope of this double tangent is given by

$$\left. \frac{dG}{dx} \right|_a = \frac{G_{Li_\eta Y} - G_{Li_\epsilon Y}}{b - a} = \frac{G_\beta(b) - G_\alpha(a)}{b - a}. \quad (35)$$

Since the chemical potential in the two-phase regime is the same as the value for chemical potential of α at $x = a$, combining eqn (34) and (35) we obtain for the two phase regime

$$\mu_{Li}(a \leq x \leq b) = G_\alpha(a) + \frac{1-a}{b-a} [G_\beta(b) - G_\alpha(a)]. \quad (36)$$

In our case, with $a \ll b < 1$, it leads to

$$\begin{aligned} \mu_{Li}(a \leq x \leq b) &= G_\alpha(a) + \frac{1}{b} [G_\beta(b) - G_\alpha(a)] \\ &= \frac{b-1}{b} G_\alpha(a) + \frac{1}{b} G_\beta(b). \end{aligned} \quad (37)$$

Again, writing down the analogous equation for the metastable phase and forming the difference, we receive the excess quantity

$$\delta\mu_{Li} = \frac{b-1}{b} \delta G, \quad (38)$$

where $\delta G \equiv G_{\alpha'} - G_\alpha$.

Since $Li_\eta Y = Li_{0.86} Y$, it can be approximated by $Li_1 Y = LiRuO_2$ resulting $b = 1/2$ and

$$-\delta\mu_{Li} = \delta G. \quad (39)$$

In consistence with the experiments, the obtained signs for the excess quantities of G and μ_{Li} are opposite. We find the same result if we apply $\varepsilon = 0$ and $\eta = 1$ to the excess values derived from eqn (25) or eqn (26) in approach 1.

This fact is not only valid for this special case; eqn (36) becomes even fully identical with eqn (25) by exchanging the stoichiometric numbers ε , η by mole fractions a , b and using eqn (33). The graphical analysis in Fig. 31 shows that μ_{Li} in α' is indeed decreased compared to α . Please note that this analysis is based on eqn (34) which yields μ_{Li} as intercept of the tangent at $x = 1$. The fundamental assumption in the graphical analysis is the shape invariance, *i.e.* $\delta G(x) = \Delta$ with $d\Delta/dx = 0$, which means that the curves G_α and $G_{\alpha'}$ are identical and $G_{\alpha'}$ is only shifted to the higher G values (Fig. 32). Although the shape invariance is quite an approximation, it is still on the same level as typical explanations for the excess energy term (see below) and it is beneficial in terms of distinction from other influences.

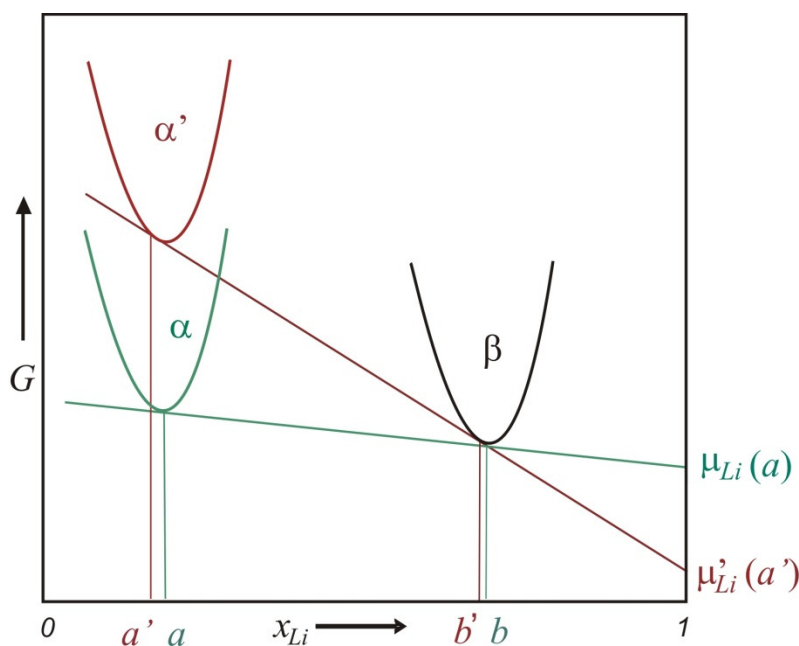


Figure 31: Molar Gibbs energy in the system Li-Y as a function of Li content. Coexistence of the stable phase α with the stable phase β compared with the coexistence of the metastable phase α' with the stable phase β . The respective double tangent construction yields the coexistence compositions (ε, η) as well as the corresponding chemical potentials.

Comparing the two above approaches, it is very interesting to observe that they both yielded a negative $\delta\mu$ in the two-phase-region, particularly with regard to the role of the coexistence composition. The clear consequence of the steeper gradient for $\alpha':\beta$ compared to $\alpha:\beta$, which is caused by the fact that Li introduction into the phase of higher free energy α' has a higher tendency to form the same product β , is the lowered chemical potential of Li. Approach 2 shows that the two-phase equilibrium strongly depends on the slope of the double tangents and the slope is given by the different coexistence concentrations, whereby small differences between a' and a cause enormous variations of the slope. Approach 1 would have resulted the same, even if we would have ignored the variations in the compositions (*e.g.* by setting $\varepsilon=0$ and $\eta=1$), because coexistence of phases is a requirement for applying of approach 1 and this then simply means different slopes and second order variations of composition.

Comparison with cell voltage in univariant systems

Here we will focus on mixture thermodynamics and again use the assumption of shape invariance ($d\Delta/dx = 0$).

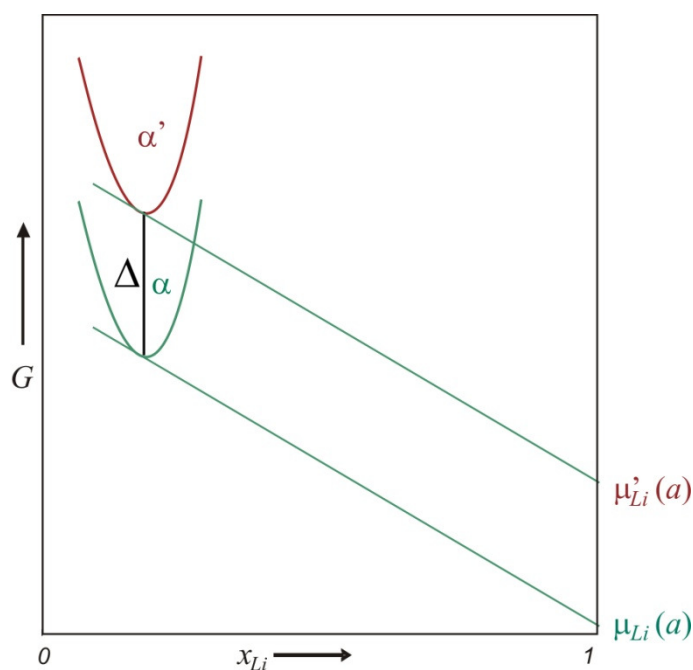


Figure 32: If the $G(x)$ curve is shifted toward higher values in the case of the metastable compound and the chemical potential of Li is increased by the same difference Δ .

Fig. 32 presents two phases with different Gibbs energies in the single phase regime ($x < a'$). We can observe that here μ_{Li} is clearly higher in phase α' than in α as long as shape invariance of $G(x)$ holds. In this case, for a given x it is valid that $\delta\mu_{Li} = \Delta > 0$ and therefore we obtain a smaller voltage, *i.e.* the value for δE is negative, in striking contrast to the two phase regime. According to Fig. 31, for $a' < x < a$ we already reside in the two phase regime for the combination $\alpha':\beta$, but we are still in the single phase regime for the combination $\alpha:\beta$. Fig. 33 illustrates the change of chemical potential with increasing x : the chemical potentials approach and become identical at $x = a^*$; between a' and a^* $\delta\mu_{Li} > 0$, but is no longer constant; for $a^* < x < a$ $\delta\mu_{Li}$ is negative and increases until the constant value $\Theta \equiv \mu'_{Li}(a') - \mu_{Li}(a)$ is reached for $a < x < b'$.

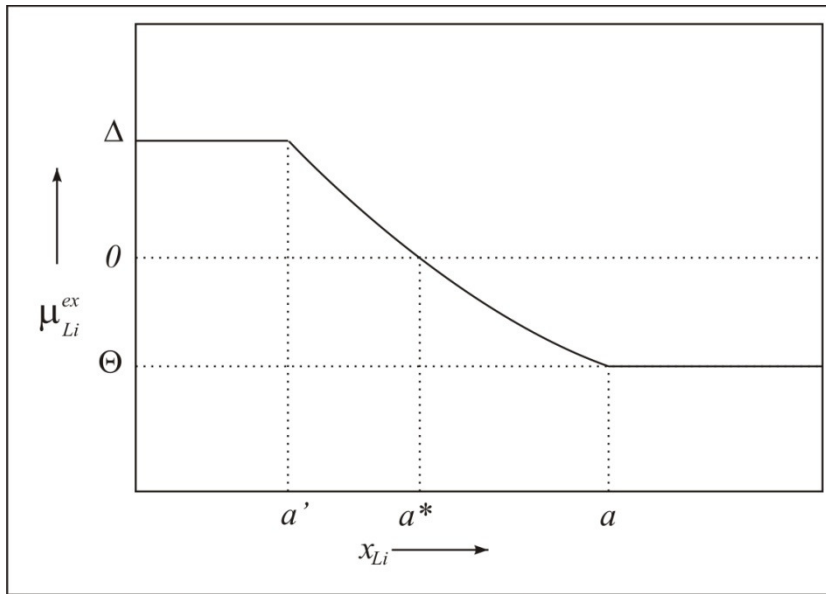


Figure 33: Variation of the excess chemical potential of Li from the region where we meet single phase behavior for both α and α' ($x < a'$) through a regime where we have two phase behavior for α' but not for α ($a' < x < a$) to a fully two phase situation. If the Li-rich phase would be the metastable one, μ_{Li}^{ex} would increase from Δ to $\Delta + |\Theta|$. (Note the non-differentiability at a' and a ; the form of the curve was calculated using parabolic $G(x)$ functions).

The composition a^* , at which the inversion from positive excess μ_{Li} to the negative value should occur, can be easily obtained graphically (see Fig. 34). In

the case of $x > a'$ (also for a^*), μ'_{Li} is constant and equal to $\mu'_{Li}(a')$. For a^* the phase α is still in the single phase regime, so the composition a^* (where $\delta\mu_{Li} = 0$ (compare Fig. 33)) is identical to the composition at which the double tangent to α' and β yields $\mu'_{Li}(a')$ at the intercept $x = 1$.

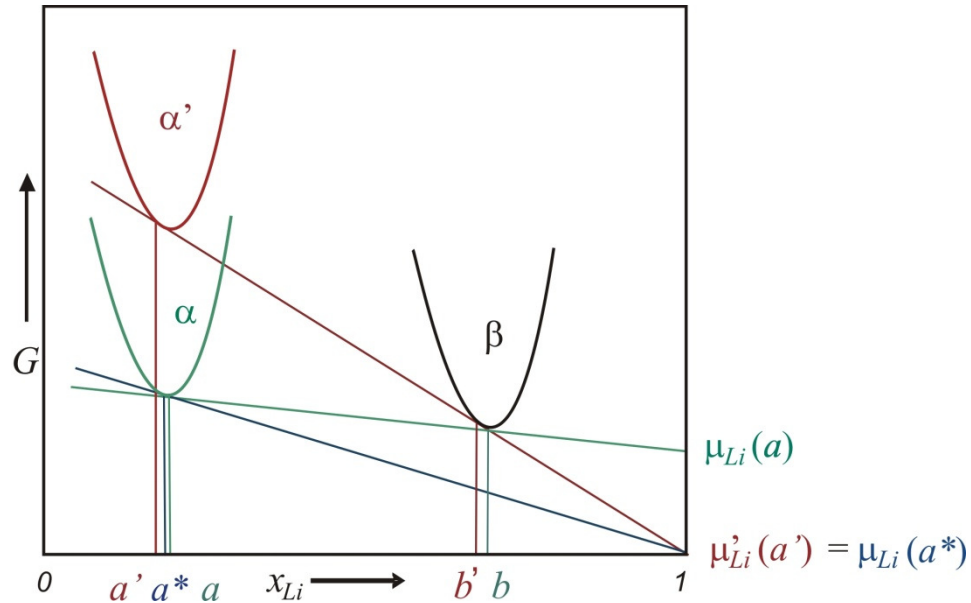


Figure 34: Determination of the cross-over composition a^* . At $a^* \mu'_{Li} - \mu_{Li} = 0$.

At this point, let us consider the limit cases of the excess chemical potential of Li with the help of eqn (36). When $a \rightarrow b$, the chemical potential and so the cell voltage (excess voltage: Θ/F) obviously diverge, *i.e.* the coexistence compositions approach each other. If we consider stable systems, closely neighbored phases in the phase diagram, in the same system, exhibit similar bonding conditions and so very different G -values of the phases are rather unlikely. In the case of the metastable phases this might be different, since different mechanisms are responsible for the formation of a metastable phase and for a transition from α to β . Still, it is quite improbable that the voltage can be exceedingly high, since closely neighbored phases usually have overlapping $G(x)$ curves. On the other hand, when $b \rightarrow 1$, Θ moves toward zero. This simply means that μ_{Li} approaches the value μ_{Li}^0 of metallic Li which obviously leads to $E \rightarrow 0$.

Experimental verification

Besides the good quantitative agreement with the emf results, there are further experimental evidences for the validity of this approach. Figure 35 presents apparent Li^+ -conductivities of the crystalline and amorphous sample in dependence of Li content. Li^+ -conductivities were calculated from the Li diffusion coefficient according to eqn (10). The unreasonable decrease of Li^+ -conductivity with increasing x_{Li} in Fig. 35 indicates that in this region a two-phase system occurs for which eqn (10) fails. So we take the maximum as coexistence composition. The maxima sensitively indicate the transition from single to two phase regime (see chapter 4.1.3 for more details). Obviously the here obtained a' and a compositions are consistent with the discussion above and Fig. 33 which suggested a smaller solubility limit of Li in amorphous than in the crystalline RuO_2 and hence smaller a' value compared to a .

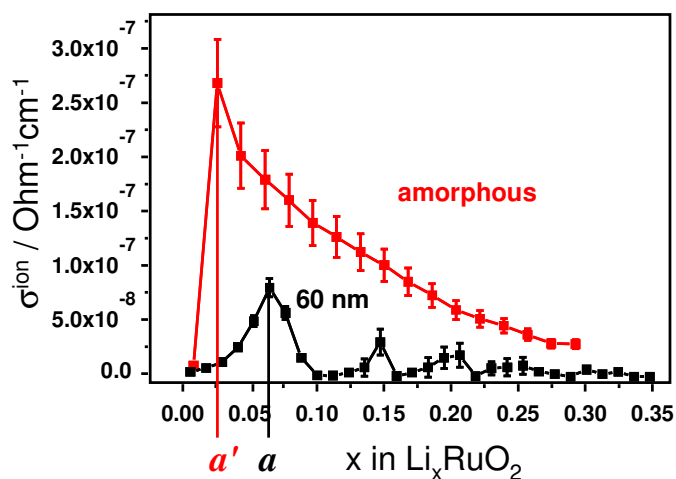


Figure 35: Apparent ionic conductivity deduced from the Li-diffusion coefficient, which is obtained from the galvanostatic titration of RuO_2 with Li. As the Li^+ conductivity is supposed to increase with x in the x -range considered, the decreasing values are attributed to apparent effective values in the two-phase regime.

Since, typically, a real system is much more complicated than a model, we could however not observe the expected inversion of the voltage for very small x -values at the composition a^* (see Fig. 36), but we clearly see both curves approaching with decreasing x . The reasons, why the experiments did not show an inversion of the voltage even for small x , might be following: First, the

minimum of the $G(x)$ curve of RuO_2 , being a boundary phase in the system RuO_2/Li , may be close to $x = 0$, resulting very small solubility limits and hence the value a^* may be very close to zero as well. Second, the shape invariance does not hold and the slope of the $G(x)$ curve of the amorphous RuO_2 at very small x values could be steeper than the $G(x)$ curve of the crystalline RuO_2 . This would mean a small chemical potential for Li and so, small amounts of Li, according to the steeper slope, could easily stabilize the amorphous phase.

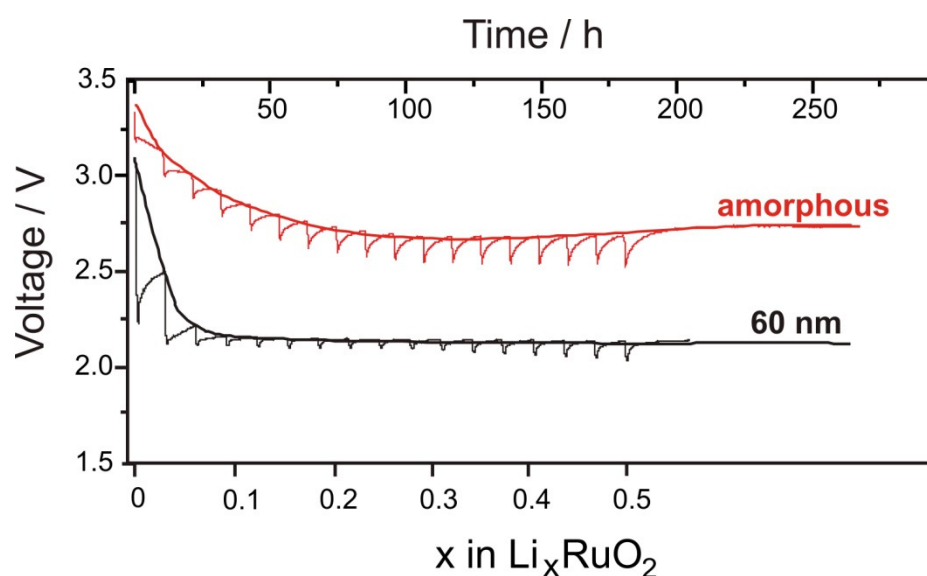


Figure 36: Galvanostatic titration curves in the system $\text{RuO}_2 - \text{LiRuO}_2$ for amorphous and (almost) macroscopically crystalline RuO_2 . The voltage refers to the potential vs. Li-electrode. As capillary effects at 60 nm are negligible, the black curve corresponds to the thermodynamically stable situation.

4.1.3 Li-Diffusion Coefficient and Li⁺-Conductivity

In contrast to the previous chapter which was dedicated to the thermodynamics of the Li - RuO₂/LiRuO₂ system, this chapter treats the kinetics. Li⁺-conductivity can be calculated from the diffusion coefficient of Li that is obtained from the GITT measurements, as it is explained in detail in the chapter 3.6. Every curve presented here is a selected data corresponding to the average of basically three measurements and the error bars give the range of variation in the measured data. As surface area of the sample, which is required for the calculation of the diffusion coefficient, geometrical area value was taken. This is a sufficient approximation for estimation of the current density which is relevant for the diffusion. Here, again, not only the influence of the particle size and modification is considered, but also the influence of additives (PVDF) on the kinetics is taken into account.

Amorphous Powders

Fig. 37 shows results of amorphous powders obtained from crystalline powders with the average particle size of 60 nm (a, b) and 30 nm (c, d) by discharge and charge in the first cycle. The Li⁺-conductivities in (a) and (c) exhibit a clear maximum in a very low Li-content range of $0 < x < 0.03$, *i.e.* the maximum is somewhere between the two first measurement points, since the experimental resolution is not high enough to name the exact values.

In this small concentration range, addition of Li into RuO₂ sample should increase the Li⁺-conductivity in RuO₂. Here we observe a maximum followed by a decreasing apparent Li⁺-conductivity. The used calculation of the diffusion coefficient and Li⁺-conductivity is valid only for single phase regimes. The unreasonable decrease in Li⁺-conductivity must hence be due to the two-phase regime; thus, the apparent Li⁺-conductivity can be used as a very sensitive indicator for the transition from the single into the two phase regime, *i.e.* the solubility limit of Li in RuO₂ can be easily determined this way. (The validity of this technique is tested versus emf measurements for crystalline samples, see below.)

The additives (PVDF, C) do not seem to influence the kinetics, at least the values under consideration (single-phase); the variation of the data is in the error limits.

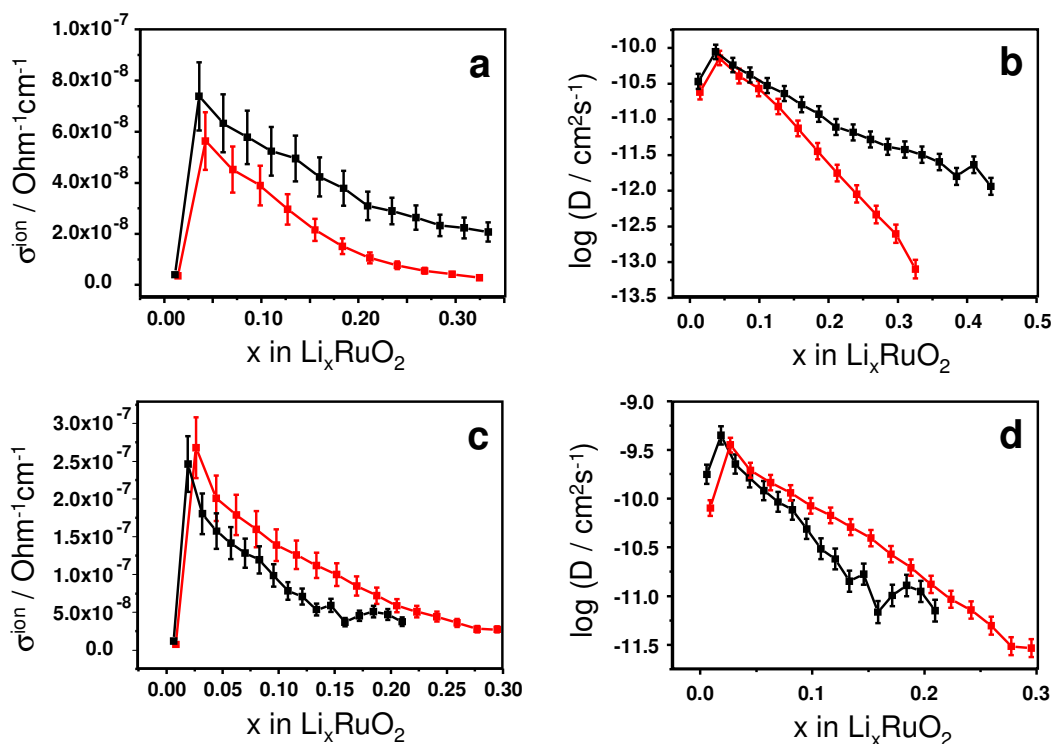


Figure 37: Li^+ -conductivity and Li-diffusion coefficient of amorphous RuO_2 electrodes: (a, b) obtained from 60 nm and (c, d) from 30 nm crystalline powders. Data denoted in black are results of the pure powders and in red are results of electrodes containing PVDF.

In Fig. 38 a closer comparison of Li^+ -conductivities and Li-diffusion coefficients in amorphous powders with different particle sizes is given. In Fig. 28, chapter 4.1.1 we saw that the grain size after amorphisation can be increased, but the size ratio between the amorphous particles obtained from the 30 nm and 60 nm sized crystalline powders is expected to be approximately the same.

The apparent shifts of the maxima (see Fig. 38) with respect to the composition are only due to the different experimental resolutions of the Li-content and are not worth to be taken into account. Li^+ -conductivity and Li-diffusion coefficient are for amorphous RuO_2 with smaller particle size (blue curve Fig. 38) about one order of magnitude higher than for amorphous RuO_2 with bigger particle size (black curve). This discrepancy is not due to the different structure of the particles, it is rather due to the evaluation itself. We derived D from the short time solution of the diffusion equation. The cross-check by estimating the mean square displacement according to $(\Delta l)^2 = 2Dt$ (with D Diffusion coefficient and t time of the short time brunch of the polarization experiment)

yields values that are about 1-1.5 orders of magnitude higher than the particle size. From the validity of the linear ΔE vs. $\Delta\sqrt{t}$ law (see Fig. 22) it must be concluded that we have to refer to a bigger “pseudo-particle” formed by agglomeration. The role of the grain boundaries then included in the evaluation can be positive or negative. In our case it seems that they act as fast pathways.

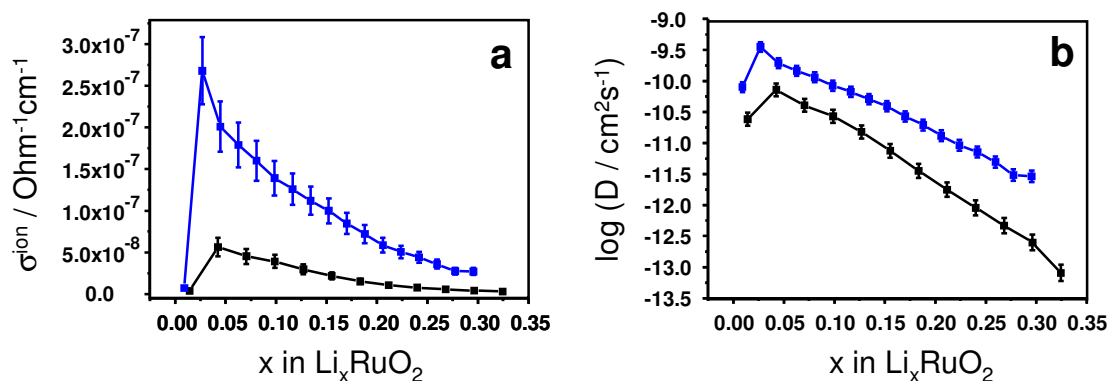


Figure 38: Comparison of amorphous samples obtained from 30 nm (blue) and 60 nm (black) sized crystalline powders.

Crystalline Powders

Now let us consider the corresponding Li^+ -conductivities and Li-diffusion coefficients of 60 nm (a) and 30 nm (b) sized crystalline samples displayed in Fig. 39. Both pure powders exhibit a clear maximum in the apparent Li^+ -conductivity which is again attributed to the solubility limit of Li in RuO_2 . The maxima are placed in the range of $0.05 < x < 0.06$ Li per RuO_2 and are close to the value of 0.04Li obtained from the discharge curves of the crystalline powders. The advantage of this method is that the solubility limit can be found in nano-crystalline or amorphous species, whereas it is not possible to estimate it from their sloped discharge curves. Depending on the experimental resolution, *i.e.* the amount of Li inserted per GITT step, the determination of the solubility limit can be very exact. The strong value variations after the first pretty accurate peak (particularly obvious in Fig. 39 (a)) come from the fact that dE/dx used for the calculation of diffusion coefficient, in the case of crystalline sample, after $x \sim 0.1$ is very close to zero and so the error becomes very big. However, this part of data is not relevant here.

Electrodes with PVDF show lower Li^+ -conductivities (Fig. 39 (a) and (b)). The deviation in the case of 60 nm sample is less than a half of order of magnitude, but 1.5 orders of magnitude in the case of 30 nm sample, while it is also true for the diffusion coefficients (Fig. 39 (d)). Apart from this, the Li solubility limit in 30 nm sized powder seems to be shifted towards a value close to zero. This effect, together with the increased OCV, will be discussed in detail in the chapter 4.1.5. The reason for decreased conductivity and diffusion coefficient by addition of PVDF is probably due to the slower diffusion of Li^+ in PVDF which has to be overcome first to reach the RuO_2 particle. With smaller particle size and hence bigger surface area the coating of the particles becomes more important. Accordingly, the effect is more pronounced in the case of crystalline powder with smaller particle size and is not observed in the case of amorphous powders due to the volume expansion caused by amorphisation.

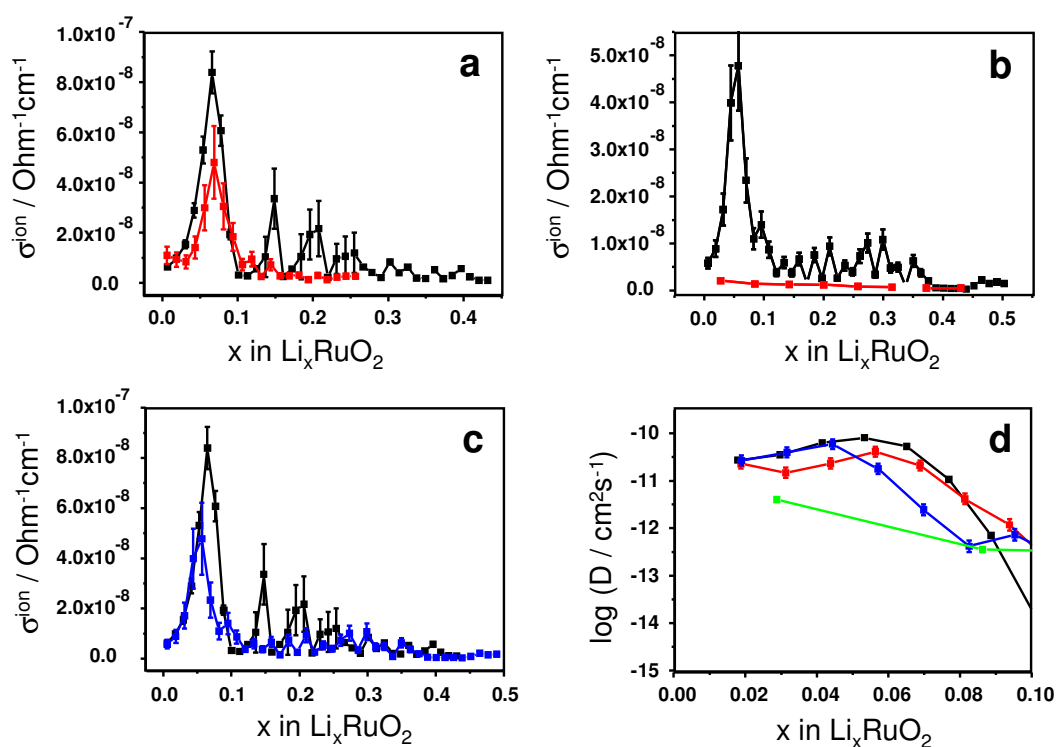


Figure 39: Li^+ -conductivities of the 60 nm (a) and 30 nm (b) sized crystalline powders with (red) and without (black) PVDF; (c) is the comparison of Li^+ -conductivities of the pure powders: black curve is 60 nm sample and blue 30 nm; (d) presents the Li-diffusion coefficients of all the four samples under consideration: 60 nm without (black) and with (red) PVDF and 30 nm sample without (blue) and with (green) PVDF.

Comparison of the Ionic Conductivities

Comparing the ionic conductivities of the pure powders in Fig. 39 (c), we can see an obvious shift of solubility limit of 30 nm sample to smaller x -values and slightly smaller ionic conductivity. Further comparison of the solubility limits of Li in RuO_2 is presented in Fig. 40 showing a clear trend, where the solubility limits are shifted to lower x -values with decreasing particle sizes, with the amorphous sample exhibiting the smallest value. The solubility limits and OCV values are dependent on each other, as already discussed in the previous chapter, so additional discussions about the samples (b) and (c) and the corresponding OCV values will be carried out in the chapters below. The maximum of the Li^+ -conductivity in the “3 nm” sample is seen, but it is rather smeared out which is quite expected for tiny sizes⁴⁴.

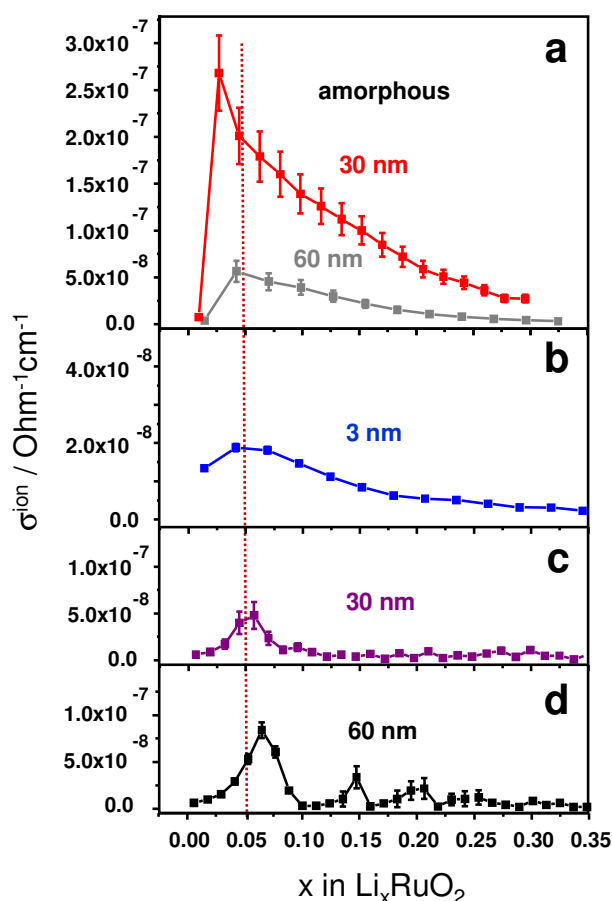


Figure 40: Li^+ -conductivities indicating the dependence of the solubility limit of Li in RuO_2 on the modification/particle size; (b), (c) and (d) represent data of pure powders.

Comparison of Diffusion Coefficients

In general, the measured diffusion coefficients of Li in RuO₂ (see Fig. 41) exhibit a common starting value at about $4 \times 10^{-11} \text{ cm}^2\text{s}^{-1}$ which is in a good agreement with the value of $2 \times 10^{-11} \text{ cm}^2\text{s}^{-1}$ given in the literature^{66,102}. With increasing Li content in the single phase regime, the values increase up to around $9 \times 10^{-11} \text{ cm}^2\text{s}^{-1}$ and begin to decrease close to the two phase regime. Exceptions are observed for the amorphous powder with the average particle size of about 30 nm exhibiting higher values and the nano-crystalline sample with the average particle size of 3 nm with lower values. As already discussed in the case of amorphous powders before, the reason might be the evaluation of the diffusion coefficient which includes the positive or negative influence of grain boundaries in the agglomerates (“pseudo-particles”). In the case of the 3 nm sample there are terminating OH-groups and traces of water (see chapter 3.3) in the grain boundaries which could decrease the Li-diffusion.

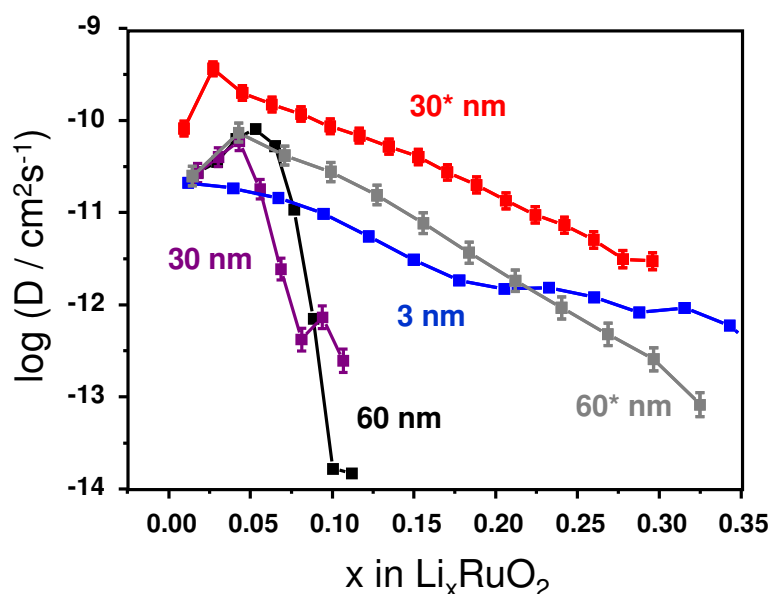


Figure 41: An overview over the diffusion coefficients of the considered RuO₂ samples; (*) indicates amorphous powders. PVDF influence is not considered, hence data of the nano-crystalline powders correspond to the experiments on pure powders.

4.1.4 Hydrous Nano-Crystalline RuO₂

Electrochemical Measurements

In an additional separate study, “hydrous” RuO₂ nano-powders, “2 h”, “20 h” and “70 h”, were investigated by performing the same electrochemical measurements which were already described in the previous chapters.

Discharge and Charge

Fig. 42 presents discharge and charge behavior of the electrodes composed of hydrothermally prepared powders and the “anhydrous” reference nano-powder with PVDF used as binder. As already discussed in the chapter 4.1.1, the influence of PVDF on the extra capacity is strongly dependent on the surface area of the powder. So it is not surprising, that commercial “anhydrous” powder with a surface area of only 85 m²g⁻¹ (strongly agglomerated) exhibits lower extra storage capacity. The capacity at the end of the second plateau (interfacial storage is not considered) is about 4.8Li per Ru and is in a good agreement with the excess value of 0.8Li per Ru composed of the typical 0.5Li which was observed on the other powders in presence of PVDF (see Fig. 25) and additional 0.3Li due to the water content. Furthermore, 4.5Li could be removed reversibly by discharge and only about 0.3Li that probably reacted with water could not be recovered. Very similar effects could be observed in the case of the “2 h” powder showing an excess capacity of *ca.* 1.7Li, where 1.13Li are due to the reaction with water. The surface area of this sample could not be measured due to the small amount of the powder, but it is assumed to be much smaller than of the powders “20 h” and “70 h” owing to the agglomeration and amorphous grain boundaries between the particles (see Fig. 14). About 0.4Li of the extra storage could be recovered, which means that the probable storage in the electrode-PVDF interface seems to be quite reversible. According to the discharge curves, electrodes “20 h” and “70 h” are supposed to store more than 1.1Li per Ru only in the electrode - PVDF interface, but unfortunately it is hard to estimate from the charge curves the real amount of recovered Li. The extended plateau at 3.75 V could be caused by side reactions with the electrolyte due to the high surface area of 360 m²g⁻¹ and hence high reactivity of the powder.

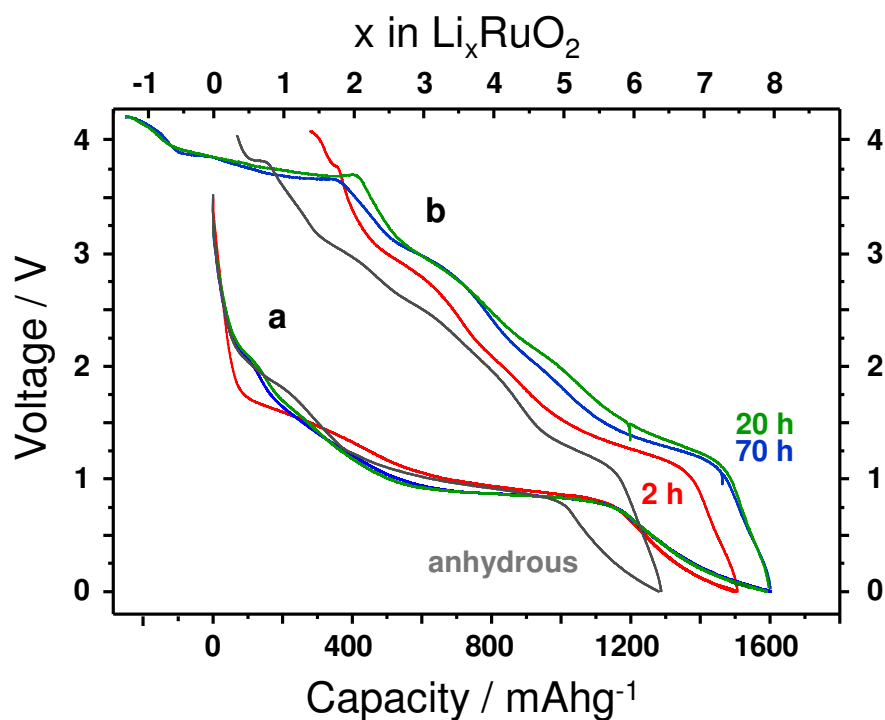


Figure 42: Discharge and charge behavior of the electrodes composed of nano-powders and PVDF.

GITT, OCV and Li-Diffusion

OCVs of the pure nano-powders at the composition Li_{0.5}RuO₂ are presented in Fig. 43. The number of the GITT steps is not the same for all the samples, since it was adapted to the weight.

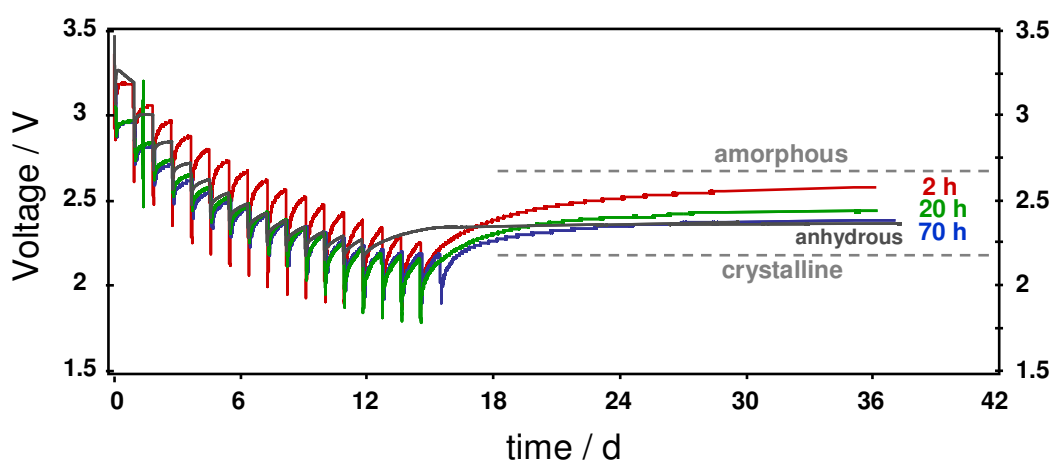


Figure 43: GITT followed by OCV measurements performed using the pure nano-powders as positive electrodes.

According to Fig. 43, it seems that with growing crystallite size and decreasing ratio of amorphous hydrous grain boundaries the OCV values decrease too. Values of the powders “70 h” and “anhydrous” are very similar, since they exhibit similar compositions and, however, a slight difference in the crystallite size distribution. Probably, the major amount of the powder “anhydrous” consists of particles with sizes of around 2-3 nm and not 10-15 nm, so that the corresponding OCV value is very close to the powder “70 h” with very narrow particle size distribution in the range of 2-3 nm. Nevertheless, if we would use $\bar{\gamma} \approx 0.1 \text{ Jm}^{-2}$ and $V_m(\text{RuO}_2) = 19.09 \text{ cm}^3 \text{ mol}^{-1}$, according to ref. [44], the excess in voltage due to the surface contribution $2V_m \bar{\gamma} / \bar{r}$ for 1 nm sized particles is expected to yield $\sim 78.8 \text{ mV}$. Here we obtain an excess of about 260 mV for the 2-3 nm (2.8 nm according to XRD) sized particles (“70 h”). The deviation could be caused by the underestimation of $\bar{\gamma}$ in addition to the neglected surface stress f which is given in the eqn (2) and includes the dependence of surface tension with strain. Taking $\bar{\alpha}$ as the average capillary parameter including $\bar{\gamma}$ and f , applying the average particle size and using the surface contribution term $2V \bar{\alpha} / \bar{r}$ and $\Delta_r G = -zF(\text{OCV})$, following values from the measured OCVs can be calculated:

Sample	Size / nm	$\delta\text{OCV} / \text{mV}$	$\delta\Delta_r G / \text{kJmol}^{-1}$	$2\bar{\alpha} / \text{Jm}^{-2}$
2 h	1.5	440	-42.45	1.67
20 h	2.5	297	-28.66	1.88
70 h	2.8	259	-24.99	1.83

Table 3: Measured excess OCV with respect to the crystalline reference value, corresponding excess Gibbs energy for the Li incorporation reaction $\delta\Delta_r G$ and the capillary parameter $\bar{\alpha}$, calculated from $\delta\Delta_r G$ in the case of “2 h”, “20 h” and “70 h” samples.

The estimated capillary parameters are close and are on average *ca.* 1 Jm^{-2} . This value is quite high, but it might be explained by the formation of the nanoparticles under non-equilibrium conditions, *e.g.* caused by the high experimental pressure of above 10 bar^{103} .

Influence of physisorbed water on the OCV values can be neglected, since, before starting the experiments, water at the SEI is immediately consumed by the electrolyte *via* substitution reactions (decomposition of $\text{Li}^{(+)}\text{PF}_6^{(-)}$) forming $\text{Li}(\text{OH})$ and HF dissolved in the electrolyte solution. Terminating OH-groups would be analogously transformed into OLi-groups under HF formation. So, with decreasing crystallite size and increasing disorder due to the increasing number of the terminating OH-groups the excess voltage could be increased up to 440 mV.

Corresponding to the increased OCVs, as predicted in the chapter 4.1.2.1.2, the solubility limits are displaced to smaller x -values. The maximum values of the samples “20 h” and “70 h” are between the values of the crystalline and amorphous samples (see Fig. 17) and the maximum of “2 h” is very close to zero (note, the solubility limit is even smaller than in the case of amorphous powders).

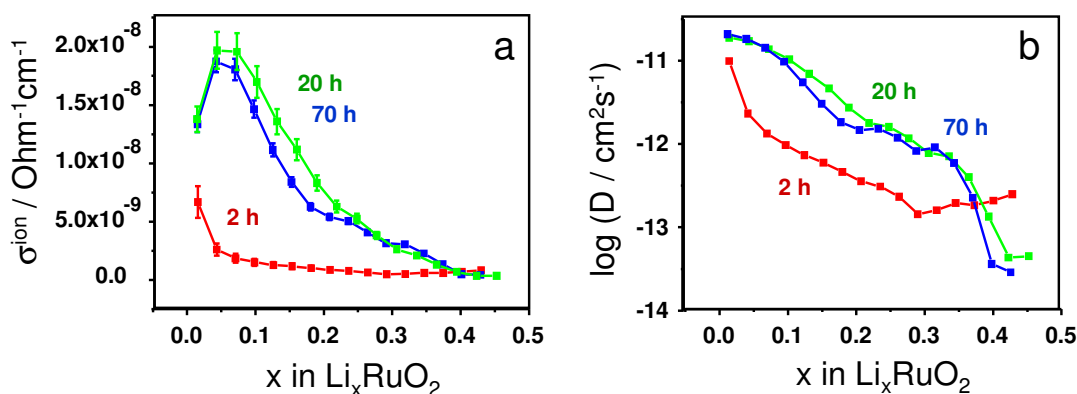


Figure 44: Li^+ -conductivity (a) and diffusion coefficient (b) of the hydrothermally prepared powders. Note that these quantities are only meaningful values in the single phase regime.

The situation here is slightly different compared to the discussion in chapter 4.1.2.1.2. The phase α' has a higher Gibbs energy due to amorphisation and not due to downsizing of the particles, so the capillary effects do not play a major role⁵⁴. Furthermore, the crystalline phase β which is formed by reaction of the amorphous phase α' with Li is identical with the phase formed by reaction of Li with the crystalline powder α . However, adopting this simplified model, assuming again shape invariance of the $G(x)$ -curves and relying on the validity

of eqn (34), following additional conjectures should be made: (a) the higher Gibbs energy of the phase α' (nano-crystalline phase) compared to α is due to the increase of the surface free energy which includes contributions from surface stress and tension; (b) the nano-crystalline phase β' has only a slightly higher Gibbs energy compared to the crystalline phase β . Due to the strong volume expansion of the particles upon lithiation the effect of the capillary terms on LiRuO_2 , formed from the nano-crystalline phase α' , is relatively low. Based on these assumptions and the experimentally obtained information about the solubility limits (a , a' , a'') and the OCVs which are correlated with the chemical potentials in the two phase regime $\mu_{\text{Li}}(a)$, $\mu_{\text{Li}}(a')$ and $\mu_{\text{Li}}(a'')$ via eqn (22), the graphical approximations shown in Fig. 45 can be constructed. Here again, the red double tangent denotes the two-phase regime of the amorphous RuO_2 with crystalline LiRuO_2 , the green double tangent represent the two-phase regime of the crystalline powders and the blue double tangent is the two-phase regime of the nano-crystalline powders. The construction takes also into account a possibly higher impact of capillary terms on the phase β' in case of the “2 h” sample (Fig. 45 (b)) due to the smaller particle size of LiRuO_2 formed from 1-2 nm sized RuO_2 crystallites. Interestingly, according to this construction, α' might even exhibit a higher Gibbs energy than the amorphous phase, even though the excess emf (as given by μ_{Li}) is smaller.

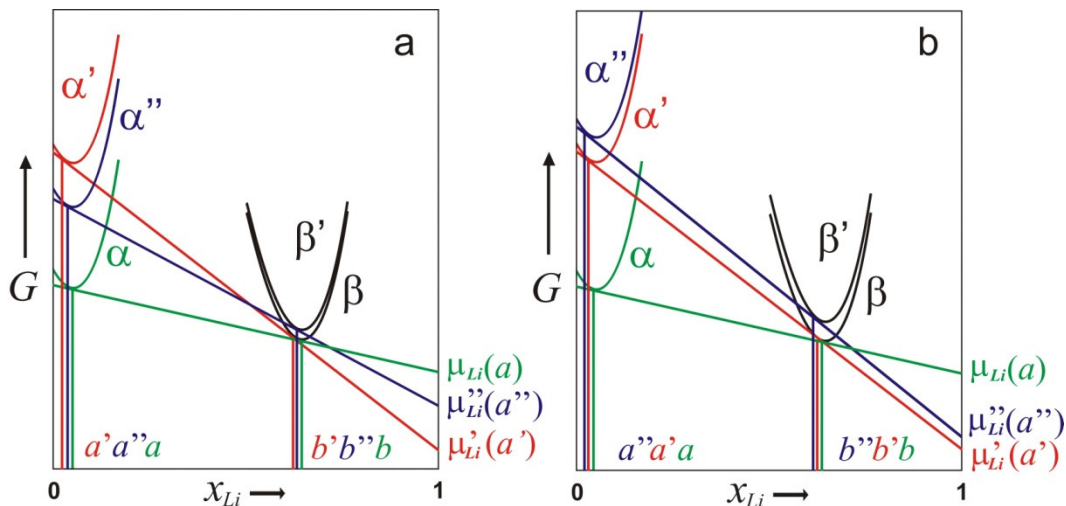


Figure 45: A construction according to the simplified model and experimental data: (a) is a possible construction for the samples “20 h”, “70 h” and “anhydrous” and (b) a construction for the sample “2 h”.

4.1.5 Influence of PVDF on OCV Values

GITT and OCV measurements on pure powders and electrodes with PVDF, used as binder, were performed and compared. The composition of the powders at the measured OCVs is again $\text{Li}_{0.5}\text{RuO}_2$. The number of the GITT steps is adjusted to the mass of the samples. Fig. 46 and 47 present the results of the pure and with PVDF coated powders.

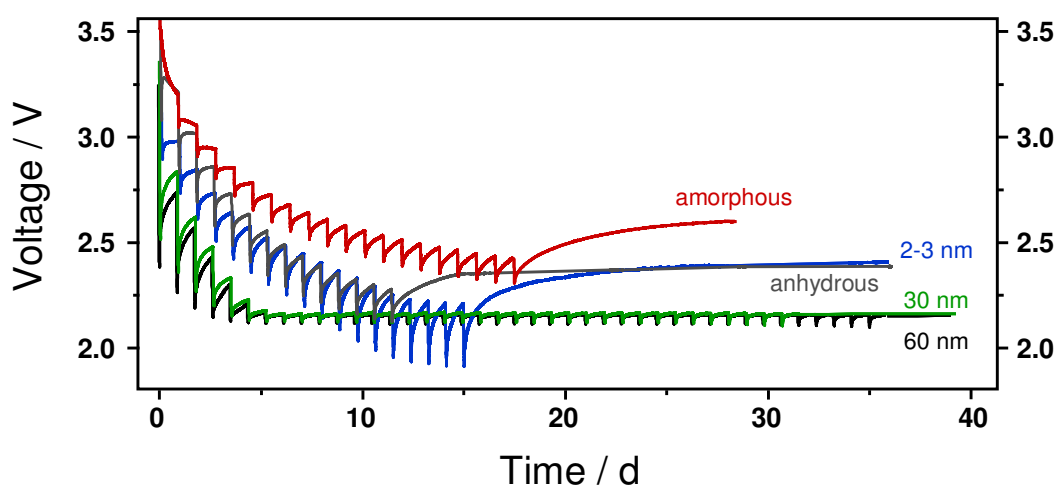


Figure 46: GITT and OCV measurements of pure powders.

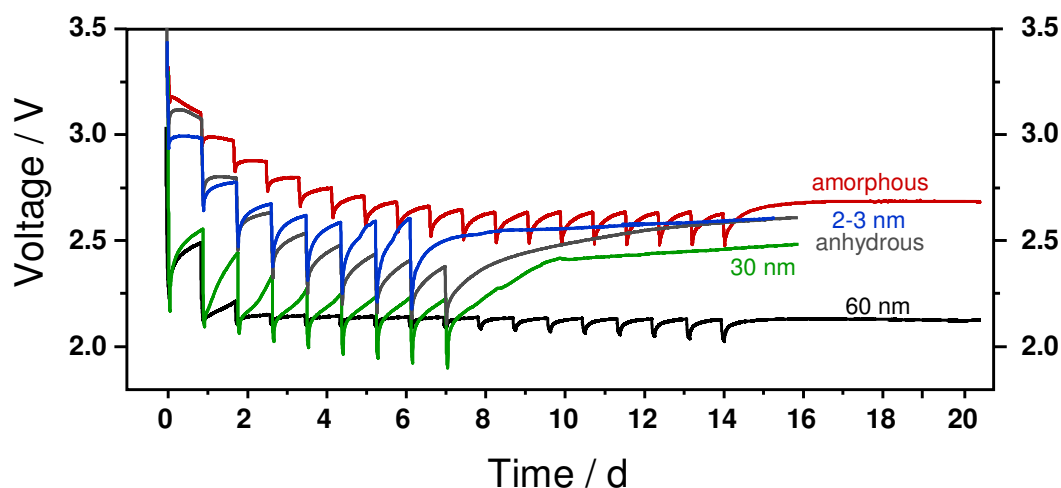


Figure 47: GITT and OCV measurements of the powders coated by PVDF.

Although the equilibration/depolarization curves of some samples, coated with PVDF, do not look homogeneously, the OCV values after a sufficient waiting time are pretty reproducible. In Fig. 48 a summary of the OCVs is provided.

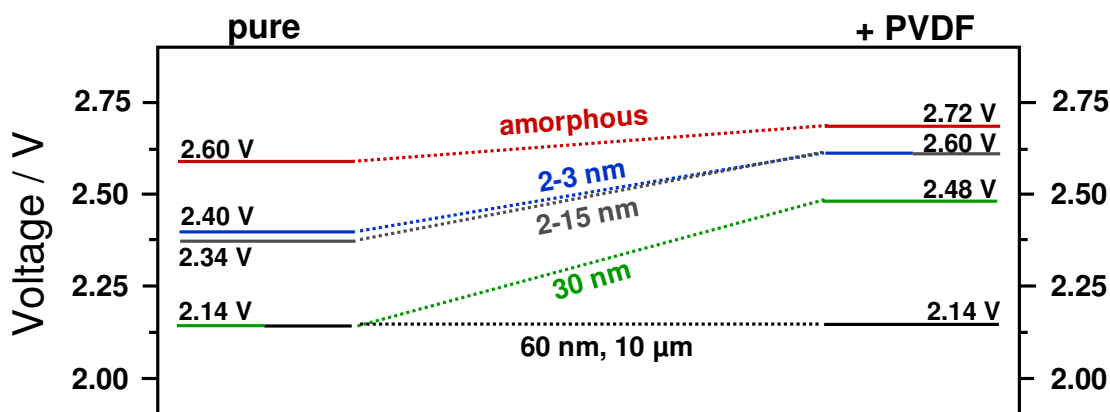


Figure 48: Comparison of the OCV values of pure particles and particles coated with PVDF.

As we can see, there is a clear trend to an increased voltage by coating of the sufficiently small particles with PVDF. Reaction of PVDF with Li in this voltage range is excluded; moreover, PVDF is a very flexible polymer which allows a tight contact to the surface of the particles. The increase of the OCV value could be attributed to the increased surface energy of the particles possibly owing to the higher strain caused by the PVDF coating. However, this quite high gain in the excess OCV value indicates bulk of the particles to be also influenced by this additional strain.

We can not observe this effect at all in the case of 60 nm and 10 μm sized particles, since the capillary terms and grain boundaries do not seem to play any significant role in this size range. The impact of the coating on amorphous powder is not large, since the particles expanded by amorphisation reducing the role of the grain boundaries. We also could not observe any remarkable shifts in the solubility limits by addition of PVDF (see Fig. 37), hence the experimental resolution of the Li-content with the according Li-conductivity values was not sufficient to notice this small difference. After all, we can distinguish two effects which were responsible for the increased OCV of the amorphous powder in comparison to the crystalline, described in the chapter 4.1.2: (a) increased Gibbs energy of the phase owing to amorphisation by 460 mV and (b) increased energy by coating with PVDF by 120 mV. Obviously, the presence of PVDF accounts for 120 mV, so that the excess value described in chapter 4.1.2 is lower by approximately 11.5 kJmol⁻¹. Nevertheless, this fact does not question the validity of the discussions in

chapter 4.1.2, since those are correct in essence and the deviation is not really big.

The coating with PVDF increases clearly the open-circuit voltages of the nanopowders (“70 h” \equiv 2-3 nm and “anhydrous” \equiv 2-15 nm), since in this particle size range every modification of the surface has a big impact on the energetics. So, the surface strain and its probable influence on the bulk of this particles additionally increases the OCV by at least 200 mV resulting in a sum an excess voltage of 460 mV in comparison to the crystalline value, taken as a reference (neglecting the influence of the coating on the bulk it would correspond to an $\bar{\alpha}$ value of 1.7 Jm^{-2}).

Particles with a size distribution around 30 nm exhibit in the pure state an OCV which is equivalent to the value of the “micro-crystalline” powder. However, according to the experiments, the particles are sufficiently small to “feel” the influence of the PVDF-coating. Here, obviously, the energy of the phase is increased only by this single effect, accordingly, rising the OCV by 340 mV (if we take it only for the surface contribution and again neglect the influence on the bulk, it would correspond to a very high $\bar{\alpha} = 12.89 \text{ Jm}^{-2}$ and an according capillary pressure of 8.6 kbar). Given the same assumptions, made in the previous chapter, and taking into account the shift in the solubility limit to the small x -values (see Fig. 49), depending on the volume expansion and the influence of PVDF on the energy of the lithiated phase (here, coated LiRuO_2), we can meet one of the cases shown in Fig. 45, denoted in blue color.

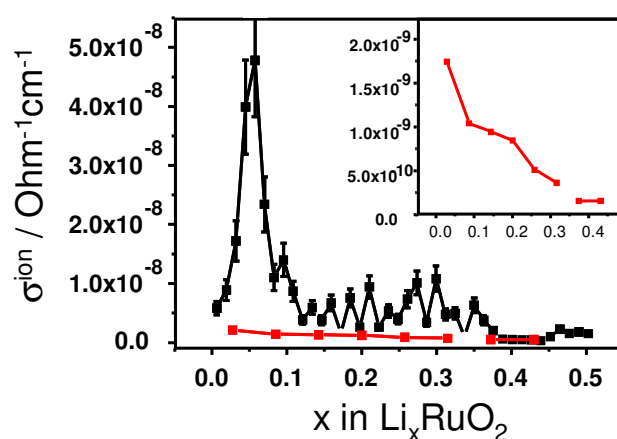


Figure 49: Li^+ -conductivity of 30 nm sized powder; pure (black) and with PVDF (red).

Of course, assuming shape invariance of the $G(x)$ -curves, *i.e.* simple parallel displacing to higher G values, is a quite an approximation, especially, when the surface stress and its influence on the bulk plays a role. Generally, in the real case, δG will vary with x , also in the amorphous state^{7,104}. Referring to a Gibbs-Kelvin type of description, shape invariance requires a constant $\bar{\gamma}$, \bar{r} and in particular a constant molar volume $V_\alpha \equiv V_{Li_\xi Y}$. (Independence of $V_{Li_\xi Y}$ from x means $V_{Li_\xi Y} = v_{Li} = v_Y$ with v_{Li} and v_Y being the partial molar volumes (appendix 2).) Moreover, for interfacial effects the validity of eqn (34) might be questioned.

4.2 Storage of Li in Metallic Ru

In this subchapter we will focus on the last part of the discharge curve – the interfacial storage⁴⁵. To prove the possibility if Li can be stored in metallic Ru or only at Li₂O/Ru interface, metallic Ru particles were used directly as the positive working electrode. Three different Ru powders with different particle sizes and surface areas were investigated as to whether there is any correlation of Li storage with the size of the surface area.

Figure 50 shows that pure metallic Ru can store Li quite reversibly. To obtain the cycling performance of the particles, the batteries with positive Ru electrodes (pure powders) were discharged and charged ten times with a current of 50 μ A ($\sim C/20$). The capacity was calculated using eqn (4) and eqn (5), where theoretical capacity was figured out considering transfer of one electron.

Fig. 50 (a) demonstrates the performance of Ru (III) with the biggest particles (200-600 nm); (b) is Ru (II), the 10 μ m sized porous particles with the crystallite size of 20 nm and (c) 10-40 nm sized particles of Ru (I). Fig. 50 (d) summarizes the strong dependence of Li storage on surface area, where an average of at least 3 different measurements of capacity in the first cycle of Ru (I-III) were taken into account.

The increased Li storage with increasing surface is caused by the larger contact area between electrolyte and electrode. In the literature there is no clear evidence for Ru to store Li in the bulk, so that the most storage might occur on the surface of Ru or in the SEI.

Powder II in the Fig. 50 (b) exhibits a long plateau at high charge voltage, which is probably due to its hierarchal porous structure that might work as a catalyst and reacts with the electrolyte.

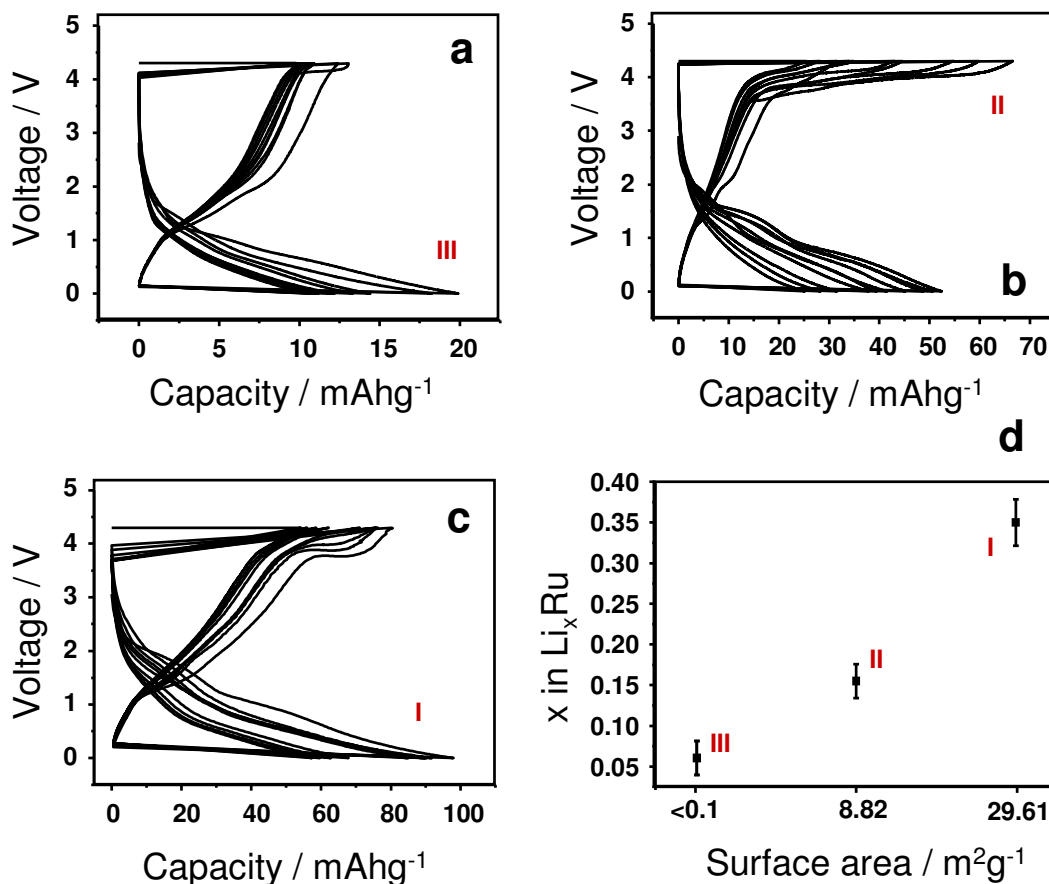


Figure 50: Cycling performance of Ru (III)(a)-(I)(c) and dependence of Li-content (first cycle) on the surface area.

More than 50% of Li is stored between 1 and 0 V, *i.e.* in the voltage window of the interfacial storage of the RuO₂/Li cell which corresponds to maximal 0.17Li per Ru. The crystallite size of Ru in a discharged RuO₂ electrode is *ca.* 1-2 nm, according to the earlier HRTEM investigations⁶⁸, and hence more than one order of magnitude lower than the average size of the here investigated powders. The typical capacity of interfacial storage in the RuO₂/Li cell is around 1.5Li which means that impressive 1.5Li per Ru are stored. Since not every Ru atom can be located on the surface, even in the case of 1 nm sized particles, there might be some additional storage mechanism. Due to the high Li⁺-conductivity of Li₂O and a perfect Li₂O-Ru contact in the Ru/Li₂O nano-

composite, the storage of Li in nano-Ru, at least in the first few atom layers, is worth being considered.

There is no Li-Ru alloy known yet according to the literature. There is only one report on LiRu_3 which was described to be obtained by arc melting¹⁰⁵. No characterization data are available apart from the experimentally found rough 1:3 atomic ratio. An attempt to obtain LiRu_3 by heating of Li metal and Ru powder with atomic ratio of 1:3 in Ar atmosphere at 500° C for several weeks, in order to obtain some characterization data, was made. According to the chemical analysis, the residual composition was LiRu_5 . The reason for this compositional variation lies most probably in the preparation method, as the Li/Ru mixture was heated in a graphite crucible which was not tightly sealed and so some Li could evaporate.

The LiRu_x compounds obtained electrochemically as well as by melting in a graphite crucible were analyzed *via* Raman, XPS and XRD. Raman turned out to be not a suitable technique to analyze Li-Ru-compounds, because changes of Li-signal with time could be observed¹⁰⁶, while to obtain a suitably high Ru signal one needs accumulation of a sufficiently high number of spectra. XPS Analysis showed a weak Li signal for the nominal composition LiRu_5 as well as for the electrochemically obtained LiRu_x compound, but there was no shift of the signals detected which could indicate a change in the oxidation state of Li or Ru. According to the XRD analysis, there was no evidence for Li being accommodating in the bulk, rather the lithiated Ru exhibited identical XRD reflections as pure Ru.

By means of the results here obtained, storage of Li in the bulk Ru can be excluded and Li in the LiRu_x compounds, obtained electrochemically as well as by melting in a graphite crucible, seems to be stored exclusively on the surface.

Chapter 5

Conclusions and Outlook

Amorphous, crystalline and nano-crystalline RuO₂ could be systematically investigated and compared in terms of OCV, diffusion coefficient and Li⁺-conductivity within the Li mol fraction $0 < x < 1$ and discharge behavior and capacity in the first discharge. Moreover, the role of PVDF in all investigated processes could be defined. Additionally, the influence of the particle size of metallic Ru on the Li storage capacity was probed.

GITT and OCV measurements allowed exciting insights into the kinetics and thermodynamics of the Li/RuO₂-LiRuO₂ system.

From GITT experiments Li concentration dependent Li diffusion coefficients and Li⁺-conductivities of RuO₂ with different particle sizes and modifications could be deduced. A new sensitive method, based on the evaluation of the Li⁺-conductivity, could be established for extracting the solubility limits of Li in nano-scaled and amorphous systems. This was not possible with the conventional method, *i.e.* from the analysis of the discharge curves, since nano-scaled and amorphous electrodes exhibit a sloped discharge profile, simulating increased solubility limits. It could be shown that with smaller particle size or amorphisation the solubility limits decrease. In the future this method should be tried on other nano-scaled electrode materials, since the solubility limit is important information for the electrochemical investigations. It must however

be kept in mind that the applicability of the method assumes a special microstructure.

OCV measurements yielded an excess voltage of about 0.5 V for amorphous phase in comparison to the crystalline phase, exhibiting the same crystalline lithiated product. This excess in the electrochemical potential could be semi-quantitatively understood in terms of melting free energy. A detailed quantitative analysis of the chemical potentials showed a striking difference in the single- and two-phase regime. A model, based on mixture thermodynamics and the assumption of the compositional independence of the Gibbs energy, could successfully correlate the experimentally obtained Li solubility limits with the corresponding OCVs. Particularly, the model demonstrates the dependence of the chemical potential of Li in the two phase regime on the Gibbs energies of the phases. With some modifications, this model could be also transferred to the case of nano-crystalline powders.

A method to prepare RuO₂ nano-particles with homogeneous size distribution (2-3 nm) and comparably low water content could be found. The influence of the surface contribution term $2V_i \bar{\alpha}/\bar{r}$ on the chemical potential as a function of the crystallite size in the size range of *ca.* 1.5-3 nm was studied. As the result, the capillary term $\bar{\alpha}$ of the nano-particles in this size range could be estimated to 1 Jm⁻² and, accordingly, enhancement of the OCV by 440 mV could be achieved.

Moreover, it could be established that coating the particles with binder (here PVDF) can increase the energy of the nano-particles as well, raising the OCV values even up to 340 mV.

Summarizing these points, it could be shown that the enhancement of the OCV values in the two phase regime, which is beneficial for the positive electrodes, can be realized not only by introducing metastability, *i.e.* down-sizing the crystallites or amorphisation, but also by different surface coatings of the particles. A necessary requirement for both cases is that the Gibbs energies of the pure and lithiated phases are sufficiently different.

Down-sizing of the particles in order to increase the Gibbs energy of the phase has been already probed on several systems, but the enhancement of the Gibbs energy by coating of the nano-scaled electrode materials, according to the

literature, was not investigated experimentally yet. It is worth continuing the studies on the impact of the surface coatings to be able to fully exploit this effect and to learn how far it could be used for improvement of the battery technology.

Furthermore, the examinations of the discharge curves (rate: C/20) resulted in higher overall voltages for nano-scale (1.5-3 nm) and amorphous particles as compared with “micro”-crystalline powders which is consistent with the higher Gibbs energy of these phases. Another, already expected effect of the particle size on the voltage could be shown, namely sloped discharge profile in the case of nano-scale and amorphous particles which was predicted^{8,44} and already verified *e.g.* on LiFePO₄ nano-powder^{6,7}.

Due to the unique properties of RuO₂, no additives are required to exhaust the full possible capacity, so that the impact of the addition of a common binder (PVDF) could be examined for the first time. Experiments showed a surface area dependent and apparently reversible increase in capacity up to 0.5-1.5Li which suggests an additional storage in the particle-binder-interface.

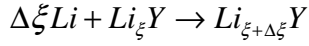
In future it would be very interesting to understand the mechanism of this extra storage, to establish if this effect can be transferred to other positive electrode materials and whether it could be utilized for improving the capacity in the Li battery system.

The Li storage experiments on Ru with different particle sizes showed a clear correlation between the surface area and the amount of the stored Li in Ru. Storage occurs obviously on the surface and in the case of electrochemical experiments also in the SEI. No evidence for the Li storage in the bulk could be found.

Appendixes

Appendix 1

Writing the cell reaction in the single phase case as



and applying the equilibrium condition yields in the limit $\Delta\xi \rightarrow 0$

$$\begin{aligned} \Delta\xi E(\xi) &\propto \mu(Li_{\xi+\Delta\xi}Y) - \mu(Li_{\xi}Y) - \mu_{Li}^0 = \\ &= (\xi + \Delta\xi)\mu_{Li}(Li_{\xi+\Delta\xi}Y) + \mu_Y(Li_{\xi+\Delta\xi}Y) - \xi\mu_{Li}(Li_{\xi}Y) - \mu_Y(Li_{\xi}Y) - \mu_{Li}^0 \\ &\approx \Delta\xi\mu_{Li}(Li_{\xi}Y) - \Delta\xi\mu_{Li}^0, \end{aligned}$$

which is simply identical to eqn (16) showing that the cell reaction formalism does not provide any further insight.

Appendix 2

For ν_{Li} or ν_Y and $V_{Li_{\xi}Y}$ a relation analogous to eqn (34) is valid. A zero variation of $V_{Li_{\xi}Y}$ with x hence requires $V_{Li_{\xi}Y}$ to be equal to ν_{Li} and hence to ν_Y . The latter is clear through symmetry or because the molar volume is the weighted sum of ν_{Li} and ν_Y . (cf. Gibbs-Duhem equation)

List of Figures

Figure 1: Comparison of gravimetric and volumetric energy densities of different battery technologies. Pb-acid batteries are mainly used in SLI (starting lighting ignition) in automobiles or standby applications ⁴	16
Figure 2: Rechargeable Li-ion battery ⁴ (“rocking-chair” - principle).....	19
Figure 3: Phenomenological model for the explanation of extra mass storage <i>via</i> the interfacial “job-sharing” storage mechanism ⁴⁵	21
Figure 4: Discharge and charge behavior of RuO ₂ electrode against Li at the rate of C/20 (1C denotes a rate at which 4Li per Ru are accommodated in 1 h.); (a)-(e) indicate the different Li storage mechanisms, with the corresponding phases represented near by.....	24
Figure 5: (a) HRTEM observations showing the coexistence of crystalline Li _{0.86} RuO ₂ and amorphous RuO ₂ ; (b) HRTEM micrograph and SAED pattern of the crystalline compound Li _{0.86} RuO ₂ formed by Li insertion into amorphous RuO ₂	26
Figure 6: X-ray diffraction patterns of RuO ₂ -samples (I)-(V).....	30
Figure 7: HRTEM/SEM micrographs of RuO ₂ samples (I)-(V): (a)-(IV), amorphous; (b)-(V), 3 nm; (c, d)-(II), 30 nm; (e)-(I), 60 nm; (f)-(III), 10 μm.	31
Figure 8: Influence of the electron irradiation on the amorphous sample during a TEM analysis.	32
Figure 9: Laser Raman spectra acquired from different RuO ₂ -samples (I)-(V) using a 632.817 nm He/Ne laser.....	33
Figure 10: XRD patterns of metallic Ru (I)–(III).	35
Figure 11: HRTEM/SEM micrographs of Ru samples (I)-(III): (a)-(I), (b)-(II) and (c)-(III).	37
Figure 12: HRTEM micrograph and SAED pattern of RuO ₂ prepared by autoclaving of the RuCl ₃ solution at 180 °C for 2 h.	38
Figure 13: Response of the particle growing to a 2 h heat treatment at every 50 °C step.	39
Figure 14: Comparison of the HRTEM micrographs and SAED patterns of powders obtained after autoclaving of RuCl ₃ solution at 180 °C for 2 h (a) and 70 h (b).	40

- Figure 15:** XRD patterns of (a) amorphous, (2 h, 20 h and 70 h) hydrothermally prepared, anhydrous (Alfa Aesar) and (c) crystalline (30 nm) reference RuO₂ powders. 41
- Figure 16:** Raman spectra of the hydrothermally prepared RuO₂ powders. 42
- Figure 17:** TG (a) and MS (b, c) data of the hydrothermally prepared samples and the anhydrous reference sample. In (b) and (c) the relative signal intensity of the mass 18 and 44 against the temperature is represented. 43
- Figure 18:** Electrochemical cell..... 44
- Figure 19:** First discharge (a) and charge (b) of crystalline RuO₂ sample at a rate of C/20..... 46
- Figure 20:** An example of GITT experiment on crystalline RuO₂; curve (a) denotes the GITT experiment and curve (b) is a discharge at a rate of C/20..... 47
- Figure 21:** GITT raw data for calculation of chemical diffusion coefficient and conductivity of Li⁺..... 48
- Figure 22:** Examples for determination of $dE/d\sqrt{t}$ and dE/dx 49
- Figure 23:** Typical plots of chemical diffusion coefficient of Li (a) and Li⁺ conductivity (b), calculated from \tilde{D} , against Li ratio in RuO₂..... 50
- Figure 24:** Cycling performance of pure crystalline RuO₂ at a rate of C/20..... 53
- Figure 25:** First discharge of RuO₂ in dependence of particle size/morphology at a rate of C/20: (a) sample (III), 10 μm; (b) - (I), 60 nm; (c) - (II), 30 nm; (d) - (IV), amorphous; (e) - (V), 3 nm; (f) overview of capacity against the particle size. Black curves present the data of pure powders and red curves denote the data of powders with additives (C, PVDF). 54
- Figure 26:** Comparison of the voltage profiles of the micro-crystalline (10 μm, red) and nano-crystalline sample (30 nm or 60 nm, black) at a rate of C/20; (a) and (b) denote the Li storage stages of the 10 μm sample with the corresponding schematic composition of the particles..... 55
- Figure 27:** SEM photographs of micro sized RuO₂ particles before (a) and after reaction with 0.8Li per mol RuO₂ (b). 56
- Figure 28:** HRTEM micrographs of RuO₂ powders: (a) - (II), 30 nm; (b) - (IV), amorphous, which was obtained after the first cycle of 30 nm powder, and (c) - (V), 3 nm..... 58
- Figure 29:** GITT and OCV measurements on RuO₂/Li cells with different particle sizes. 59

- Figure 30:** Thought experiment that connects the limit of a nano-crystalline material (with size approaching zero) to the amorphous state. The latter is characterized by a total loss of orientation (white and grey squares denote the differently orientated grains). 61
- Figure 31:** Molar Gibbs energy in the system Li-Y as a function of Li content. Coexistence of the stable phase α with the stable phase β compared with the coexistence of the metastable phase α' with the stable phase β . The respective double tangent construction yields the coexistence compositions (ε , η) as well as the corresponding chemical potentials..... 68
- Figure 32:** If the $G(x)$ curve is shifted toward higher values in the case of the metastable compound and the chemical potential of Li is increased by the same difference Δ 69
- Figure 33:** Variation of the excess chemical potential of Li from the region where we meet single phase behavior for both α and α' ($x < a'$) through a regime where we have two phase behavior for α' but not for α ($a' < x < a$) to a fully two phase situation. If the Li-rich phase would be the metastable one, would increase from Δ to $\Delta + |\Theta|$. (Note the non-differentiability at a' and a ; the form of the curve was calculated using parabolic $G(x)$ functions). 70
- Figure 34:** Determination of the cross-over composition a^* . At $a^* \mu'_{Li} = 0$ 71
- Figure 35:** Apparent ionic conductivity deduced from the Li-diffusion coefficient, which is obtained from the galvanostatic titration of RuO_2 with Li. As the Li^+ conductivity is supposed to increase with x in the x -range considered, the decreasing values are attributed to apparent effective values in the two-phase regime. 72
- Figure 36:** Galvanostatic titration curves in the system $\text{RuO}_2 - \text{LiRuO}_2$ for amorphous and (almost) macroscopically crystalline RuO_2 . The voltage refers to the potential vs. Li-electrode. As capillary effects at 60 nm are negligible, the black curve corresponds to the thermodynamically stable situation. 73
- Figure 37:** Li^+ -conductivity and Li-diffusion coefficient of amorphous RuO_2 electrodes: (a, b) obtained from 60 nm and (c, d) from 30 nm crystalline powders. Data denoted in black are results of the pure powders and in red results of electrodes containing PVDF..... 75
- Figure 38:** Comparison of amorphous samples obtained from 30 nm (blue) and 60 nm (black) sized crystalline powders. 76
- Figure 39:** Li^+ -conductivities of the 60 nm (a) and 30 nm (b) sized crystalline powders with (red) and without (black) PVDF; (c) is the comparison of Li^+ -conductivities of the pure powders: black curve is 60 nm sample and blue 30 nm; (d) presents the Li-diffusion coefficients of all the

four samples under consideration: 60 nm without (black) and with (red) PVDF and 30 nm sample without (blue) and with (green) PVDF.	77
Figure 40: Li ⁺ -conductivities indicating the dependence of the solubility limit of Li in RuO ₂ on the modification/particle size; (b), (c) and (d) represent data of pure powders.	78
Figure 41: An overview over the diffusion coefficients of the considered RuO ₂ samples; (*) indicates amorphous powders. PVDF influence is not considered.	79
Figure 42: Discharge and charge behavior of the electrodes composed of nano-powders and PVDF.	81
Figure 43: GITT followed by OCV measurements performed using the pure nano-powders as positive electrodes.	81
Figure 44: Li ⁺ -conductivity (a) and diffusion coefficient (b) of the hydrothermally prepared powders. Note that these quantities are only meaningful values in the single phase regime.	83
Figure 45: A construction according to the simplified model and experimental data: (a) is a possible construction for the samples “20 h”, “70 h” and “anhydrous” and (b) a construction for the sample “2 h”.	84
Figure 46: GITT and OCV measurements of pure powders.	85
Figure 47: GITT and OCV measurements of the powders coated by PVDF.	85
Figure 48: Comparison of the OCV values of pure particles and particles coated with PVDF.	86
Figure 49: Li ⁺ -conductivity of 30 nm sized powder; pure (black) and with PVDF (red).	87
Figure 50: Cycling performance of Ru (III)(a)-(I)(c) and dependence of Li-content (first cycle) on the surface area.	89

References

- (1) *Wochenschau Elektrochemie*; GDCh: Frankfurt am Mein, 2007.
- (2) US-Department of energy; www.eia.doe.gov/oif/ieo/index.html
- (3) Armand, M.; Tarascon, J. M. *Nature* **2008**, *451*, 652-657.
- (4) J.-M. Tarascon, M. A. *Nature* **2001**, *414*, 359-367.
- (5) Ravet, N.; at; al. In *Electrochemical Society Meeting Hawaii*, 1999.
- (6) Meethong, N.; Huang, H.-Y. S.; Carter, W. C.; Chiang, Y. M. *Electrochem. Solid State Lett.* **2007**, *10*, A134-A138.
- (7) Gibot, P.; Casas-Cabanas, M.; Laffont, L.; Levasseur, S.; Carlach, P.; Hamelet, S.; Tarascon, J. M.; Masquelier, C. *Nat. Mater.* **2008**, *7*, 741-747.
- (8) Van der Ven, A.; Wagemaker, M. *Electrochem. Commun.* **2009**, *11*, 881-884.
- (9) Ikeda, H.; Saito, T.; Tamura, H. *Proc. Manganese Dioxide Symposium* **1975**, *1*.
- (10) Wittingham, M. S. US patent 4009052.
- (11) Wittingham, M. S. *Science* **1976**, *192*, 1226.
- (12) Carides, J. N.; Murphy, D. W. *J. Electrochem. Soc.* **1977**, *124*, 1309.
- (13) Abraham, K. M.; Pasquariello, D. M.; Martin, F. J. *J. Electrochem. Soc.* **1986**, *133*, 661.
- (14) Auburn, J. J.; Barberio, Y. L.; Hanson, K. J.; Schleich, D. M.; Martin, M. J. *J. Electrochem. Soc.* **1987**, *134*, 580.
- (15) Murphy, D. W.; DiSalvo, F. J.; Carides, J. N.; Waszczak, J. V. *Mater. Res. Bull.* **1978**, *13*, 1395-1402.
- (16) Lazzari, M.; Scrosati, B. *J. Electrochem. Soc.* **1980**, *127*, 773.
- (17) DiPietro, B.; Patriarca, M.; Scrosati, B. *J. Power Sources* **1982**, *8*, 298.
- (18) Mohri, M. *J. Power Sources* **1989**, *26*, 545-551.

- (19) Tarascon, J. M.; Gozdz, A. S.; Schmutz, C.; Shokoohi, F.; Warren, P. C. *Solid State Ion.* **1996**, *86-88*, 49-54.
- (20) Arico, A. S.; Bruce, P.; Scrosati, B.; Tarascon, J. M.; Van Schalkwijk, W. *Nat. Mater.* **2005**, *4*, 366-377.
- (21) Schoonman, J. *Solid State Ion.* **2000**, *135*, 5-19.
- (22) Maier, J. *Nat. Mater.* **2005**, *4*, 805-815.
- (23) Bisquert, J. *Phys. Chem. Chem. Phys.* **2008**, *10*, 49-72.
- (24) Maier, J. *J. Power Sources* **2007**, *174*, 569-574.
- (25) Balaya, P.; Bhattacharyya, A. J.; Jamnik, J.; Zhukovskii, Y. F.; Kotomin, E. A.; Maier, J. *J. Power Sources* **2006**, *159*, 171-178.
- (26) Balaya, P. *Energy Environ. Sci.* **2008**, *1*, 645-654.
- (27) Suzdalev, I. P. *Russ. Chem. Rev.* **2009**, *78*, 249-282.
- (28) Tuller, H. L. *Solid State Ion.* **2000**, *131*, 143-157.
- (29) Maier, J. *Solid State Ion.* **2003**, *157*, 327-334.
- (30) Maier, J. *Solid State Ion.* **2002**, *154-155*, 291-301.
- (31) Maier, J. *Solid State Ion.* **2004**, *175*, 7-12.
- (32) Maier, J. *Solid State Ion.* **2002**, *148*, 367-374.
- (33) Maier, J. 9th Europhysical Conference on Defects in Insulating Materials, Wroclaw, Poland, 2002; p 1-10.
- (34) Maier, J. *Journal of the European Ceramic Society* **2004**, *24*, 1251-1257.
- (35) Maier, J. *Phys. Chem. Chem. Phys.* **2009**, *11*, 3011-3022.
- (36) Armin, R.; Balaya, P.; Maier, J. *Electrochem. Solid State Lett.* **2007**, *10*, A13.
- (37) Delacourt, C.; Laffont, L.; Bouchet, R.; Wurm, C.; Leriche, J.-B.; Morcrette, M.; Tarascon, J. M.; Masquelier, C. *J. Electrochem. Soc.* **2005**, *152*, A913.
- (38) Ojczyk, W.; Marzec, J.; Swierczek, K.; Zajac, W.; Molenda, M.; Dziembaj, R.; Molenda, J. *J. Power Sources* **2007**, *173*, 700.

- (39) Morgan, D.; Van der Ven, A.; Ceder, G. *Electrochem. Solid State Lett.* **2004**, *7*, A30.
- (40) Manthiram, A.; Choi, J.; Choi, W. *Solid State Ion.* **2006**, *177*, 2629.
- (41) Saravanan, K.; Reddy, M. V.; Balaya, P.; Gong, H.; Chowdari, B. V. R.; Vittal, J. J. *J. Mater. Chem.* **2009**, *19*, 605-610.
- (42) Guo, Y. G.; Hu, Y. S.; Sigle, W.; Maier, J. *Adv. Mater.* **2007**, *19*, 2087-+.
- (43) Poizot, P.; Laruelle, S.; Grugeon, S.; Dupont, L.; Tarascon, J. M. *Nature* **2000**, *407*, 496-499.
- (44) Jamnik, J.; Maier, J. *Phys. Chem. Chem. Phys.* **2003**, *5*, 5215-5220.
- (45) Zhukovskii, Y. F.; Balaya, P.; Kotomin, E. A.; Maier, J. *Phys. Rev. Lett.* **2006**, *96*, 4.
- (46) Maier, J. Meeting on Atomic Transport and Defect Phenomena in Solids, Guildford, ENGLAND, 2006; p 51-66.
- (47) Bekaert, E.; Balaya, P.; Murugavel, S.; Maier, J.; Menetrier, M. *Chem. Mat.* **2009**, *21*, 856-861.
- (48) Laruelle, S.; Grugeon, S.; Poizot, P.; Dolle, M.; Dupont, L.; Tarascon, J. M. *J. Electrochem. Soc.* **2002**, *149*, A627.
- (49) Liao, P.; MacDonald, B. L.; Dunlap, R. A.; Dahn, J. R. *Chem. Mat.* **2008**, *20*, 454.
- (50) Buffat, P.; Borel, J. P. *Phys. Rev. A* **1976**, *13*, 2287-2298.
- (51) Shuttleworth, R. *Proc. Phys. Soc. A* **1950**, *63*, 444.
- (52) Kramer, D.; Weissmuller, J. *Surf. Sci.* **2007**, *601*, 3042-3051.
- (53) McHale, J. M.; Auroux, A.; Perrotta, A. J.; Navrotsky, A. *Science* **1997**, *277*, 788-791.
- (54) Pitcher, M. W.; Ushakov, S. V.; Navrotsky, A.; Woodfield, B. F.; Li, G. S.; Boerio-Goates, J.; Tissue, B. M. *J. Am. Ceram. Soc.* **2005**, *88*, 160-167.
- (55) Ranade, M. R.; Navrotsky, A.; Zhang, H. Z.; Banfield, J. F.; Elder, S. H.; Zaban, A.; Borse, P. H.; Kulkarni, S. K.; Doran, G. S.; Whitfield, H. J. *Proc. Natl. Acad. Sci. U. S. A.* **2002**, *99*, 6476-6481.
- (56) Gräf, C. P.; Heim, U.; Schwitzgebel, G. Conference on Interfacially Controlled Functional Materials: Electrical and Chemical Properties, Schloß Ringberg, Germany, 1998; p 165-174.

- (57) Knauth, P.; Schwitzgebel, G.; Tschöpe, A.; Villain, S. *J. Solid State Chem.* **1998**, *140*, 295-299.
- (58) Villain, S.; Knauth, P.; Schwitzgebel, G. *J. Phys. Chem. B* **1997**, *101*, 7452-7454.
- (59) Jacob, K. T.; Jayadevan, K. P.; Mallya, R. M.; Waseda, Y. *Adv. Mater.* **2000**, *12*, 440-+.
- (60) Gartner, F.; Bormann, R.; Birringer, R.; Tschöpe, A. *Scr. Mater.* **1996**, *35*, 805-810.
- (61) Schroeder, A.; Fleig, J.; Drings, H.; Wuerschum, R.; Maier, J.; Sitte, W. EMRS Symposium on Solid State Ionics, Strasbourg, FRANCE, 2004; p 95-101.
- (62) Balaya, P.; Maier, J. *to be submitted to Physical Chemistry Chemical Physics*.
- (63) Delmer, O.; Balaya, P.; Kienle, L.; Maier, J. *Adv. Mater.* **2008**, *20*, 501-505.
- (64) Delmer, O.; Maier, J. *Phys. Chem. Chem. Phys.* **2009**, DOI: 10.1039/b822961a.
- (65) Meethong, N.; Huang, H. Y. S.; Carter, W. C.; Chiang, Y. M. 210th Meeting of the Electrochemical-Society, Cancun, MEXICO, 2006; p A134-A138.
- (66) Armand, M.; Dallard, F.; Deroo, D.; Mouliom, C. *Solid State Ion.* **1985**, *15*, 205-210.
- (67) Dalard, P.; Deroo, D.; Foscallo, D.; Mouliom, C. *Solid State Ion.* **1985**, *15*, 91-94.
- (68) Balaya, P.; Li, H.; Kienle, L.; Maier, J. *Adv. Funct. Mater.* **2003**, *13*, 621-625.
- (69) Jirkovsky J.; Makarova M.; Krtil, P. *J. Electrochem. Soc.* **2005**, *152*, A1613-A1619.
- (70) Lytle J. C.; Rhodes C. P.; Long, J. W.; Pettigrew, K. A.; Stroud, R. M.; Rolison, D. R. *J. Mater. Chem.* **2007**, *17*, 1292-1299.
- (71) Kuratani, K.; Kiyobayashi, T.; Kuriyama, N. *J. Power Sources* **2009**, *189*, 1284-1291.
- (72) Tsuda, N.; Nasu, K.; Fujimori, A.; Siratori, K. *Electronic conduction in oxides*; Second ed.; Springer, 2000.

- (73) Balaya, P.; Hu, Y. S.; Maier, J. World Scientific, Kandy, Sri Lanka, 2006.
- (74) Cullity, D. (*Addition-Wesley, Reading, MA*) **1967**, 261.
- (75) Huang, Y. S.; Pollak, F. H. *Solid State Communications* **1982**, *43*, 921-924.
- (76) Music, S.; Popovic, S.; Maljkovic, M.; Furic, K.; Gajovic, A. *Materials Letters* **2002**, *56*, 806-811.
- (77) Ryan, J. V.; Berry, A. D.; Anderson, M. L.; Long, J. W.; Stroud, R. M.; Cepak, V. M.; Browning, V. M.; Rolison, D. R.; Merzbacher, C. I. *Nature* **2000**, *406*, 169-172.
- (78) Bhaskar, S.; Dobal, P. S.; Majumder, S. B.; Katiyar, R. S. *Journal of Applied Physics* **2001**, *89*, 2987-2992.
- (79) Music, S.; Popovic, S.; Maljkovic, M.; Saric, A. *Materials Letters* **2004**, *58*, 1431-1436.
- (80) Weppner, W.; Huggins, R. A. *J. Electrochem. Soc.* **1977**, *124*, 1569-1578.
- (81) Besenhard, J. O.; Wachtler, M.; Winter, M.; Andreaus, R.; Rom, I.; Sitte, W., Edinburgh, Scotland, 1998; p 268-272.
- (82) Chen, C. H.; Kelder, E. M.; Jak, M. J. G.; Schoonman, J. *Solid State Ion.* **1996**, *86-88*, 1301.
- (83) Striebel, K. A.; Deng, C. Z.; Wen, S. J.; Cairns, E. J. *J. Electrochem. Soc.* **1996**, *143*, 1821.
- (84) Yan, H.; Huang, X.; Li, H.; Chen, L. *Solid State Ion.* **1998**, *113-115*, 11.
- (85) Levi, M. D.; Gamolsky, K.; Aurbach, D.; Heider, U.; Oesten, R. *J. Electroanal. Chem.* **1999**, *477*, 32.
- (86) Levi, M. D.; Levi, E.; Aurbach, D.; Schmidt, M.; Oesten, R.; Heider, U. *J. Power Sources* **2001**, *97-98*, 525.
- (87) Shembel, E.; Apostolova, R.; Nagirny, V.; Aurbach, D.; Markovsky, B. *J. Power Sources* **1999**, *81-82*, 480.
- (88) Huang, H.; Kelder, E. M.; Chen, L.; Schoonman, J. *J. Power Sources* **1999**, *81-82*, 362.
- (89) Maurin, G.; Bousquet, C.; Henn, F.; Simon, B. *Ionics* **1999**, *5*, 156.
- (90) Shembel, E.; Apostolova, R.; Nagirny, V.; Aurbach, D.; Markovsky, B. *J. Power Sources* **1999**, *80*, 90.

- (91) Levi, M. D.; Aurbach, D. *Electrochim. Acta* **1999**, *45*, 167.
- (92) Stomme Mattsson, M. *Solid State Ion.* **2000**, *131*, 261.
- (93) Molenda, J.; Wilk, P.; Marzec, J. *Solid State Ion.* **2003**, *157*, 115.
- (94) Cao, F.; Prakash, J. *Electrochimica Acta* **2002**, *47*, 1607-1613.
- (95) Deiss, E. *Electrochimica Acta* **2002**, *47*, 4027-4034.
- (96) Deiss, E. *Electrochimica Acta* **2005**, *50*, 2927-2932.
- (97) Maier, J. *Festkörper - Fehler und Funktion*; Teubner: Stuttgart - Leipzig, 2000.
- (98) Li, H.; Balaya, P.; Maier, J. *J. Electrochem. Soc.* **2004**, *151*, A1878-A1885.
- (99) Barin, I. *Thermodynamical Data of Pure Compounds*; Wiley-VCH: Weinheim, Germany, 1989.
- (100) Atkins, P. W. *Physical Chemistry*; Freeman: New York, 1998.
- (101) Swalin, R. A. *Thermodynamic of Solids*; Wiley: New York, 1972.
- (102) Dallard, F.; Deroo, D.; Mauger, R. *J. Power Sources* **1983**, *9*, 321.
- (103) "Drucktabelle," www.dampf.com, Stritzel Dampftechnik.
- (104) Meethong, N.; Huang, H. Y. S.; Speakman, S. A.; Carter, W. C.; Chiang, Y. M. *Adv. Funct. Mater.* **2007**, *17*, 1115-1123.
- (105) Loebich, O.; Raub, C. J. *Platinum Metals Rev.* **1981**, *25*, 113-120.
- (106) Naudin, C.; Bruneel, J. L.; Chami, M.; Desbat, B.; Grondin, J.; Lassegues, J. C.; Servant, L. *J. Power Sources* **2003**, *124*, 518-525.

Acknowledgements

I would like to thank to all those who were directly or indirectly involved in this work:

Prof. Joachim Maier, for his support, suggestions, fruitful discussions, theoretical analysis of the chemical potentials of lithium and especially for the prompt corrections of the thesis,

Balaya Palani, for the introduction in the Li battery topic and supervision in the first year,

Prof. Werner Sitte, for explanation of some details concerning the Li diffusion coefficient,

Dominik Samuelis, for writing a program which made the evaluation of the enormous amount of the GITT data possible,

Rotraut Merkle, for having always been ready for any scientific discussion and for performing TG and MS measurements,

several who assisted with technical support, including
Viola Duppel, for beautiful HRTEM and SEM micrographs,
Gabi Götz, for an enormous number of XRD patterns,
Anette Fuchs, for the fast SEM and BET analyses,
Armin Schultz, for many Raman spectra,
Dr. Mitsuharu Konuma, for his patience with the XPS analyses,
Udo Klock and Peter Senk, for solving technical problems,
Uve Traub, for solving all the computer related problems,

Sofia Weiglein, for her bountiful administrative support,

all my colleagues who accompanied me during my time at MPI and became very close friends, (I hope to keep in touch with you for many, many years!)

my family, for loving support as long as I can remember,

Damian Delmer, for his loving support through many years,

and Jose Luis Marrazzo, for his understanding and loving support during the last stages of this work.

Curriculum Vitae

Name:	Olga Delmer, geb. Reifschneider
Nationality:	German
Date of birth:	September 8 th , 1979
Place of birth:	Frunze (Bishkek) in Kirgizia
09/1989 – 09/1993	Secondary school in Frunze
10/1993	emigration to Germany
10/1993 – 7/1994	Secondary school in Ludwigsburg
09/1994 – 7/1997	Secondary school: Werkrealschule in Marbach am Neckar
09/1997 – 6/2000	Secondary school: Ernährungswissenschaftliches Gymnasium in Ludwigsburg
6/2000	Abitur
10/2000 – 12/2004	Chemistry studies at the University of Stuttgart
01/2005 – 07/2005	Diploma thesis at the University of Stuttgart in collaboration with Robert Bosch GmbH: <i>“Phasenanalyse gefüllter Pyrolysekeramiken im System SiOC mit Hilfe der Festkörper-NMR-Spektroskopie”</i>
07/2005	Diplom
11/2005 – 11/2009	PhD at Max Planck Institute for Solid State Research, Stuttgart: <i>“Size and Morphology Effects on the Cell Voltage of Li-Batteries: Case Study of RuO₂”</i> with Prof. Dr. Joachim Maier